AD-A007 512

INTEGRATED OPTICAL CIRCUIT DEVICES

W. E. Martin, et al

Naval Electronics Laboratory Center

Prepared for:

Defense Advanced Research Projects Agency

1 February 1975

REPORT DOCUMENTATION PAGE		READ INSTRUCTIONS BEFORE COMPLETING FORM
1. REPORT NUMBER NELC Technical Report 1942 (TR 1942)	2. GOVT ACCESSION NO.	3. RECIPIENT'S CATALOG NUMBER AD/A007 512
4. TITLE (and Subtitle) INTEGRATED OPTICAL CIRCUIT DEVICES (Presents current status of the ARPA/NELC program in integrated optical circuits and fiber optics for use in Navy and DoD communication and information processing systems)		5. TYPE OF REPORT & PERIOD COVERED R&D, 1 April to 30 September 1974
		6. PERFORMING ORG. REPORT NUMBER
7. AUTHOR(s) W. E. Martin and L. B. Stotts		8. CONTRACT OR GRANT NUMBER(s)
9. PERFORMING ORGANIZATION NAME AND ADDRESS Naval Electronics Laboratory Center San Diego, California 92152		10. PROGRAM ELEMENT, PROJECT, TASK AREA & WORK UNIT NUMBERS 60000E, P3D10, OSD (NELC F215)
11. CONTROLLING OFFICE NAME AND ADDRESS Defense Advanced Research Projects Agency 1400 Wilson Boulevard, Arlington, Virginia 22209		12. REPORT DATE 1 February 1975
		13. NUMBER OF PAGES 86 83
14. MONITORING AGENCY NAME & ADDRESS(If different from Controlling Office)		15. SECURITY CLASS. (of this report) UNCLASSIFIED
		15a. DECLASSIFICATION/DOWNGRADING SCHEDULE
16. DISTRIBUTION STATEMENT (of this Report) Approved for public release; distribution unlimited		
17. DISTRIBUTION STATEMENT (of the abstract entered in Block 20, if different from Report)		
18. SUPPLEMENTARY NOTES		

19. KEY WORDS (Continue on reverse side if necessary and identify by block number)

Optical integrated circuit
Optical materials
Waveguides--Properties
Lasers
Waveguides--Coupling

20. ABSTRACT (Continue on reverse side if necessary and identify by block number)

The objectives of the program described here are to advance the material and device physics of integrated optics for military applications; to establish, in concert with other Navy and DoD programs, a continuing assessment of system requirements and cost benefits for R&D investments in each application area; and to produce prototype optical elements and subsystems that are aimed at satisfying these requirements.

The report includes articles on Materials and Fabrication Techniques for Integrated Optical Circuitry, Waveguide Device Properties, Pattern Fabrication Techniques, Laser Development, Fabrication and Analysis of Input/Output Waveguide Coupling, and Transients in Periodic Structures: Coupled Waves Approach.

DD FORM 1473 1 JAN 73   EDITION OF 1 NOV 65 IS OBSOLETE
S/N 0102-014-6601

OBJECTIVE

Study and contribute to the advancement of integrated optical circuits (IOCs) and fiber optics and their application in information transfer and processing systems. Emphasize applications in Navy and other DoD programs in airborne, shipboard, land-based, and undersea systems.

Contribute to and evaluate the state of the art in material and device techniques for the fabrication of IOC devices such as sources, couplers, switches, and modulators. Determine the feasibility of employing fiber optics and IOC technology in military applications such as high-capacity (multi-GHz) data links, data buses, and nonradiating and radiation-resistant communication systems.

RESULTS

1. Theoretical analysis of the propagation constants in diffused optical waveguides has been performed by use of various approximating techniques.

2. Electrooptic modulation of light in a planar waveguide fabricated from a zinc-blende type crystal has been analyzed.

3. Directional coupling has been observed in ZnSe by use of conventional photolithography.

4. The generation of closely spaced lines with extremely smooth edges in SiO_2 deposited on semiconductor substrates has been demonstrated.

5. Characterization of Ge-doped double-heterojunction light-emitting diodes and cw laser diodes has been performed.

6. Threshold shifts in $Ga_{1-x}Al_x As$ double-heterojunction lasers with a corrugated interface have been investigated theoretically.

7. Input/output waveguide coupling structures have been fabricated and analyzed.

8. Coupling from planar to linear waveguides by means of horn structures has been evaluated theoretically along with transients in periodic couplers.

RECOMMENDATIONS

1. Develop optical interconnections between waveguides, fibers, and lasers using horns or other structures.

2. Develop optical integrated circuit elements such as two-port optical switches and electrooptical modulators.

3. Develop low-loss, single-mode glass fibers, 1-3 km in length.

4. Provide continued support to the development of continuous room-temperature laser diodes.

5. Develop electronic drivers for electrooptic switches, modulators, and detector amplifiers.

6. Assemble an IOC breadboard demonstration system incorporating the low-loss fibers, laser diodes, and integrated optical circuits developed in this program.

ADMINISTRATIVE INFORMATION

CONTENTS

INTRODUCTION

The fabrication of miniature solid-state optical components connected by channel waveguides is becoming feasible with the advancement of such disciplines as the materials sciences, quantum electronics, and guided-wave optics. Integrated optical components — sources, detectors, modulators, and various coupling elements — on one or more tiny substrates will comprise systems much smaller in size and weight than optical systems employing discrete components. These components will perform a number of functions in the area of optical communications. They include rapid modulation and switching by guided-wave elements using applied fields to generate small refractive index changes, coupling, filtering of signals, light detection by p-n junctions or other structures in thin films, and light generation by thin-film laser elements. The new systems will be much less susceptible to environmental hazards, such as mechanical vibrations, extremes in temperature, and electromagnetic fluctuations because of their small size and packaging density. In addition, wideband active components, such as waveguide electrooptic modulators and switches, will be able to operate at very low power levels because of the small dimensions involved.

Guided-wave optical components have found an important potential use in the area of optical communications because of recent progress in the fabrication of single-mode fiber-optic waveguides with very low losses. Fiber-optic waveguides with losses as low as 1-2 dB/km at 0.85-μm and 1.06-μm wavelengths (for GaAs and Nd-YAG lasers, respectively) and single-mode fibers having anticipated bandwidths as high as 10 GHz for a 1-km length immensely widen the horizon of optical communications. Single-mode devices must be developed to couple energy efficiently with the fibers and to process the optical information efficiently at rates approaching the bandwidth capacity of the fibers.

Fiber-optic waveguide systems offer significant advantages for military information transfer, both immediately, with discrete components and multimode fibers, and in the future, with single-mode fibers and integrated optical elements. These advantages include freedom from electromagnetic interference (EMI, EMP), elimination of grounding problems, and elimination of signal leakage, as well as the potential for large savings in size, weight, power consumption, and cost. In addition to high-capacity point-to-point communications, a major interest in integrated optics from a military standpoint is the potential for implementing a fiber optic-transmission line multiterminal (data bus) multiplexing system through low-loss coupling and modulation elements. This will provide isolated-terminal, redundant information transfer, thus facilitating the truly modular (including distributed computer) command control and communications system. Another promising area is in fast, high-capacity, high-density multiport switches for interconnecting networks.

The objectives of the program reported here are to advance the material and device physics of integrated optics for military applications, to establish in concert with other Navy and DoD programs a continuing assessment of system requirements and cost benefits for R&D investments in each application area, and to produce prototype optical elements and subsystems that are aimed at satisfying these requirements. The work on the program that was performed at Naval Electronics Laboratory Center (NELC) and under contracts administered by NELC was in the areas of integrated-optical-circuit (IOC) applications assessment, materials for IOC devices and substrates, pattern fabrication, theoretical analysis, components, and system concepts.

Experimentally, effort continued to be centered on the fabrication of IO components, such as optical switches and waveguide modulators.

This report is divided into the following six sections:

Materials and Fabrication Techniques for Integrated Optical Circuitry, Waveguide Device Properties, Pattern Fabrication Techniques, Laser Development, Fabrication and Analysis of Input/Output Waveguide Coupling Structures, and Transients in Periodic Structures: Coupled Waves Approach.

Within each section are several subsections concerning specific work by NELC or others under contracts administered by NELC. The performing organization is indicated in the introduction to each subsection.

MATERIALS AND FABRICATION TECHNIQUES FOR
INTEGRATED OPTICAL CIRCUITRY

During recent years it has become apparent that an optical material analog to the highly successful silicon substrates used in monolithic integrated circuitry is presently not to be found in the wide range of materials explored for integrated optical circuit (IOC) use. Of the materials investigated[1], the III-V compounds, most notably GaAs and GaAlAs, stand out as the best potential candidates for a totally monolithic structure; that is, source, wave-guide components, and detector on a single chip, in the medium-to-long-term development time scale (5-10 years). This technology, however, brings with it several material and fab-rication problems which must be solved before a complex IOC can be realized. Most notable of these is the relatively high loss incurred in optical waveguides at the wavelength of the most efficient source. For example, the leading contender as a source in integrated optics is the cw room-temperature injection laser which emits at $\sim0.85~\mu m$. The best GaAlAs waveguides to date have losses on the order of 10–30 dB/cm at that wavelength. Choosing a longer-wavelength source such as InGaAs ($\sim1.0~\mu m$) with GaAlAs as the guide material (losses <5dB/cm at $1.15~\mu m$) increases the complexity of fabrication and replaces the loss problem with that of lattice mismatch. This is evident by noting that the best III-V lasers and waveguides are produced by planar liquid-phase epitaxy (LPE) techniques. Selective etching and regrowth, and multisource LPE growth, however, do offer promise as a solution to the latter problem. It is apparent, in any event, that the full benefits of monolithic IOCs will only be realized by an extensive development of the III-V compounds. Thus, it is more likely that integrated optics will follow an evolution similar to that of the electronic IC semiconductor technology. That is, the trend will be towards a hybrid approach in the near term. In the hybrid approach, each component group is optimized for a given function, such as light generation, active and passive waveguide components, or detection, in terms of the material/fabrication technique best suited for the particular function. The one significant difference between electronic ICs and IOCs is the wider range of material parameters required for the latter.

Table 1 lists some of the most promising material systems and their associated fabrication methods. This is not intended to be exhaustive nor are all possible fabrication techniques for the various materials included.

For the near-term hybrid technology of IOC development, diffusion into active materials such as ZnSe and $LiNbO_3$ appears to be the best means of constructing active waveguides and interconnects. A cw GaAlAs injection laser is the leading source for this case, with either InGaAs or Si avalanche photodiodes as the detectors in the system. Optimizing each component in the IOC as to performance places the principal burden of integration on coupling the various elements together. Until efficient high-level technology coupling schemes such as periodic or distributed-gap couplers are reliably available, the most likely coupling arrangement will be butt-joined end-fire coupling. The monolithic technology in IOCs when fully developed will of course use continuous or distributed coupling between components.

To summarize, at this time there is no single material/fabrication system which is satisfactory in all respects for monolithic IOC fabrication. Considerable effort must be devoted to material and fabrication techniques for a completely monolithic technology to be developed. Hybrid systems optimize the individual components, but presently lack optical coupling schemes. For practical IOC devices a semihybrid technology may prove most efficient for ongoing system development. For the short term, a system consisting

3

TABLE 1.

Material System	Representative Types	Fabrication Techniques	Interaction	Loss	Advantages/Limitations
III-V	GaAs/GaAlAs, GaP etc.	LPE, VPE, II, D*, IM	EO, AO	~5dB/cm @1.15 μm	Best source mat'l, good detectors, large waveguide losses at emitting wavelength, difficult pattern fabrication in LPE
Liquid Crystal	MBBA, Cholesteric/ Nematic mixture	Various planar (sandwich, etc.)	EO, scattering	15-40dB/cm @.633 μm	High activity, slow operation, no source detector, multi-scheme addressable
Garnets	YIG, GGG	VPE, LPE	MO	~4dB/cm @1.06 μm	Very slow operation, difficult pattern fabrication, no source/detector
Perovskites	LiNbO$_3$, LiTaO$_3$	D, VPE	EO, AC	~3dB/cm @.633 μm	Best EO modulators, anisotropic Δn makes pattern fabrication difficult, no source/detector
II-VI	ZnSe, ZnO, CdS, etc.	D, VPE	EO, AO	<3dB/cm @.633 μm	Conventional photolithography of patterns .5-10 μm. No source/detectors
Glasses/ Polymers	SiO$_2$, PMMA	CVD, II, D, etc.	None	<1dB/cm	Lowest losses, possible Nd-glass source, difficult pattern fabrication
Misc	ADP, KDP	LPE	EO	<3dB/cm	Good EO modulation, nondurable material, no source/detector

*Free carrier modification only

LPE: liquid phase epitaxy   D: diffusion
VPE: vapor phase epitaxy   IM: ion etching
II: ion implantation   CVD: chemical vapor deposition

EO, AO, MO: electro-, acousto-, magneto-optic

of GaAlAs* cw laser source, diffused waveguides in ZnSe, and silicon APD detection with low-loss, single-mode transmission links offers the highest overall capability. An ongoing task is the assessment of capabilities offered by the developing technologies in the entire materials/fabrication area to optimize overall performance in an IOC system.

*GaAlAs is a commonly accepted notation for $GaAl_{1-x}As_x$.

WAVEGUIDE DEVICE PROPERTIES

PROPAGATION CONSTANTS IN DIFFUSED OPTICAL WAVEGUIDES

This section reviews some theoretical work performed at NELC on the determination of waveguide properties in a guide containing a graded-index boundary. The exact propagation constants obtainable in a guide containing an index gradient such as that produced by diffusion are essential for optimum device performance. Device design parameters are dependent, sometimes critically so, on the exact nature of the propagation of light in the waveguide. The determination of propagation constants in a planar graded-index waveguide is a necessary first step to fully understanding propagation in more-complex structures.

ELECTROOPTIC MODULATION OF LIGHT IN A PLANAR WAVEGUIDE FABRICATED FROM A ZINC-BLENDE TYPE CRYSTAL

Previous work on waveguide electrooptic modulators[2] at NELC dealt with the fabrication of devices in II-VI compounds such as ZnSe, which has the cubic zinc-blende type structure. This section presents theoretical calculations performed at NELC on certain aspects of device performance which arise from the confinement of the optical energy in a waveguide compared to bulk crystal electrooptic modulation.

Planar optical waveguides have been fabricated in the II-VI compounds by diffusion[3]. The diffused planar optical waveguides are fabricated by diffusing an appropriate element into single-crystal II-VI compound semiconductors to produce a composition gradient at the surface of the crystal. In those mixed crystals in which the refractive index is a function of composition, a surface layer of sufficiently high refractive index to guide light is formed. The fabrication of optical waveguides by this technique has been demonstrated for the diffusion of Se into CdS, Cd into ZnSe, Cd into ZnS, and Se into ZnS[4].

If these waveguides are to be employed in IOCs, a knowledge of the propagation velocities of the modes supported by these structures is necessary. The refractive index profile for these waveguides has been measured[5] and found to be the error function complement in agreement with simple diffusion theory. The fields in such waveguides and the transcendental equation for the propagation constants cannot be formulated in closed-form expressions involving only simple functions. Approximate values for the propagation constant can be obtained by WKB techniques or from the exact solutions for other refractive index profiles. Closed-form solutions exist for square[6], linear[7], and exponential[8] refractive index profiles.

Two diffusion profiles are of interest for diffused waveguides. The diffusion of a dopant from a large volume of gas into a crystal is described by the model of diffusion from a source of constant concentration into a semi-infinite body. The profile of the diffusant concentration for this case is an error function complement. If the diffusion is from an infinitely thin layer of the diffusant — that is, an exhaustible source — the concentration profile of the diffusant is Gaussian[9]. The refractive index profiles of interest are illustrated in figure 1. Each profile can be expressed as

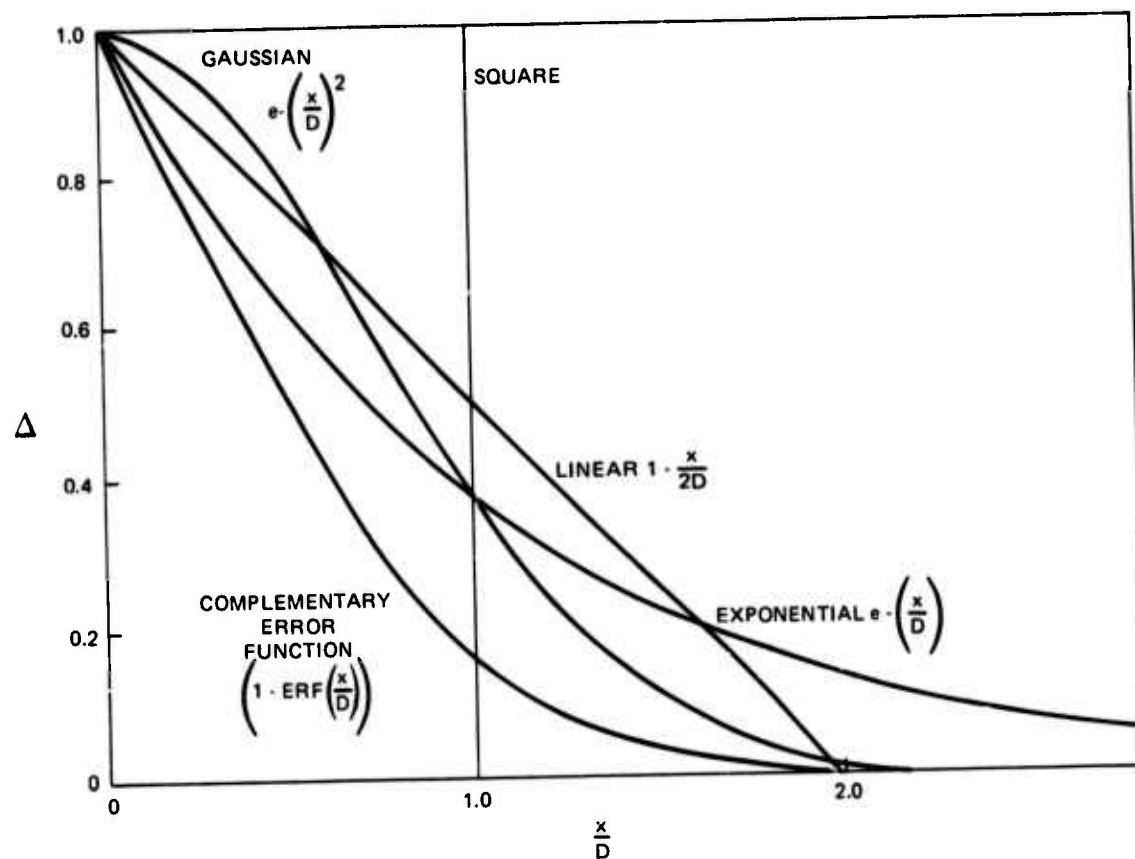$$N(X) = N_s + \Delta N \times f(X),$$

Figure 1. Refractive index vs depth.

where N_s is the refractive index of the substrate and $N_s + \Delta N$ the refractive index at the surface. The function $f(x)$ is given in figure 1 in association with the corresponding refractive index profile.

Numerical solutions for the modes propagating in the waveguides were obtained by dividing the planar structure into three regions: 1, the region outside the substrate; 2, the region in the substrate close to the surface where there is significant spatial variation in the refractive index; and 3, the bulk of the substrate. For TE modes the electric fields in regions 1 and 3 are given by the expressions

$$E_1 = A_1 \exp [g_1 X + (w t - \beta Z]$$

and

$$E_3 = A_3 \exp [-g_3 X + (w t - \beta Z].$$

where

$$g_r = \beta^2 - k^2_r$$

$$k_r = \frac{2\pi}{\lambda} n_r$$

$$r = 1, 3$$

7

and A_1, A_3 are constants. The electric field in region 2 is given by the solution of the differential equation[10]

$$E^1(X) = [k^2(X) - \beta^2] \, E(X) = 0$$

$$k(X) = \frac{2\pi}{\lambda} \, N(X) \quad .$$

The magnetic field along the direction of propagation in all three regions is given by the expression

$$H(X) = -\frac{1}{i \omega \mu} \, E'(X) \quad .$$

Solutions were obtained by assuming a value for B and for the magnitude of the electric field in region 3. The continuity of the electric and magnetic fields across the 2, 3 boundary was used to obtain the magnitude of the electric field and its first derivative in region 2 at the 2, 3 boundary. The ordinary differential equation for the electric field was integrated across region 2 to the 1, 2 boundary by use of a Miln predictor-corrector algorithm. The electric and magnetic fields at this boundary in regions 1 and 2 were then compared. A two-point interpolation iteration technique was used to find the values of g that matched the fields at the 1, 2 boundary. The boundary 2, 3 was placed at the value of X for which f(X) equals $0.1 \times f(o)$.

The accuracy of the computation was checked by comparing the propagation constant computed for a rectangular profile, by use of the above algorithm, with the exact solution. The values of g agreed to three significant places and of B to five places.

The lateral confinement of a mode in a dielectric waveguide is analogous to the quantum mechanical model of a particle in a potential well. The WKB approximation has been extensively developed for this later problem[11]. The technique is directly applicable to the present problem and yields

$$\int_0^{\gamma} \sqrt{k^2(X) - \beta^2} \, dx = (n - 1/2)\pi$$

as the determining equation for the propagation constant β where $n = 1, 2 \ldots$ and γ is the point at which the magnitude of $[k(X)^2 - \beta^2]$ equals zero.

The propagation constants for the lowest-order mode of waveguides with Gaussian, exponential, square, and linear refractive index profiles are plotted in figures 2 and 3, where

$$B = \frac{\beta - \left(\frac{2\pi}{\lambda}\right) N_s}{\left(\frac{2\pi}{\lambda}\right) \Delta N} \quad .$$

In figure 2, $\Delta N = 1\% \, N_s$ for all waveguides. In figure 3, the ΔN for each profile has been adjusted in a manner such that the integrated excess refractive index,

$$\int \left[N(X) - N_s\right] \, dX,$$

equals $0.01 \times N^1 \times D$ for all waveguides where $N^1 = \Delta N$ for the square profile.
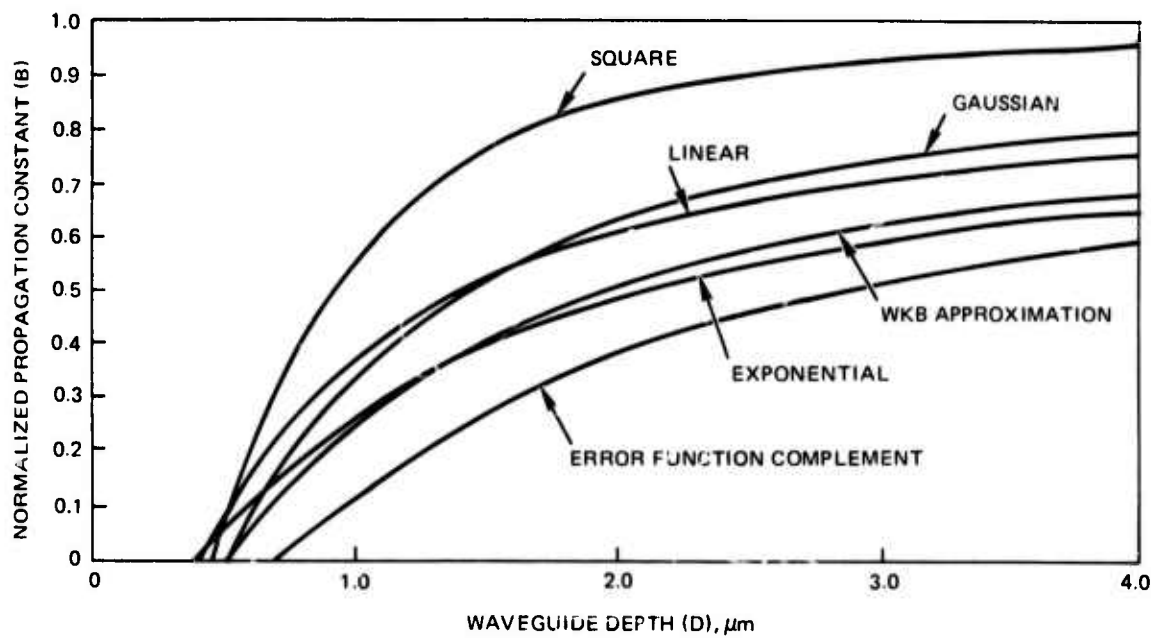
Figure 2. Propagation constant for square, Gaussian, linear, exponential, and error function complement refractive index profiles, $\Delta N = 1\% \ N_s$.
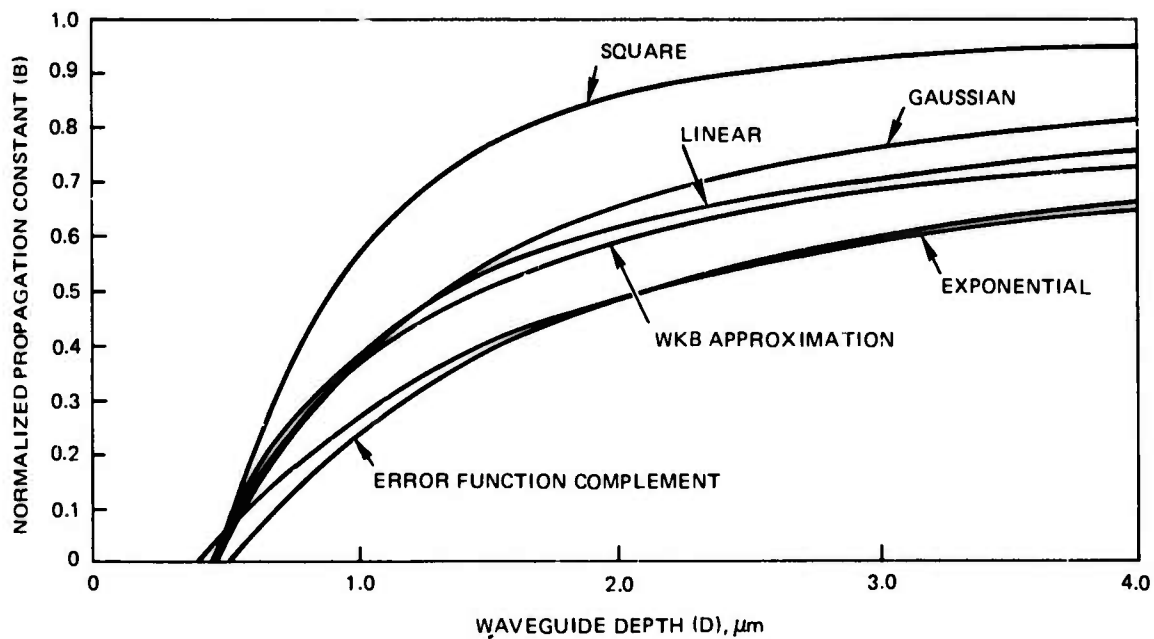

Figure 3. Propagation constant for square, Gaussian, linear, exponential, and error function complement refractive index profiles, integrated refractive index = $0.01 \times N_s \times D$.

In the case of the symmetric square waveguide, the differential equations for the electric and magnetic fields can be normalized by using the reduced quantities

$$b = \frac{\beta^2 - N_s K_o^2}{(N_s + \Delta N)^2 - N_s^2 K_o^2}$$

and

$$d = \left| (N_s + \Delta N)^2 - N_s^2 \right|^{1/2} D/\lambda$$

These quantities do not normalize the corresponding equations when the refractive index profile is not constant with depth in the guiding region. Nevertheless, calculations showed that for the range of N_s from 2.3 to 3.0 and ΔN from 0.1% to 10% N_s the use of the above reduced quantities did bring the curves for B versus D into coincidence to within two significant places. The propagation constants for waveguides fabricated in ZnTe, CdS, CdSe, and ZnS and measured at wavelengths other than 6328Å can therefore be found from figures 2 and 3 by using the expressions for b and d.

It can be seen from figures 2 and 3 that each of the profiles could be used as an approximation for estimating the magnitude of the propagation constant of another of the profiles; however, such an estimate would be only a rough approximation. The error function complement and the exponential profiles, compared on the basis of integrated refractive index profiles, yielded closely similar values of the propagation constant far from cut-off. At cut-off the discrepancy is large, and the exponential approximation yields poor estimates for the wave dimensions at cut-off.

The propagation constant for the error function complement profile was estimated by the WKB approximation and is included in figures 2 and 3. It is simpler to estimate the propagation constant by this technique than by any of the exact solutions, and the accuracy should be adequate for many applications.

Two realizations of a planar waveguide modulator are illustrated in figure 4. The voltage applied between the electrodes induces an electric field predominantly along the x-axis in the transverse electrode configuration(4a) and predominantly along the y-axis in the parallel electrode configuration (4b). While it is possible to apply the electric field along the z-axis, the significant increase in the applied voltage required for this configuration eliminates it from practical consideration.

The planar waveguide modulators discussed here are intrinsically phase modulators. If no static electric field is applied to the crystal, then TE and TM modes propagate along the planar waveguide. If a voltage is applied to the electrodes, the resulting electric field perturbs the dielectric tensor. The modes then may become mixed and the propagation constants of some or all of the modes present may change as a function of the applied field. Phase modulation will result if a mode whose propagation velocity is sensitive to the modulating voltage is launched into the waveguide. Amplitude modulation is achieved by launching two modes with equal initial phase, usually a TE and a TM mode, into the modulator. If the sensitivities of the propagation velocities of these two modes to the modulation voltage are different, then the interference of the two modes at the exit of the modulator will yield a signal which is amplitude modulated by the electric field applied to the electrodes.
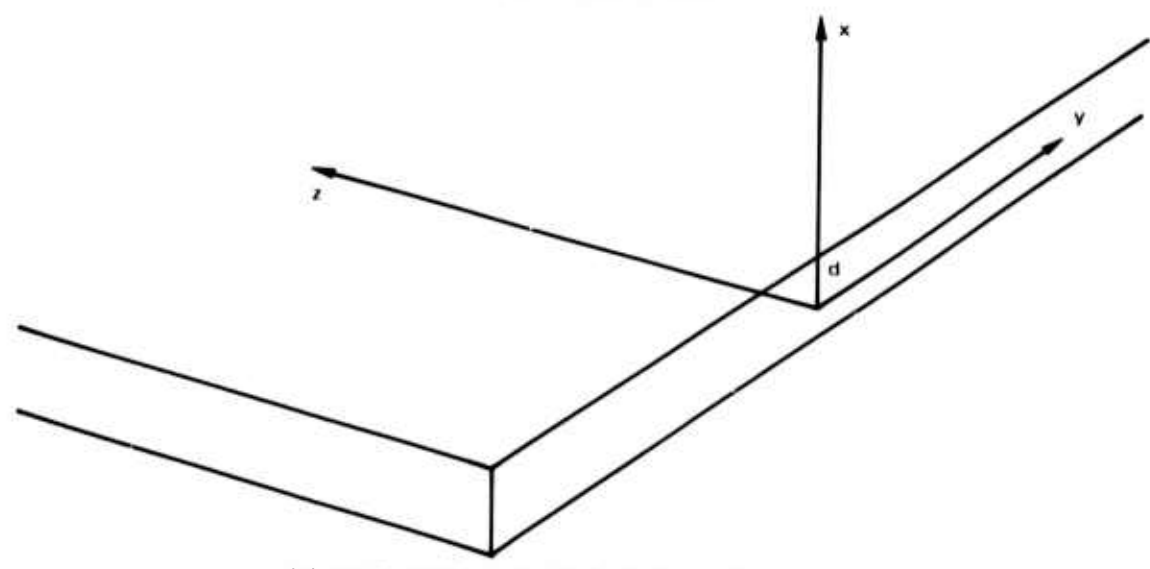
These modulators are the waveguide analog of the well known bulk modulators. A compensator must be added to the output of the modulator to achieve maximum amplitude modulation. The compensator can be eliminated if the length of the modulator
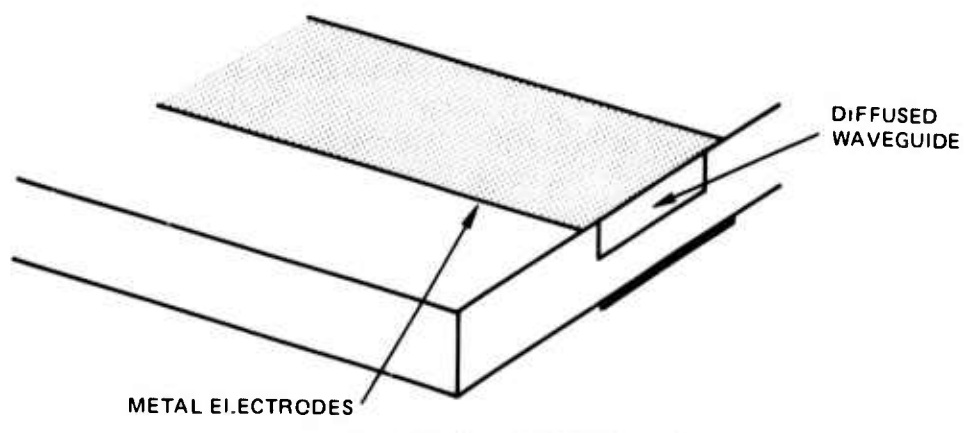
(A) TRANSVERSE ELECTRODES
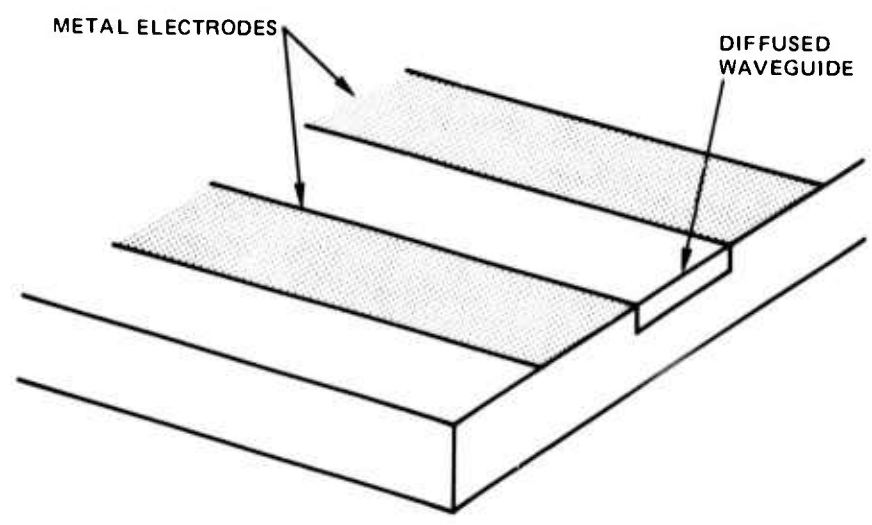
(B) PARALLEL ELECTRODES

(C) COORDINATE AXIS FOR PLANAR WAVEGUIDE

Figure 4. Electrooptical waveguide modulators.

is selected to be such that the two modes are in phase at the exit of the modulator when the voltage across the electrodes is zero.

An idealization of the geometry of the modulators is shown in figure 4c, where the propagation is assumed to be in the z direction. An electrooptically active layer, 2d thick, is bounded above and below by nonactive regions of lower refractive index. It is assumed in addition that there is no variation in the properties of the modulator or in the electromagnetic fields along the y-axis. This latter assumption would not be a good idealization of a single transverse mode channel waveguide modulator. However, the idealization is useful for those modulators described in reference 12 which have much greater width than depth and which support a very large number of transverse modes.

Under suitable circumstances the crystallographic axis could have an arbitrary orientation with respect to the waveguide axis. Any given fabrication technique, however, usually yields only a limited number of possibilities. For the cubic crystals the principal axes in the absence of an applied field are aligned with the crystallographic axes, and the index ellipsoid is

$$\frac{x''^2}{n^2} + \frac{y''^2}{n^2} + \frac{z''^2}{n^2} = 1 \;,$$

where double prime represents the crystallographic axes.

In the presence of an applied electric field $\mathcal{E}x$, $\mathcal{E}y$, $\mathcal{E}z$, the index ellipsoid deforms to become[13]

$$\frac{x''^2 + y''^2 + z''^2}{n^2} + 2r_{41} (\mathcal{E}xy''z'' + \mathcal{E}yz''x'' + \mathcal{E}zN''y'') = 1.$$

The axes of the deformed ellipsoid, the primed axes of figure 5, are rotated from the crystallographic axes. For purposes of illustration the first two cases examined by Namba[14] are illustrated in figure 5.

The dielectric tensor in the primed coordinate system is

$$\begin{pmatrix} \epsilon_{x'} & & \\ & \epsilon_{y'} & \\ & & \epsilon_{z'} \end{pmatrix}$$

Rotation of this tensor to the unprimed or waveguide axis coordinate system yields the tensor

$$\begin{pmatrix} \epsilon_1 & \epsilon_{12} & \epsilon_{13} \\ \epsilon_{21} & \epsilon_2 & \epsilon_{23} \\ \epsilon_{31} & \epsilon_{32} & \epsilon_3 \end{pmatrix}$$
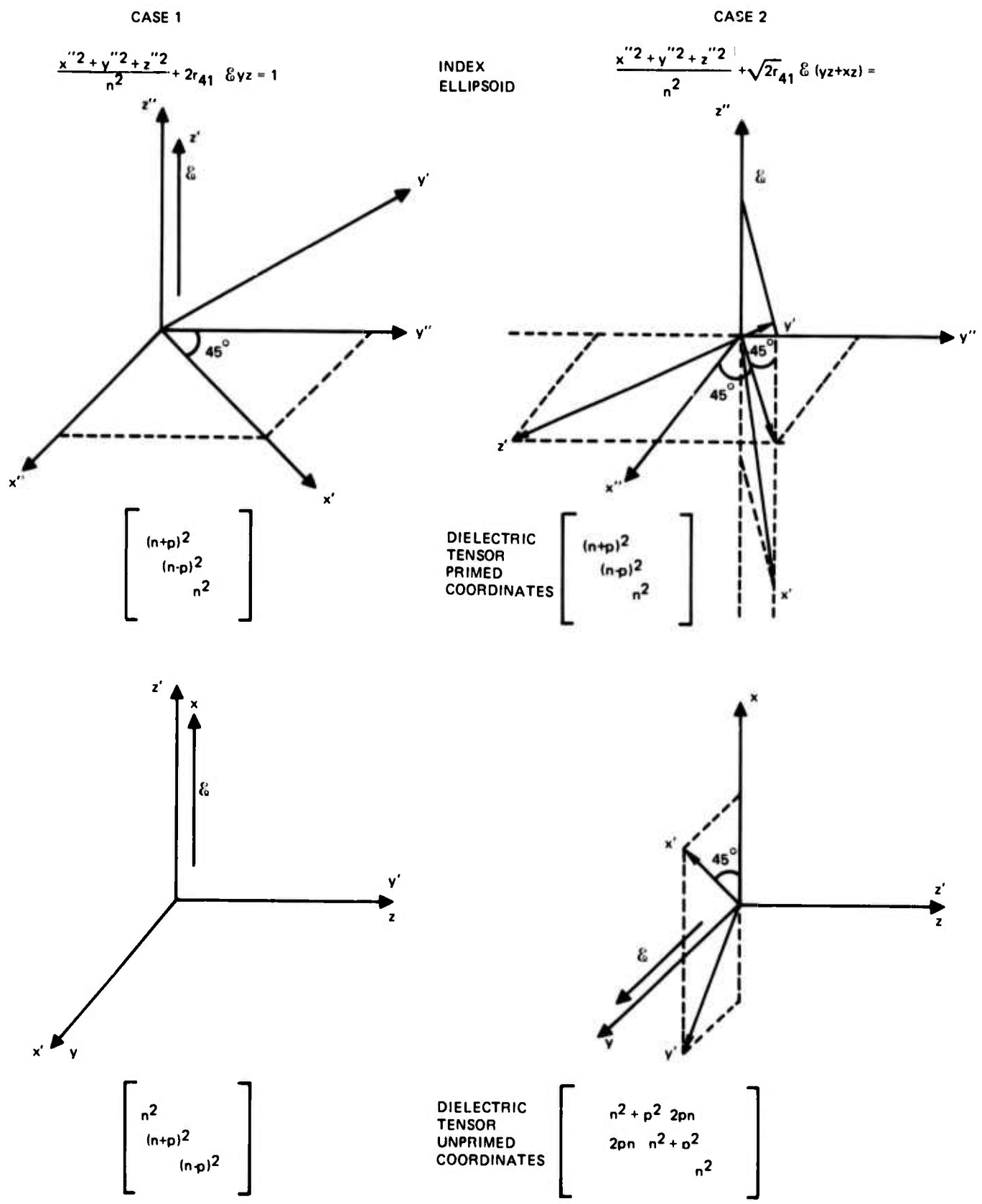
CASE 1

$$\frac{x''^2 + y''^2 + z''^2}{n^2} + 2r_{41} \, \mathcal{E}yz = 1$$

INDEX
ELLIPSOID

CASE 2

$$\frac{x''^2 + y''^2 + z''^2}{n^2} + \sqrt{2}r_{41} \, \mathcal{E} \, (yz+xz) =$$

$\mathcal{E}_0$

z'' z' y' y'' 45° x'' x'

z'' $\mathcal{E}$ y' y'' 45° 45° z' x'' x'

DIELECTRIC
TENSOR
PRIMED
COORDINATES

$$\begin{bmatrix} (n+p)^2 & & \\ & (n-p)^2 & \\ & & n^2 \end{bmatrix}$$

$$\begin{bmatrix} (n+p)^2 & & \\ & (n-p)^2 & \\ & & n^2 \end{bmatrix}$$

z' x $\mathcal{E}_0$ y' z x' y

x x' 45° z' z $\mathcal{E}$ y y'

DIELECTRIC
TENSOR
UNPRIMED
COORDINATES

$$\begin{bmatrix} n^2 & & \\ & (n+p)^2 & \\ & & (n-p)^2 \end{bmatrix}$$

$$\begin{bmatrix} n^2 + p^2 & 2pn & \\ 2pn & n^2 + p^2 & \\ & & n^2 \end{bmatrix}$$

Figure 5. Axis and dielectric tensor for cases 1 and 2.

13

If ϵ_{12} and ϵ_{23} equal zero, the modes that can propagate will remain TE and TM modes. The simplest example of this case occurs if the waveguide axis coincides with the principal axis of the deformed ellipsoid. Since the zinc-blende crystals cleave along the (110) planes, a waveguide oriented as in figure 6 is easily fabricated. Such a waveguide used in a transverse modulator becomes case 1 of figure 5. The dielectric tensor in the unprimed coordinate system for this orientation of the crystal is 13.

$$\begin{pmatrix} n^2 & & \\ & (n+p)^2 & \\ & & (n-p)^2 \end{pmatrix} ,$$

where

$$p = \tfrac{1}{2}n^3 r_{41} \mathcal{E} \quad .$$

From Maxwell's equations the differential equations for E_y and H_y within the guiding region are

$$E_y'' + (k_2^2 - B^2)E_y = 0 , \tag{1}$$

and

$$H_y'' + \frac{\epsilon_3}{\epsilon_1}(k_1^2 - B^2) H_y = 0 , \tag{2}$$
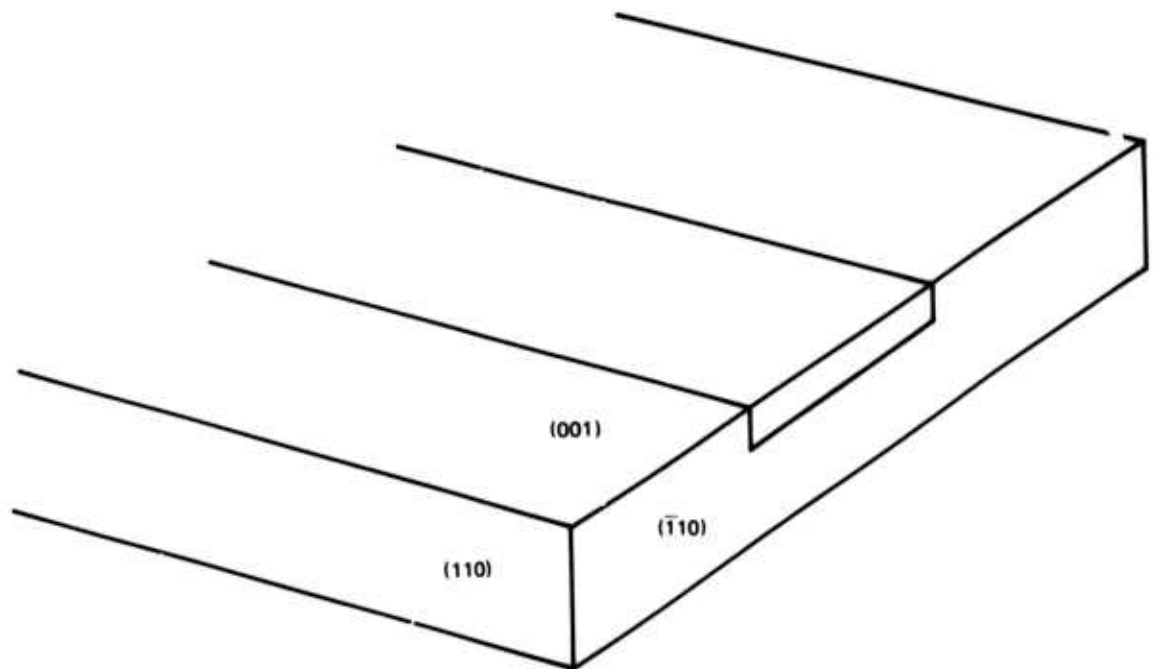

Figure 6. Crystal and optical waveguide orientation.

14

where

$$k_1{}^2 = \omega^2\mu\epsilon_1, \ k_2{}^2 = \omega^2\mu\epsilon_2, \text{ and } B \text{ is the propagation velocity.}$$

These equations are uncoupled and the modes remain TE and TM.

For the lowest-order TE mode let E_y be

$$E_y = A \cos Ux$$

within the guiding region and

$$E_y = A \cos Ud \ e^{-V(x-d)}$$

in the evanescent region. The characteristic equation for this mode is

$$U \sin Ud - V \cos Ud = 0, \tag{3}$$

where

$$U^2 + V^2 = K_2{}^2 = k_2{}^2 - k_0{}^2,$$

$$k_0{}^2 = \omega^2\mu\epsilon_0.$$

and ϵ_0 is the dielectric constant of the bounding regions.

The corresponding characteristic equation for the lowest-order TM mode is

$$\epsilon_3 U \sin Ud - \epsilon_0 \ \delta \cos Ud = 0, \tag{4}$$

where

$$\frac{\epsilon_3}{\epsilon_1} U^2 + V^2 = K_1^2 = k_1^2 - k_0^2 \quad .$$

The above equations were solved numerically for the propagation velocities of the lowest-order TE and TM modes as a function of the static electric field. The waveguide used in the numerical calculations had the properties

$$d = 0.25 \ \mu m,$$
$$n_0 = 2.58,$$
$$n = 1.01 \times N_o,$$
$$r_{41} = 2 \times 10^{-10} \text{ cm/volt.}$$

and

$$\lambda = 632.8 \text{ nm.}$$

These values were chosen in order to model the optical waveguides fabricated in ZnSe[11] and tested with a HeNe laser. The magnitude of d is not critical for this purpose.

The variation of the propagation velocity of the TE mode with the magnitude of the static electric field is plotted in figure 7. It is evident from this figure that the variation of the propagation velocity of this mode is closely linear.
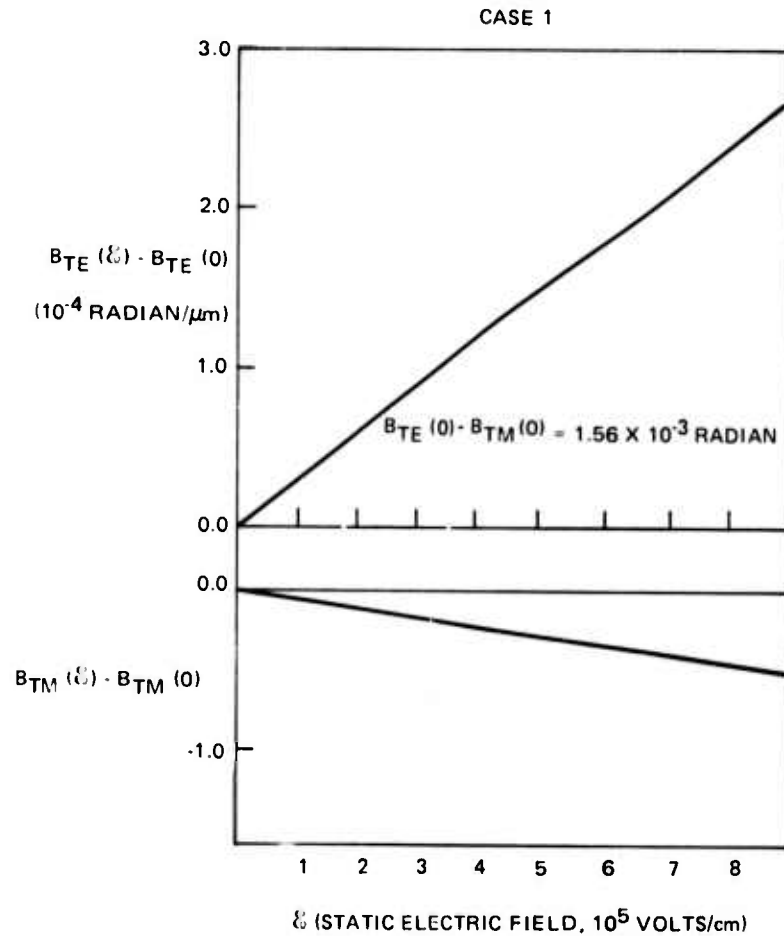

Figure 7. Differential phase delay for TE and TM modes, case 1.

The derivative of the propagation velocity with respect to the applied electric field is given by the expression

$$\frac{dB}{d\mathcal{E}} = \frac{K_1}{B} \frac{V^2 + VK_1^2 d}{K_1^2 + VK_1^2 d} \frac{dk_1}{d\mathcal{E}} = f \frac{dk_1}{d\mathcal{E}} \quad ,$$

where the factor $\dfrac{dk_1}{d\mathcal{E}}$ is the rate of change of the propagation velocity for a plane wave in the bulk material propagating in the same direction as the waveguide. The factor f varies from zero to unity as v varies from its lower bound of zero to its upper bound of K_1. The change in the velocity of propagation in the waveguide is then always less than the change in the propagation velocity in the bulk material.

16

The variation of the propagation velocity of the TM mode with applied field is also shown in figure 7. The propagation velocity of the TM plane wave in the bulk material oriented in the same direction as the TM mode in the waveguide is independent of the applied voltage.

As the second example, consider the electric field to be applied transversely for the same waveguide orientation as before. The dielectric tensor is

$$\begin{pmatrix} (n+p)^2 & & \\ & (n-p)^2 & \\ & & n \end{pmatrix}$$

in the primed coordinate system and

$$\begin{pmatrix} n^2+p^2 & 2pn & \\ 2pn & n^2+p^2 & \\ & & n \end{pmatrix}$$

in the unprimed coordinate system. The equations for E_y and H_y for this case are

$$E_y'' + \left[k^2 - B^2 - \frac{\omega^2\mu}{\epsilon_1}(2pn)^2 \right] E_y = \omega B \mu \frac{(2pn)}{\epsilon_1} H_y \tag{5}$$

and

$$H_y'' + \frac{\epsilon_3}{\epsilon_1}(k^2 - B^2) H_y = -\omega B \frac{\epsilon_3}{\epsilon_1}(2pn) E_y,$$

where

$$k^2 = \omega^2\mu (n^2 + p^2).$$

These equations are coupled, and the modes that propagate are no longer pure TE and TM modes but rather mixed modes.

These mixed modes are not coupled but are each orthogonal to all other modes that may propagate. The departure from being pure TE and TM modes is very slight if the propagation velocities of the TE and TM modes of the same order are not closely equal. In the absence of a voltage applied to the electrodes, there is no coupling, and the modes are TE and TM. Only with the application of a voltage do the modes change to what will be termed here QTE and QTM modes for quasi TE and quasi TM. The QTE mode then grows from the TE mode and the QTM mode from the TM mode with the application of a voltage to the electrodes.

The changes in the propagation velocities of the QTE and QTM modes are plotted versus the transverse electric field intensity in figure 8. The zero field intensity propagation velocity difference has been suppressed. These numerical results are for an optical waveguide of the same properties as the previous numerical example. The variation of the propagation velocity with applied field is square law to within 5%. The change in the propagation velocity with applied voltage in the numerical example can be approximated by the expression

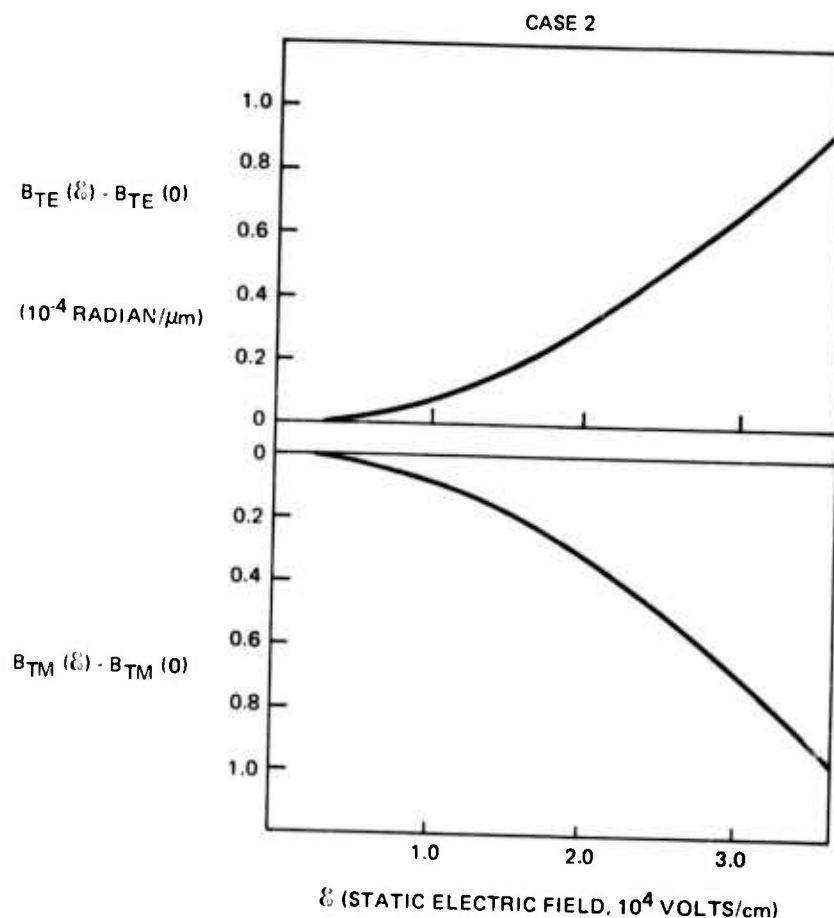$$B_{QTE}(\mathcal{E}) - B_{QTM}(\mathcal{E}) = (B_{TE} - B_{TM}) = 1.48 \times 10^{-13} \mathcal{E}^2. \tag{6}$$

CASE 2

Figure 8. Differential phase delay vs static electric field for QTE
and QTM modes, case 2.

The approximate expression

$$B_{QTE}(\mathcal{E}) - B_{QTM}(\mathcal{E}) = (B_{TE} - B_{TM}) + \frac{k_{\bar{1}}^2 B_{TE} n^4 r_{4\bar{1}}^2}{\omega U_e (U_m - U_e)} \mathcal{E}^2 \tag{7}$$

for the propagation velocity difference is derived in reference 15. For the waveguide considered, this approximation for the coefficient of the $\mathcal{E}^2$ term equals 3.74×10^{-13}. While the approximate calculation does reproduce the quadratic dependence upon $\mathcal{E}$, the magnitude of the coefficient is in error by a factor of 2.5.

In this second case the results for the waveguide modulator are substantially different than for the bulk modulator. The variation of the propagation velocity difference with applied voltage is quadratic in the waveguide modulator and linear for the bulk modulator. In the waveguide modulator the first-order effect is zero, and the second-order term dominates.

The orientation of the polarizers used for amplitude modulation is also different. In the waveguide modulator the waveguide boundaries dominate over the weak induced anisotropy and the boundaries define the TE and TM modes. The polarizer orientation required to produce amplitude modulation is 45° to the waveguide normal or the waveguide must be excited by a signal polarized in the $\langle 111 \rangle$ or $\langle \bar{1}\bar{1}\bar{1} \rangle$ direction. In the bulk

18

modulator the weak anisotropy defines the orientation of the TE and the TM modes in a manner such that the polarization of the incident light must be along the ⟨001⟩or⟨110⟩ direction to achieve maximum amplitude modulation. This direction is then at 45° to that required for the waveguide modulator. In contrast to these results the fields of the QTE and QTM modes deviate only slightly from being TE and TM modes, respectively.

The magnitude of the light intensity out of the modulator is related to the differential phase delay by the expression

$$I = \cos^2 \frac{\Gamma(\mathcal{E})}{2},$$

where the differential phase delay is

$$\Gamma(\mathcal{E}) = \left[B_{QTE}(\mathcal{E}) - B_{QTM}(\mathcal{E}) \right] \; L \tag{8}$$

at wavelength λ for a modulator of length L.

Experimental results verify the polarizer orientation and, at low modulation voltages, the quadratic dependence (11). Experimental data for the amplitude of the modulator output versus the applied voltage are reproduced in figure 9. For comparison the magnitudes of the light outputs for a linear and a quadratic propagation velocity difference dependence on applied field are also shown.
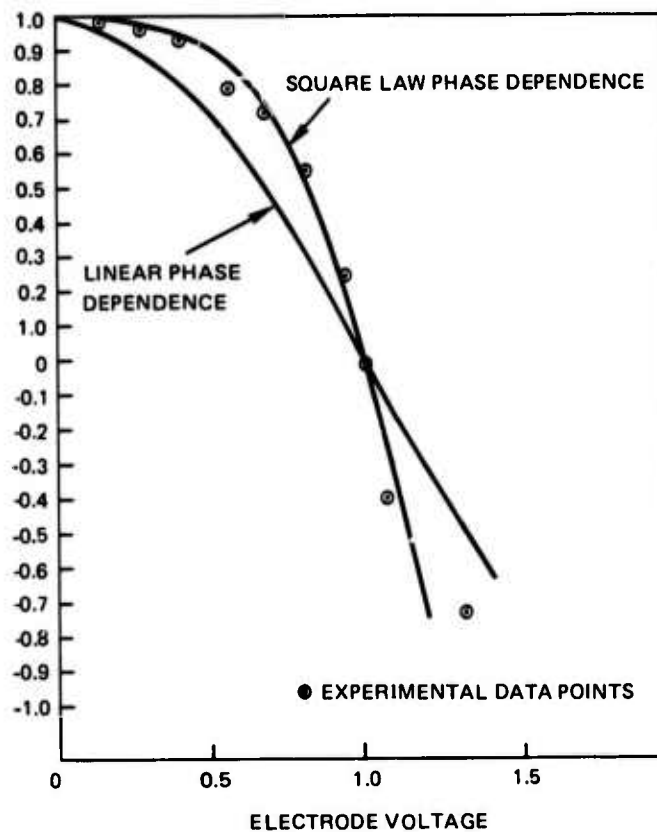

Figure 9. Modulator output vs electrode voltage (relative units), measured data, linear phase dependence, and square law phase dependence.

Numerous other special cases of the planar waveguide modulator could be considered. However, the two cases discussed here illustrate the new phenomena that can be introduced by the presence of the guiding structure. In addition, the waveguide modulators that are projected to be useful in integrated optical circuits are single-mode channel waveguides. The strong lateral confinement of such waveguides greatly complicates the analysis, and the approximate analysis which yields such simple expressions for the case considered here is not applicable.

EXPERIMENTAL FABRICATION OF FREQUENCY-SELECTIVE WAVEGUIDES IN GLASS

Previous work[15] at NELC on the fabrication of optical waveguides in glass by use of a focused cw laser beam has resulted in low loss waveguides. The process involves cw laser heating of a glass that is highly absorbing at the laser wavelength but has very low losses at the longer wavelengths used for waveguiding. This section reports progress in waveguide fabrication by cw laser heating.

Attempts were made to demonstrate frequency-selective waveguiding in channel optical waveguides. A periodic structure was imposed on the waveguide by chopping the cw laser beam by means of a mechanical chopper.

Distributed feedback should be observable in waveguides possessing a period p

$$p = \frac{\lambda}{2n} \quad (2N + 1)$$

with $N = 0, 1, 2, \ldots$. The fabricated waveguides were about 3 μm wide. Orders with $N = 0$, 1, 2 were fabricated, employing different laser powers, chopping frequencies, and exposure times.

To increase the sensitivity of the detection method, a Princeton Applied Research lock-in amplifier in the differential mode was used. The chopped light output from the near field guiding area was collected on a silicon diode, giving rise to signal A. Scattered light in the vicinity of the waveguide was collected on another silicon diode, resulting in signal B. With the aid of a variable transmission filter the amplitudes of signals A and B were adjusted until

$$A(\lambda) - B(\lambda) \sim 0.$$

The difference signal was then amplified. At $p = \lambda_1$, one would expect strong reflection of this wavelength due to the corrugated structure of the waveguide, resulting in a signal

$$A(\lambda_1) - B(\lambda_1) \neq 0.$$

In performing these experiments, it became apparent that a very high level of noise was obstructing any observable effect.

Considerable effort was spent to reduce noise, which had its main sources in many mechanical vibrations within the system. New holders for mirrors, objectives, mountings, etc. had to be specially constructed in order to eliminate the mechanical instabilities.

To date, in spite of significant improvements in the mechanical and electronic stability of the measuring apparatus, no frequency-dependent transmission has been observed. It is felt that the heating/sublimation mechanism by which the waveguides are formed may make small dimensional changes very difficult to accomplish due to the thermal conductivity of the glass.

Work on frequency selectivity is now receiving lower priority due to the start-up of work on fabricating input/output coupling structures by use of cw laser heating techniques.

PATTERN FABRICATION TECHNIQUES

Fabricating good-quality optical waveguide components by diffusion requires masking techniques which have extremely good pattern definition and repeatability. At present, two such techniques are being investigated in this program for this purpose. NELC is pursuing state-of-the-art photolithography for producing the diffusion masks in SiO_2 and Hughes Research Laboratories is investigating electron beam lithography. The following two sections describe the current status of the two approaches

PHOTOLITHOGRAPHIC FABRICATION OF COUPLED WAVEGUIDES

To date, photolithography appears to be the most useful masking technique for constructing IOC components by diffusion in the II-VI compound semiconductors. Recent work has resulted in significant improvement in the quality level of simple waveguide components and much promise with more-complex structures. Basically, contact photolithography requires very smooth surfaces for optimum reproduction of the photomask pattern. Thus, large-area ($>1 cm^2$) substrates with extremely smooth ($\sim\lambda/50$ rms) and flat ($\sim\lambda/2$) surfaces are required for the best possible pattern resolution. ZnSe used at NELC for most of the recent diffused waveguide work has a strong tendency to twin along (111) planes. The orientation of the substrates used in the work has been <100>. This results in the intersection of the (111) twin planes with the (100) top surface, resulting in very irregular surfaces after chemical polishing due to etch rate variations in the vicinity of the twinned areas. The size of the untwinned areas on a (100) crystal was typically 3 by 10 mm, although 10 by 10-mm areas could be obtained on rare occasions.

Discussions with Y. S. Park and coworkers at Wright-Patterson Air Force Base Solid State Physics Laboratory resulted in the change to (111) oriented crystals. In this orientation the face of the substrate is parallel to the twin planes, resulting in defect-free crystals of 20 by 20-mm area with an average size of 10-15 mm square. This is a significant increase in usable area ($\sim300\%$) and has resulted in rapid progress in photolithographic pattern fabrication.

Arrays of optical waveguides of 2-μm width separated by 2-μm spaces over 1 cm long have been fabricated in ZnSe by the diffusion of cadmium. Figure 10 shows oscillograph traces of the light intensity at 6328 Å detected by scanning a silicon diode across the output of an array of 4-μm, single-mode coupled waveguides separated by 5-μm spaces. The waveguides are coupled by their evanescent fields.

The intensity distribution among two coupled waveguides can be expressed as

$$I_1(z) = \cos^2 Kz$$

$$I_2(z) = \sin^2 Kz \quad,$$

where z is the propagation length and K is the coupling coefficient. In an infinite array of coupled waveguides the light intensity in the nth guide away from the initially excited ($zero^{th}$) guide is (15)

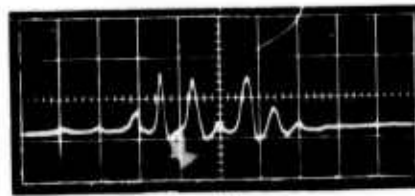$$I_n(z) = J_n^2(2Kz) \quad.$$

Figure 11 shows the relative intensities of the first few orders. From figure 10 the value of K is calculated to be approximately 0.5 mm^{-1} at 6328 Å. In addition, no scattering is visible

(a)

(b)

(c)

Figure 10. Directional coupling between parallel waveguides. Waveguide dimensions 4-μm width by 3-μm spaces. Sample length: (a) 1.70 mm, (b), 2.70 mm, (c). 3.55 mm. Waveguides fabricated by cadmium diffusion in ZnSe. Diffusion depth 2 μm.
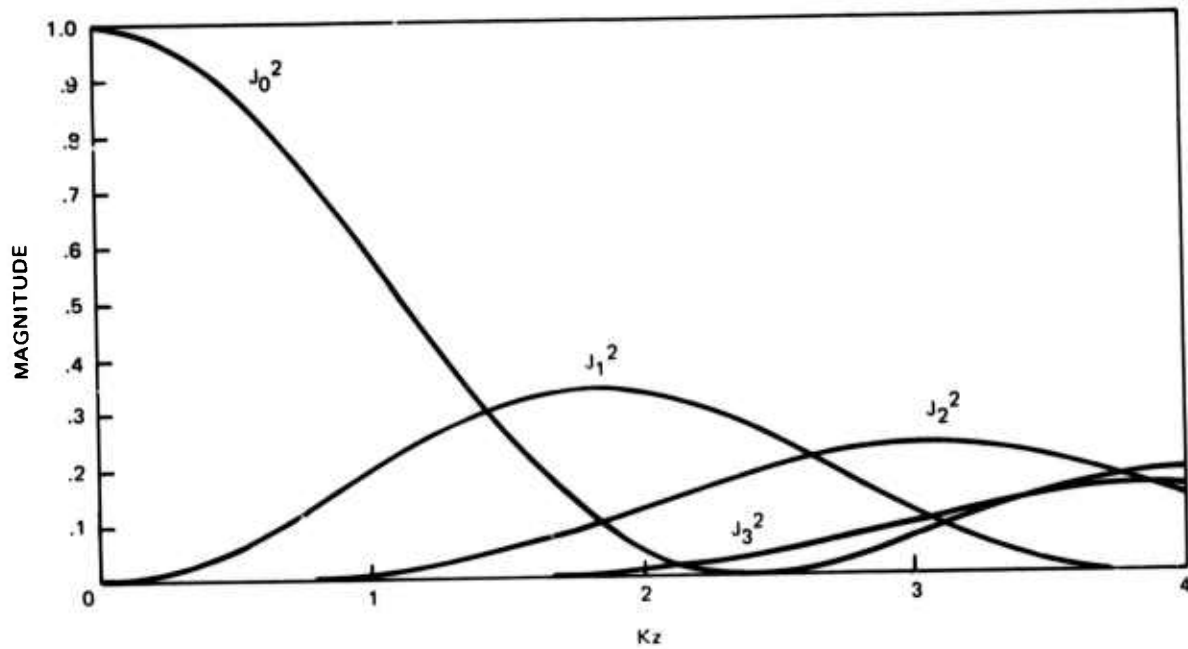

Figure 11. Magnitude of the first three orders of the ordinary Bessel function as a function of argument Kz.

from these waveguides, indicating scattering losses of less than 1 dB/cm, which should be compared to the more than 20 dB/cm of the previously reported directional couplers in GaAs (16) fabricated by ion implantation.

The significance of this work is not just that directional couplers were fabricated, but that fabrication was accomplished by conventional photolithographic techniques which are inexpensive and quite straightforward to implement. More-complex active structures are imminent and await only the acquisition of suitable masks.

ELECTRON BEAM LITHOGRAPHY

Hughes Research Laboratories (HRL) has developed several novel techniques for the fabrication of patterns suitable for the diffusion fabrication of optical waveguides. This work is oriented toward the generation of oxide diffusion masks on semiconductor substrates and employs a computer-controlled scanning electron microscope. Recent work at HRL has concentrated on the generation of closely spaced lines with extremely smooth edges etched in a SiO_2 masking layer deposited on a semiconductor substrate.

Two groups of four samples each of ZnSe, oriented (100), each with a 1000-Å layer of sputter-deposited SiO_2, were supplied by NELC for electron beam exposure and pattern delineation in the oxide layers that are used subsequently as diffusion masks for creating optical waveguides. The surfaces of some of these samples were complicated by the presence of several large crystals terminating in the surface. Patterns were delineated as much as possible in smooth areas between crystal surface structures, which were usually confined to a particular crystallite. However, in some cases the patterns intercepted such structure.

Figure 12 shows a cross section of the patterns or lines fabricated with the characteristic dimensions A (line width) and B (line spacing). Chemical etching of the SiO_2 was used after electron beam exposure and development of the electron resist. This decision was based on successful results in the past and the fact that the particular line widths required for this program are relatively large ($>1 \mu m$). The validity of the choice is shown in figure 13, which is a scanning electron micrograph (2000X) of a typical set of three etch channels in the SiO_2 films. Note that the edge roughness is undetectable, even at this magnification (probably ≤ 500 Å).
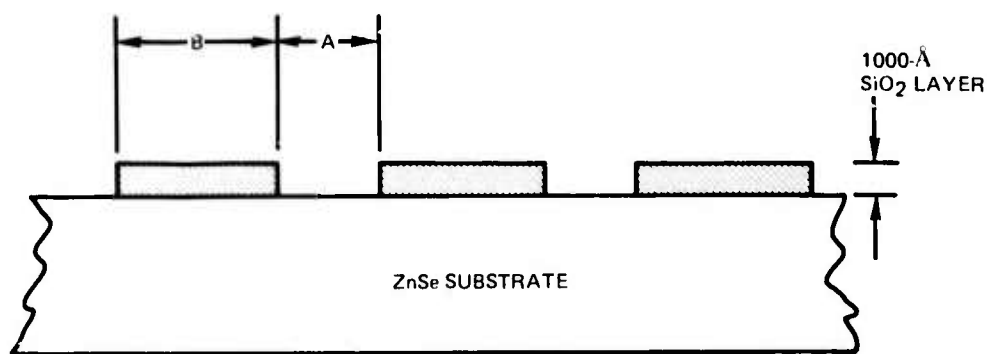

Figure 12. Cross section of the line sets fabricated, illustrating the two characteristic dimensions A and B.

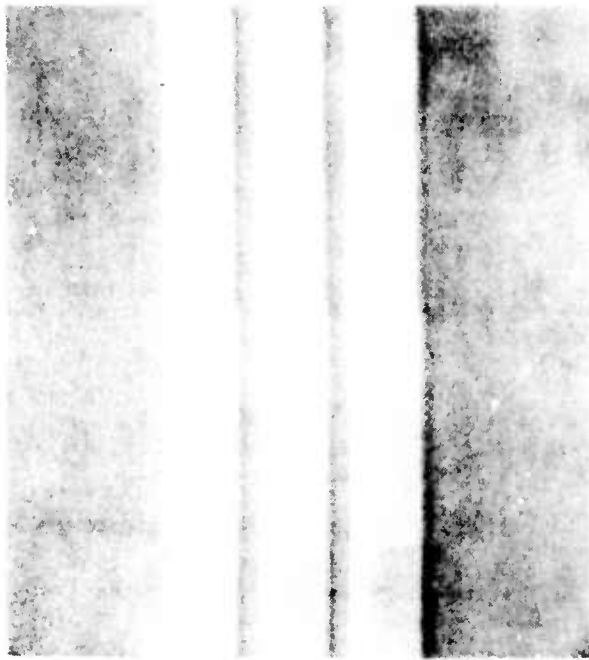Figure 13. Scanning electron micrograph (2000X) of chemically etched channels in SiO_2. (Channel width is 4.5 μm. Edge smoothness is better than 500 Å except for "charging" jog — see text.)

Only seven of the eight samples were deemed usable. Two hundred and thirty two sets of three parallel lines (0.1–2 cm long) were etched into the oxide layer of the samples. Figure 14 presents a map depicting the areas of pattern delineation on one of the samples. Photomicrographs of typical line sets are shown in figures 15 through 17.
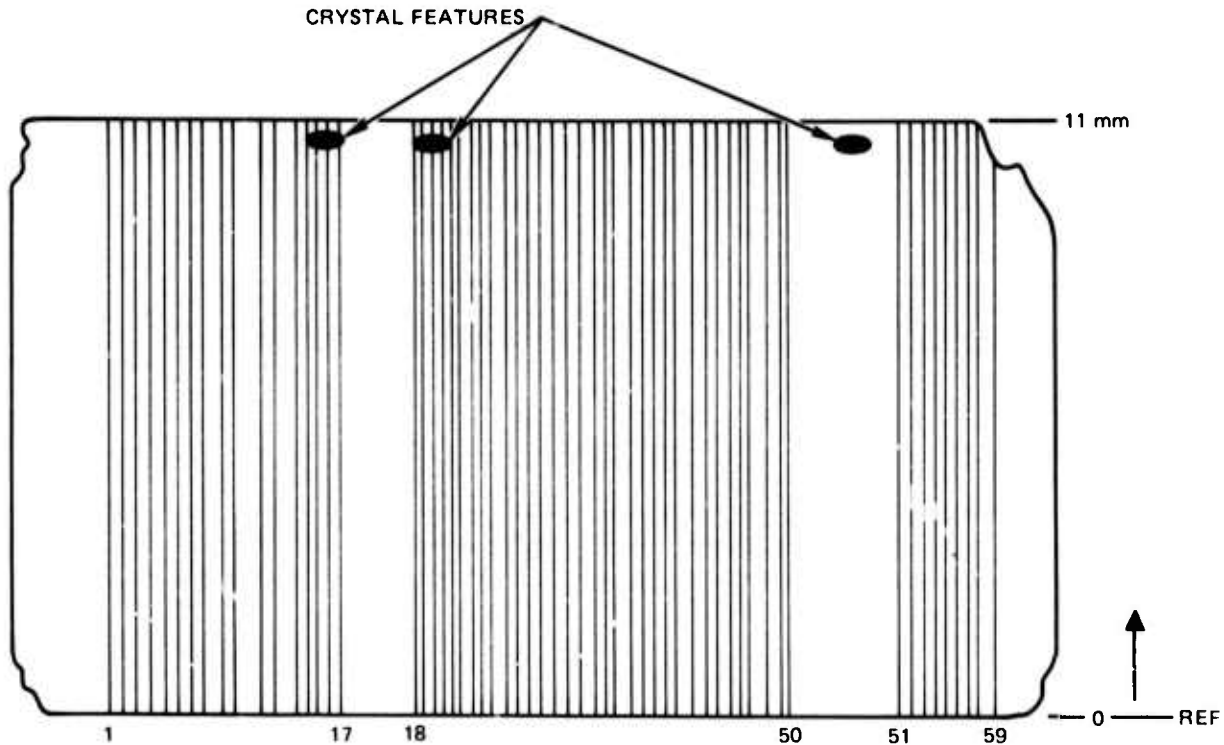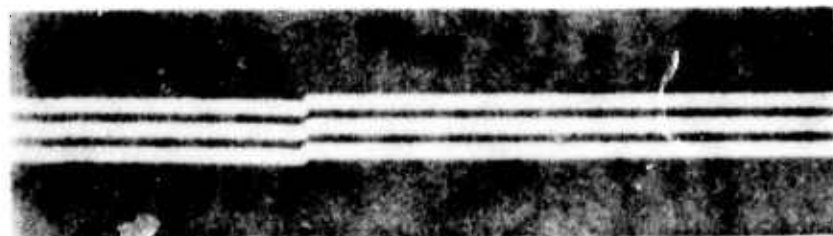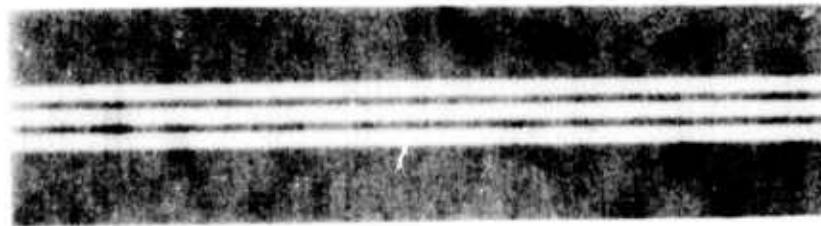

Figure 14. Map for sample 1 from group II.

Figure 15. Reflection photomicrograph (500X) of sample 1 of group 1. (a) Jog in line set 1 probably caused by sample charging. (b) Loss of pattern definition caused by excessive undercutting during etching (line set 2). (c) Line broadening caused by undercutting (line set 4). (d) Better control of etching (line set 3).

Figure 16. Reflection photomicrograph (500X) of sample 2 of group II. Lines pass through many surface irregularities (discussed in text). Photograph is typical of all line sets on this sample.

	LINE WIDTH μm	LINE SPACING μm
(e)	1.4	4.0
(d)	1.4	3.6
(c)	1.3	3.3
(b)	1.2	2.9
(a)	1.3	2.5

Figure 17. Typical 1000X photomicrographs of etched line sets on sample 1 of group II.

28

Figures 13 and 15(a) reveal an early problem that does not significantly affect light scattering in the guides. The jog in the line set may have been caused by stage translation during exposure, or more likely by specimen charging, which momentarily deflected the electron beam. The latter cause can be eliminated by coating the resist with a thin electrically conductive film.

The width of the 354 lines in the 59-line sets on sample 1 of group II is 1.3 ±0.1 μm; the length of the lines extends the full crystal width, which is 1.1 cm. The separations of the lines are constant within each line set, but vary among the sets from 2.5 to 4.0 μm in controlled steps. An effort was made to align the line sets for exposure parallel to most of the crystal defects; however, in some cases the lines unavoidably intersect crystal defects. Table 2 lists the values of the A and B dimensions for the 59 sets of six lines. Dimension A was fixed at 1.3 μm and is seen to have come out to be 1.3 ±0.1 μm after the pattern definition and etching processes were completed. Dimension B was varied from 2.5 to 4.0 μm in approximately 0.3-μm steps, with several groups of sets made at the narrowest dimension that came out to have 2.5-, 2.6-, and 2.7-μm separations. The other steps turned out to be 2.9, 3.3, 3.6, and 4.0 μm.

TABLE 2.
LINE DIMENSIONS FOR SAMPLE 1 OF GROUP II.

Line Set Number	Dimension A Line Width, μm	Dimension B Line Spacing, μm
1 to 10	1.4	2.7
1 to 17 (fig 17b)	1.2	2.9
18 to 23 (fig 17a)	1.3	2.5
24 to 28 (fig 17e)	1.4	4.0
29 to 39 (fig 17d)	1.4	3.6
40 to 44 (fig 17c)	1.3	3.3
45 to 50	1.3	2.6
51 to 56 and 59	1.4	2.5

LASER DEVELOPMENT

INTRODUCTION

Work has continued at RCA Laboratories and California Institute of Technology on developing light sources for IOC and Fiber-Optic applications. The work falls into two categories: (1) continuous room-temperature injection lasers for single-mode or multimode fibers and for IOCs; and (2) novel injection laser sources employing distributed feedback.

RCA Laboratories has addressed the first area, while the distributed-feedback (DFB) injection laser work has been undertaken by California Institute of Technology.

CW LASER DIODE RESEARCH

Excellent control of the various parameters involved in the fabrication of cw lasers has been achieved. Some half-dozen wafers have been grown, all yielding cw material. The effect of diode parameter variations on device performance has been determined in a number of cases, and acceptable limits have been established. Experiments and studies were made, using diodes developed in this program, concerning the coupling and transmission problems arising in fiber communication systems.

MATERIALS TECHNOLOGY

The DH structure with Al in the active region is now being used consistently. The temperature dependence of the threshold current density is relatively steep in these structures, as shown in figure 18. This is partly due to the use of an undoped active layer but may also be due to the Al content of the active layer. Thus, experiments are needed in which the threshold dependence is evaluated for doped active layers, as it is possible that lower threshold currents may be achieved thereby.

DEVICE DESIGN

Careful studies have been made of the temperature increase due to cw operation. It has been concluded that the first GaAlAs layer bounding the active layer exerts a crucial role in determining the junction temperature rise because of two effects: first, the thermal conductivity of GaAlAs compared with that of GaAs is reduced, and, second, the stripe geometry does not affect regions adjacent to or coinciding with the heat source. This is illustrated in a calculation summarized in figure 19. In other words, the stripe geometry reduces the effect of thermal or electrical barriers some distance from the active layer (for example, the region near the contacts), but it does not alter the thermal resistance of the GaAlAs layer. Thus, a careful control of that layer's thickness becomes important; however, one cannot reduce the thickness too much, because the optical field spreads through this layer until it reaches the highly absorbing GaAs regions. An excessively thin GaAlAs layer would lead to high absorption losses and increased thresholds.

The above problems are intimately connected with the question of beam width. Allowing more of the energy to leak out of the active region by reducing the heterojunction barrier height leads to both reduced beam widths and higher thresholds. The best units have threshold current densities on the order of 1100 - 1300 A/cm^2 and 55° beam widths (full width at 1/2 power in a direction normal to the junction). Reducing the beam width to 35°
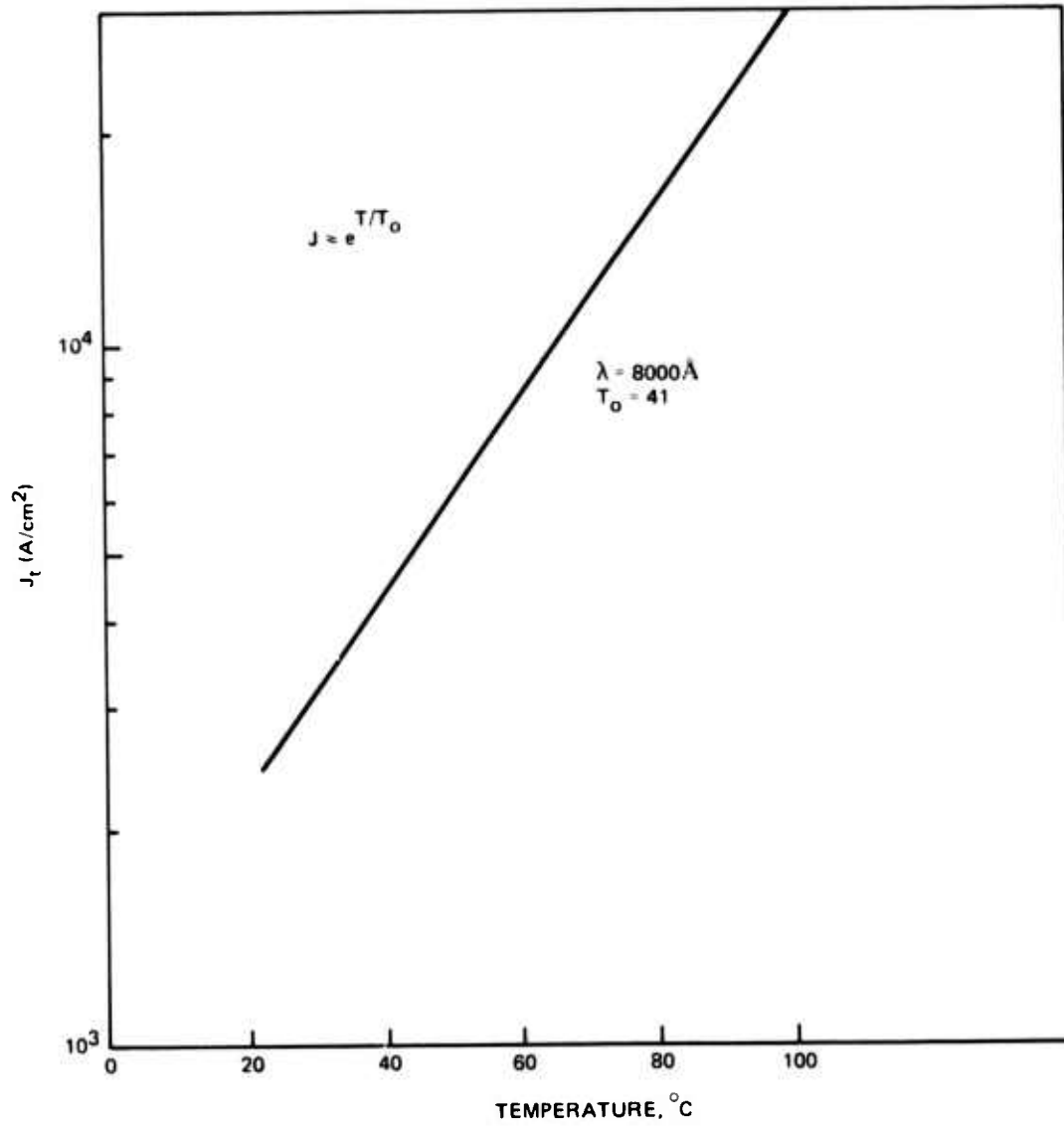
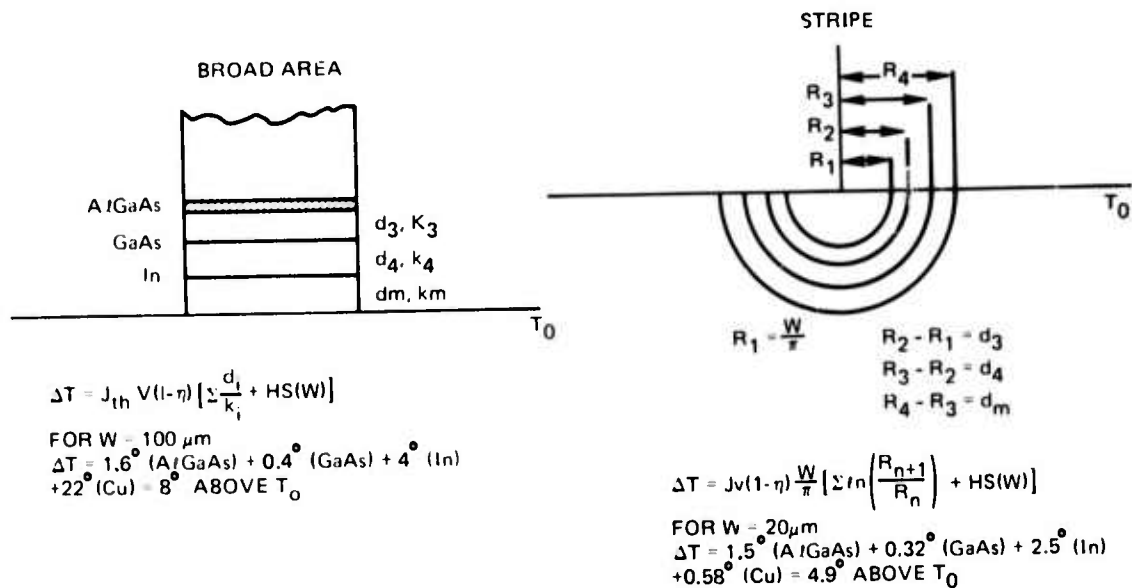Figure 18. Temperature dependence of threshold current density in undoped cavity cw lasers.

BROAD AREA

AlGaAs
GaAs
In

d_3, K_3
d_4, k_4
d_m, k_m

T_0

$$\Delta T = J_{th} V(1-\eta)\left[\Sigma \frac{d_i}{k_i} + HS(W)\right]$$

FOR $W = 100\ \mu m$
$\Delta T = 1.6°\ (AlGaAs) + 0.4°\ (GaAs) + 4°\ (In)$
$+ 22°\ (Cu) = 28°\ ABOVE\ T_0$

STRIPE

R_4
R_3
R_2
R_1

T_0

$R_1 = \frac{W}{\pi}$

$R_2 - R_1 = d_3$
$R_3 - R_2 = d_4$
$R_4 - R_3 = d_m$

$$\Delta T = Jv(1-\eta)\frac{W}{\pi}\left[\Sigma \ln\left(\frac{R_{n+1}}{R_n}\right) + HS(W)\right]$$

FOR $W = 20\mu m$
$\Delta T = 1.5°\ (AlGaAs) + 0.32°\ (GaAs) + 2.5°\ (In)$
$+ 0.58°\ (Cu) = 4.9°\ ABOVE\ T_0$

Figure 19. Calculation of temperature drops in the one-dimensional (broad area) and the two-dimensional (stripe) geometries.

has increased the threshold by a factor of about 2, which is more than can be tolerated. In view of the importance of the beamwidth in potential diode applications, a considerable effort will be devoted to the study of this problem.

DIODE ASSEMBLY

Attention has been focused recently on a technological problem in the utilization of cw lasers, a problem that arises because of two conflicting requirements. On the one hand, the laser is fragile and sensitive to ambients, so that one would want to enclose it in a sealed structure with suitable windows for the emission. On the other hand, users of these units, at the present state of development, desire to experiment with the coupling, and therefore prefer to have the facet accessible. A new design has been developed which, to some extent, satisfies these requirements. The laser diode is mounted in a deep groove milled in a copper stud, with parts of the stud extending and protecting the diode. Figure 20 shows this package mounted in a liquid-cooled heat sink. Ambient protection is at present provided by external air control, but may ultimately be provided by evaporating a suitable oxide film over the facet of the whole diode. The water cooling will be replaced by thermoelectric cooling in practical mounts. Another method of laser mounting uses the "L-mount" assembly shown in figure 21.

DIODE FIBER COUPLING*

Since fiber optical communications links are often limited in their performance by the amount of light reaching the detector, it is important to couple into the fiber as much of the light emitted by the source as possible. Several cases are of interest: LED and injection laser sources, single fibers and bundles of fibers, and large-aperture and small-aperture types of fibers. These variables can occur in various different combinations in different proposed systems. To provide insight into the problem of how to optimize coupling, measurements

*This work at RCA was sponsored by the Office of Naval Research.
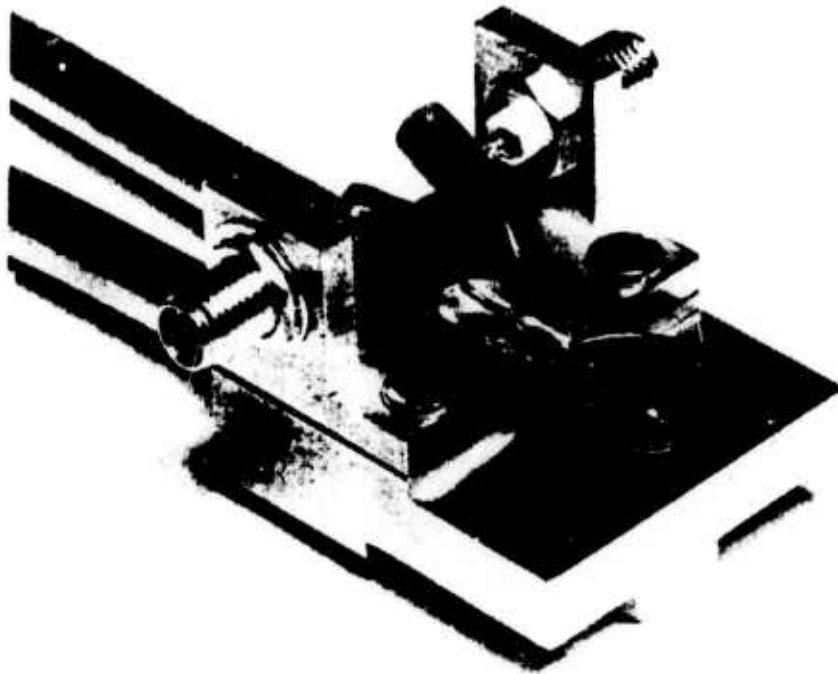
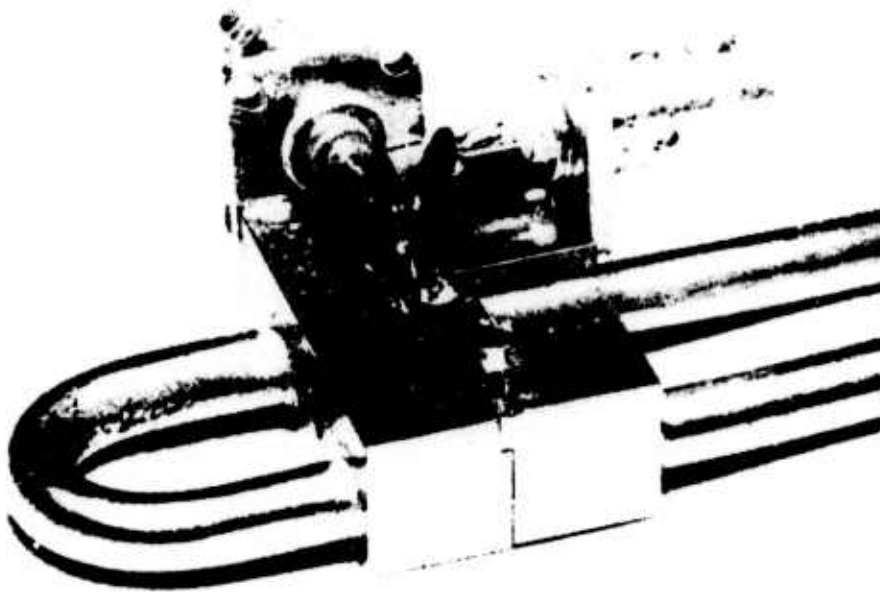Figure 20. Experimental cw laser mount for hexagonal heat-sink type laser headers.

Figure 21. Experimental cw laser mount for "L-mount" laser headers.

were made on the beam patterns of "normal" rectangular junction plane LEDs, on "stripe-contact" LEDs, and on a cw injection laser. In all cases, only an edge-emission geometry was considered, as it is believed that this geometry will prove most practical in actual systems.

The beam patterns of the LEDs show slight differences with polarization, but these are small enough that the incoherent emission can be considered unpolarized. This is not true of the laser emission, which was about 90% polarized when operated 10 - 20% above threshold.

In general, the emission pattern in the plane of the p-n junction differs from that in the plane perpendicular to the junction, and the laser pattern differs significantly from the LED patterns. For all the incoherent LEDs, the emission pattern in the plane of the p-n junction approximates the $\cos \theta$ pattern associated with a Lambertian source. However, in the plane perpendicular to the junction, the beam patterns differ significantly from a $\cos \theta$ dependence and from each other, depending on the details of the epitaxial layers and their compositions and thicknesses (see figures 22 and 23).

It is a good approximation to assume that the relative intensity at any polar angle (θ, ϕ) from the axis of the device is given by the product of the relative intensities in the corresponding angles in these two planes. With this assumption, the relative intensity distribution, averaged over the azimuthal angle ϕ, can be computed and integrated over the solid angle about the system axis. This yields the cumulative distributions shown in figure 24, along with the corresponding Lambertian source distribution. It is seen that the beam patterns from the LEDs are somewhat more forward-directed than they would be from a Lambertian source, thus showing the (weak) optical guiding of the epitaxial layers. For low cone angles, as used in coupling an LED to a small-aperture fiber by "butting" the fiber end against the emitting facet of the LED, this "beam narrowing" can result in twice as much light coupled into the fiber as would be the case from a Lambertian source. Less-directional LEDs (for example, curve (b), in figure 24) give considerably less improvement. In any case, only about 4% (−14 dB) of the light emitted from the (one) facet can be coupled into an N.A. = 0.14 fiber in this way.

Various techniques have been proposed to increase the coupling, by utilizing the light emitted into a much larger cone angle; this can be done with either lenses or reflectors. Well known principles of optics prevent this from being done without enlarging the effective source size, however. The coupling of an edge emitter, whose junction width is (or can be made) greater than the diameter of a fiber, cannot be usefully increased in this one dimension by any such optical elements. Perpendicular to the plane of the junction, where the thickness of the emitting region is only a few micrometers, the light emitted into larger beam angles than those corresponding to the N.A. of the fiber can be collected with lenses, etc, and brought within the acceptance cone of the fiber.

For best effect, lenses used for this purpose must be very small. If cylindrical lenses are used, as the above considerations suggest, the lack of focusing in the plane of the junction requires that the fiber end be as close as possible to the LED. This requires small optical elements. If, instead, spherical lenses are used, the strong aberrations associated with this geometry prevent improved coupling unless the lenses are again comparable in size to the fiber diameter. Using such small elements, we have achieved a factor-of-2 improvement in light coupling over simple butting in certain LEDs. However, for coupling into single fibers, alignment tolerances are somewhat critical.
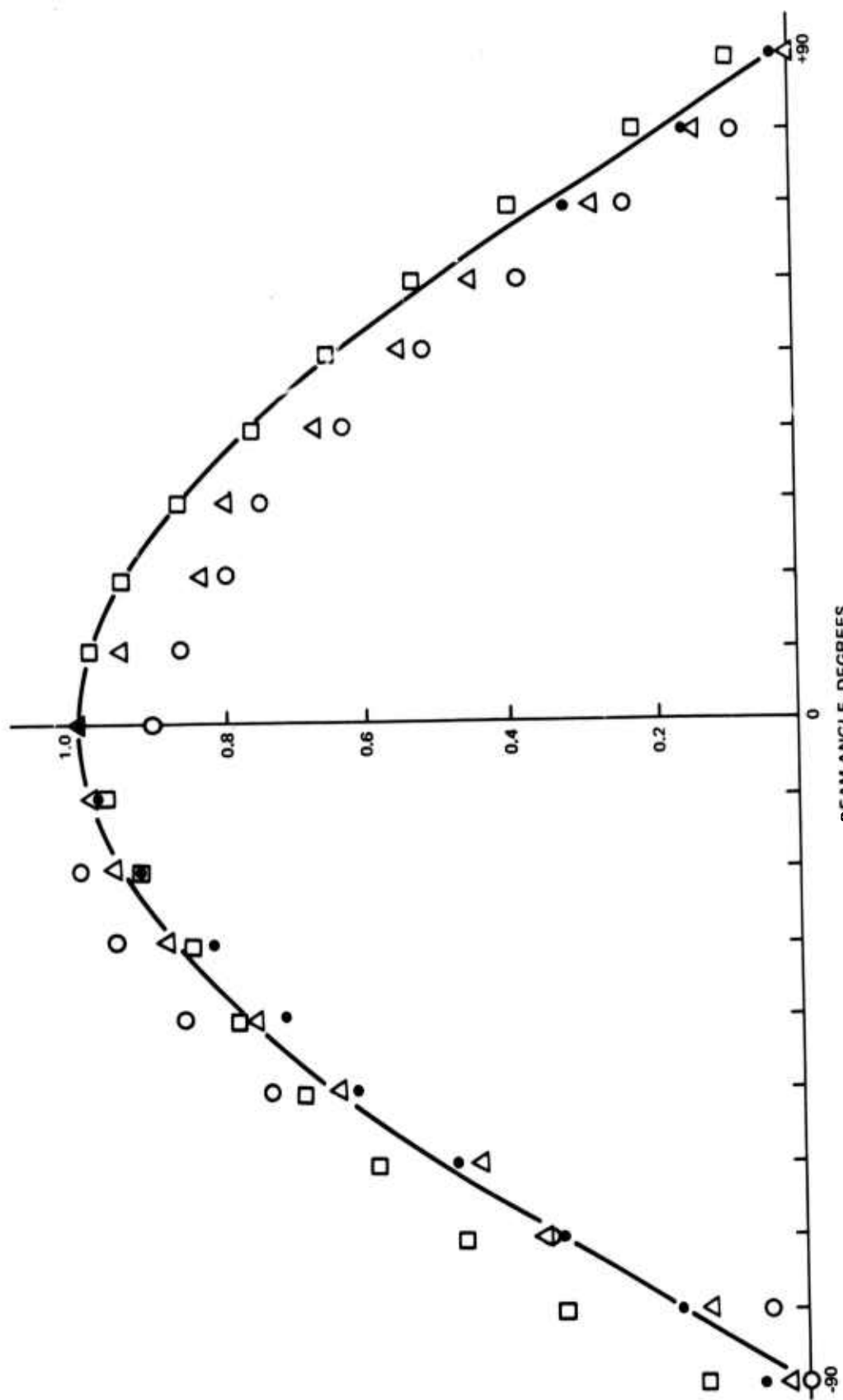
34

Figure 22. Far-field beam patterns of several LEDs in the plane of the p-n junction.
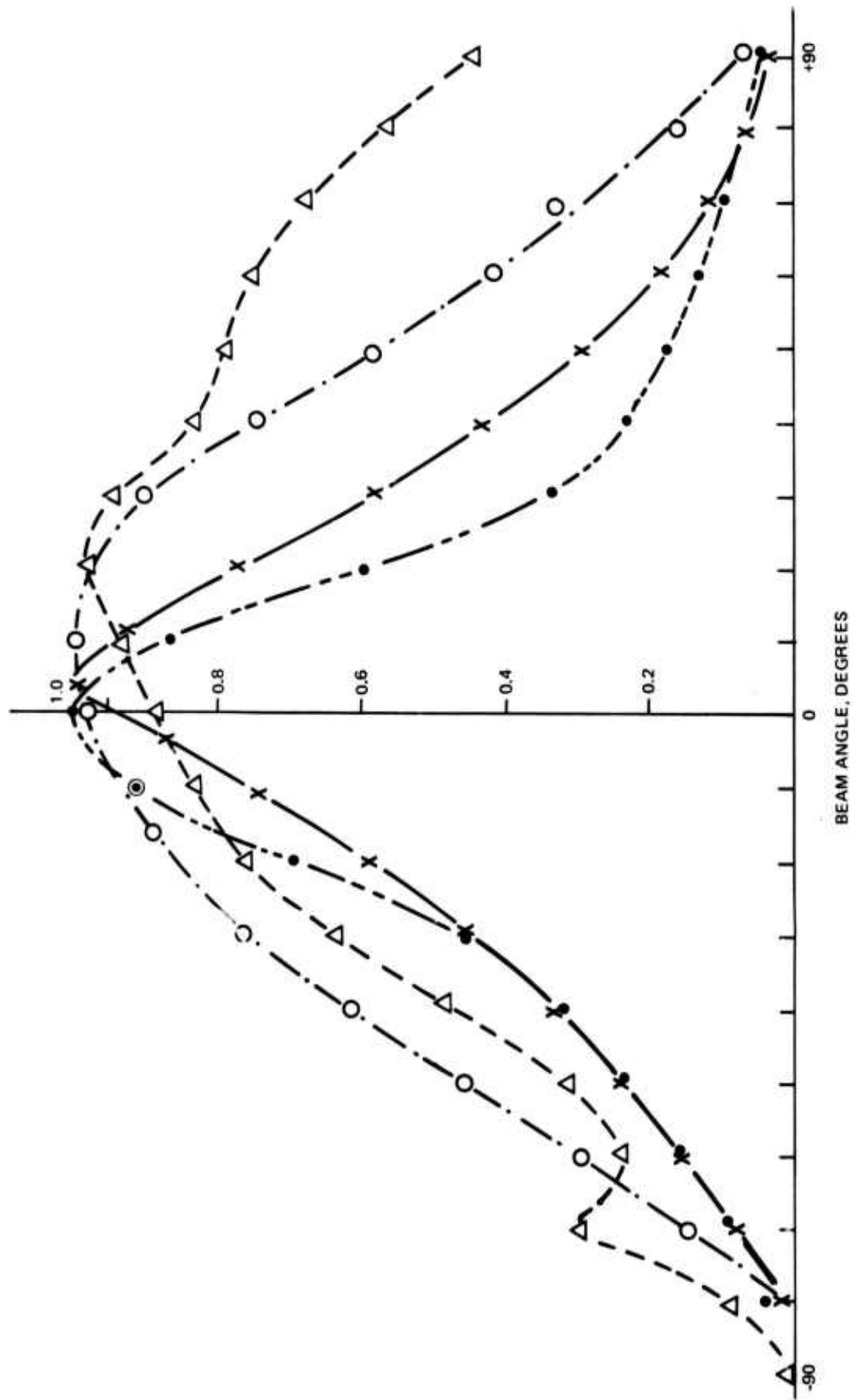
BEAM ANGLE, DEGREES

Figure 23. Far-field beam patterns of several LEDs in the plane perpendicular to the p-n junction.
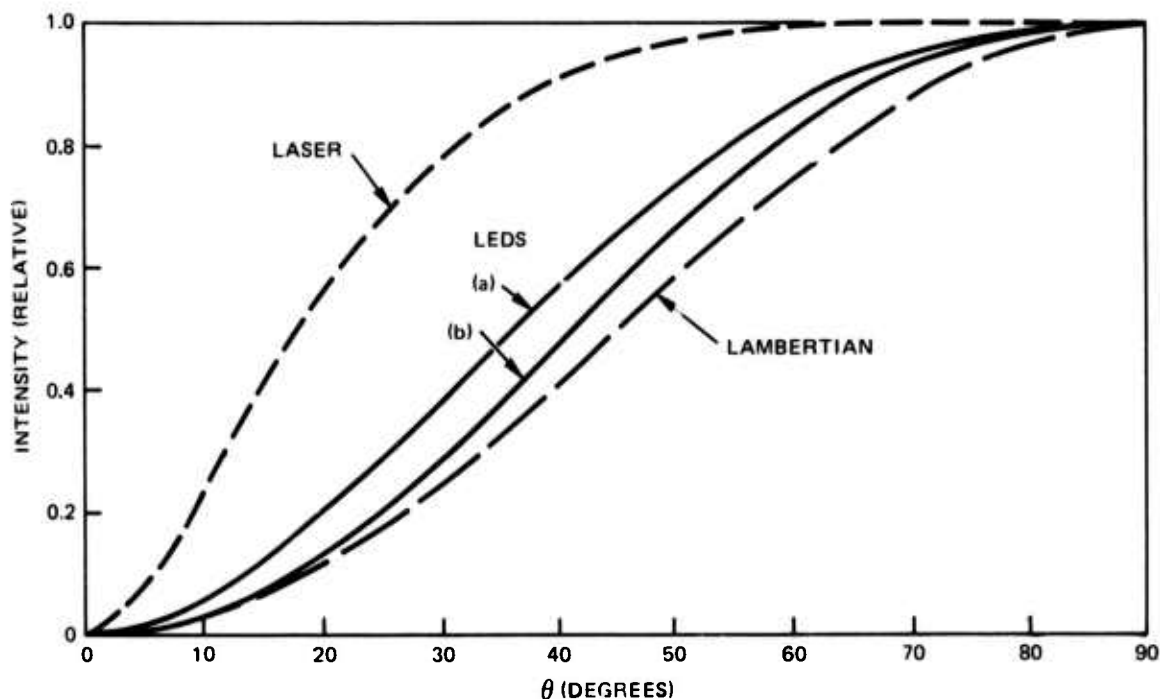
BEAM ANGLE, DEGREES

Figure 24. Fraction of emitted beam within a cone of angle θ (centered on the device axis) for two LEDs and an injection laser operating 10 - 20% above threshold. LED curve (a) corresponds to the LED indicated by the (●) points of figures 22 and 23, curve (b) to the (o) points. The corresponding Lambertian cumulative distribution is also shown.

The situation is considerably improved if one is coupling into a bundle of fibers. Now, despite losses associated with the "packing fraction" of the bundle, source magnification in both directions can be tolerated and significant improvements can be achieved by use of focusing elements. However, the improvement to be expected even here is reduced by reflection and/or transmission losses.

Present cw room-temperature injection lasers are typically multimode devices when operated 10 − 20% above threshold. It is thus more difficult to couple the output beam into a single fiber than would otherwise be the case. A typical laser has the beam pattern shown in figure 25. The calculation outlined above for LEDs, when applied to this laser, gives the results shown in figure 24. It is seen that the much more directive beam pattern of the laser permits approximately 15% of the output to be coupled into the fiber with simple butting. Simple (small) cylindrical lenses permit this to be significantly increased, with increased construction and alignment complexity.

The beam pattern of an injection laser varies with excitation level, from the broad LED-type pattern below threshold, through the "beam-narrowing" region of increasing stimulated emission as threshold is reached, to the quite sharp pattern slightly above threshold when only one mode (or a few) is oscillating. At the still higher excitation levels needed to provide optimal power output, the number of laser modes oscillating increases sharply, and the beam pattern again broadens. Coupling efficiency is, therefore, a somewhat ill-defined term for these devices.

This characteristic is illustrated in figure 26, where the coupling loss, measured as the ratio of power coupled through 1000 feet of N.A. = 0.14, low-loss, step-index fiber to the power measured into a large-area detector butted against the emitting facet of the laser, is
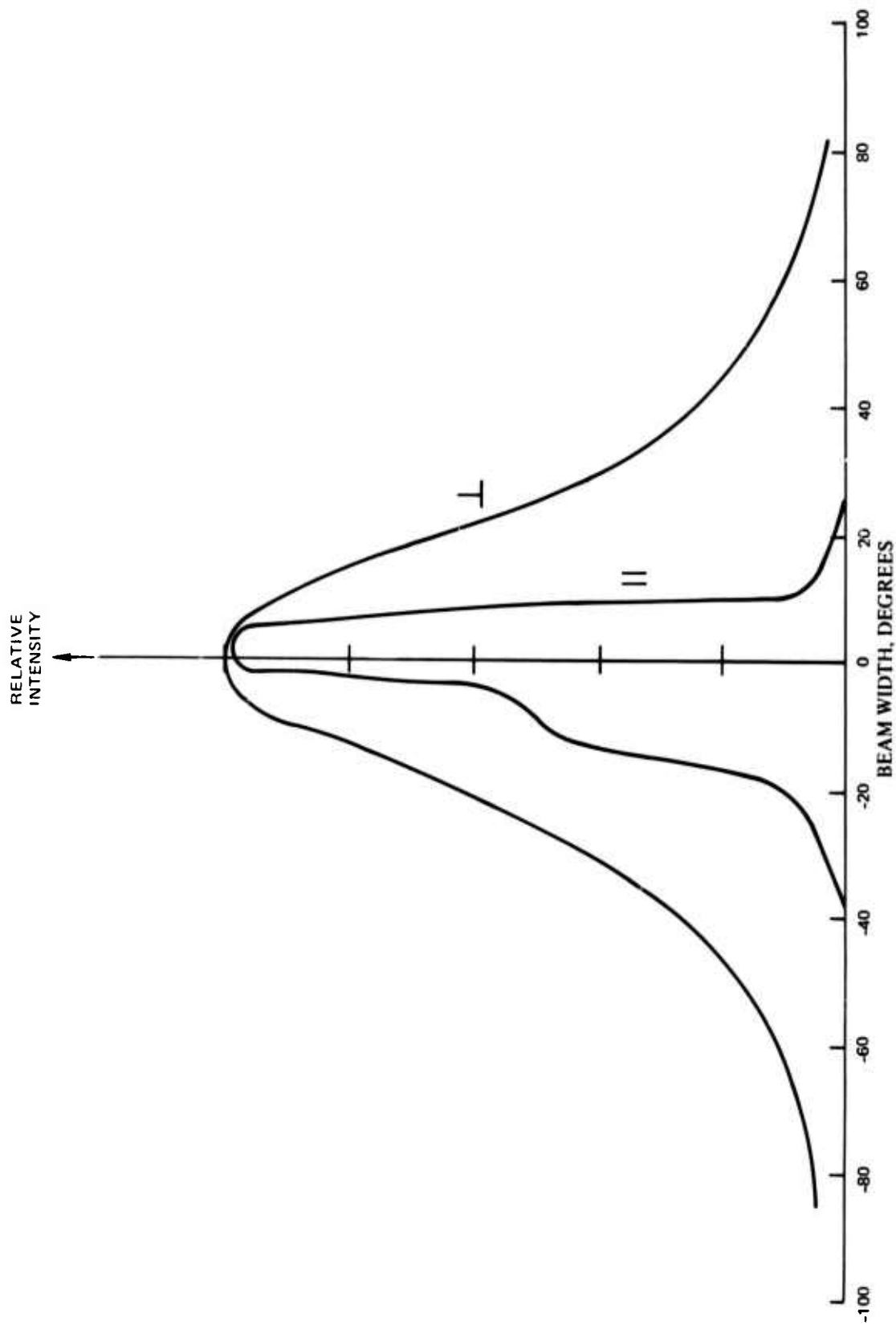
37

Figure 25. Far-field beam pattern for a cw injection laser operating 10 - 20% above threshold, in planes parallel and perpendicular to the junction plane. Only the dominant polarization is shown; emission at the orthogonal polarization was down more than 10 dB.
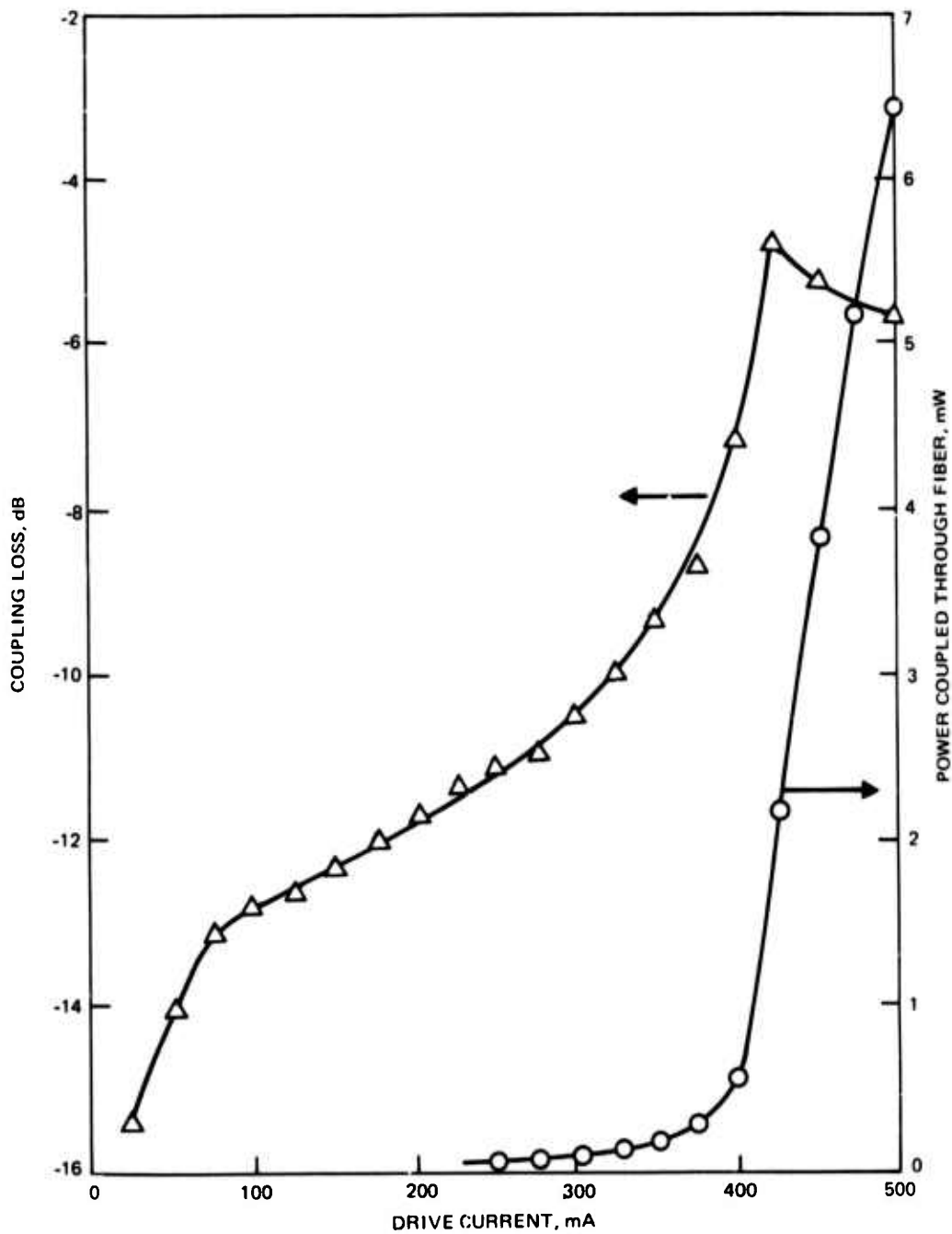
Figure 26. The coupling loss of an injection laser through an N.A. = 0.14 step-index fiber
as a function of laser drive current. The output power through 1000 feet of fiber is also shown.

plotted against laser drive current, as is the power through the fiber. The figure shows a gradual increase in coupling efficiency as threshold is approached, with a sharp rise just above threshold. At still higher drive levels, the beam pattern broadens and the coupling efficiency drops somewhat.

LIFE TESTS

Excellent progress is being made in eliminating the causes of rapid diode failure. To date the longest operating time in the testing laboratory is 2000 hours. Figure 27 shows the power output vs current curve of a diode randomly selected from a wafer at the start of the test and after 2000 hours of operation. The threshold current increase is about 10%. Therefore, the power output change with time will depend on the operating current above threshold. Unfortunately, a power failure in the testing laboratory, with a resultant "surge," destroyed all the diodes life-tested, and no additional time substantially in excess of 2000 hours could be accumulated. New facilities have been constructed with a special protection circuit which will, in the future, shut the diodes off permanently in case of power failure. More diodes are being tested and data will be accumulated.

The degradation mechanism operating in these units is predominantly facet damage. Presumably, portions of the material lose their volatile component (As), leaving a residue of Al and Ga. Early results indicate that this problem can be drastically reduced through the deposition of a protecting Al_2O_3 film on the facet. Experiments are continuing toward improved deposition techniques as the device yield at present is still not satisfactory.
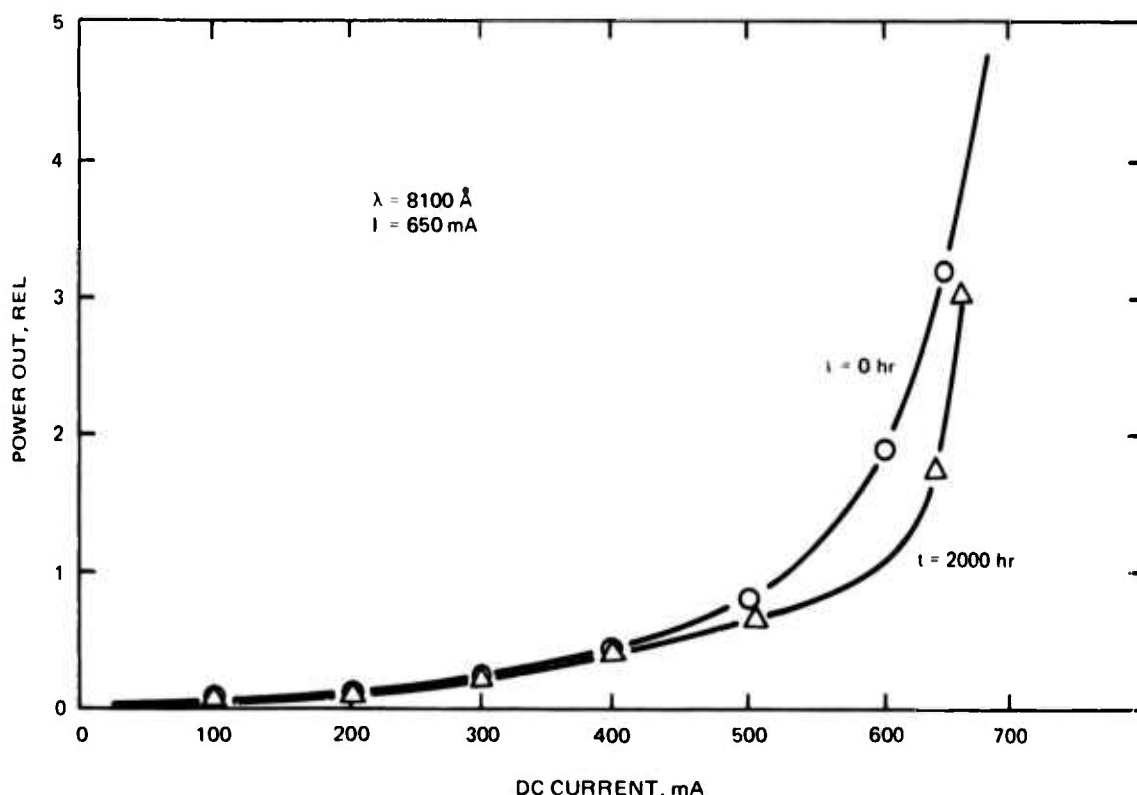

Figure 27. Power output as a function of dc current of a diode operating at room temperature before and after 2000 hours of continuous operation in dry air ambient.

DISTRIBUTED-FEEDBACK LASERS

Prompted by recent experimental [17-21] and theoretical[22] work, there has been much interest in applying the concept of distributed feedback to GaAs lasers where control of the emission spectrum is difficult. Shank et al[23] have demonstrated that one can reduce the threshold of an optically pumped distributed-feedback (DFB) laser by using a double hetero-junction (DH) rather than a single heterojunction (SH). This demonstration points the way to the ultimate realization of a DFB injection laser. Moving in this direction, Scifres et al[24] constructed a DFB single heterojunction (SH) GaAs diode laser which was electrically pumped and had threshold current densities comparable to those of normal SH diodes. The following section is a summary of the work done by A. Yariv and his coworkers at California Institute of Technology and M. Nakamura[25] of the Hitachi Central Research Laboratories in this area during this quarter.

THRESHOLD SHIFTS IN $Ga_{1-x}Al_x$ AS DOUBLE HETEROJUNCTION LASERS WITH A CORRUGATED INTERFACE[26]

Consider the double heterojunction structure in figure 28. The oscillating optical fields associated with corrugated structure obey the following coupled relations:

$$\frac{dA^-}{dz} = iK_\varrho \exp\{-2i\delta_\varrho Z\} A^+ - \alpha A^-$$

and

$$\frac{dA^+}{dz} = iK_\varrho \exp\{2i\delta_\varrho Z\} A^- + \alpha A^+.$$

where

$A^+, A^- \equiv$ right- and left-going normal mode amplitudes, respectively

$\delta_\varrho = \frac{\pi}{\Lambda}\varrho - \beta$

$\Lambda \quad \equiv$ corrugation period

$\varrho \quad \equiv$ reflection order

$\beta \quad \equiv$ propagation constant of the waveguide layer n_2

$2\alpha \quad \equiv$ intensity gain constant of the modes

$K_\varrho \quad \equiv$ coupling constant (reflection produced by the corrugations)

K_ϱ for the mth order longitudinal mode of rectangular corrugations is given by

$$K_\varrho = \frac{2\pi^2 (-1)^\varrho (n_2^2 - n_1^2) m^2}{3\varrho\lambda n_2} \quad x$$

$$(a/_t)^3 \left[1 + \frac{3}{2\pi}\frac{\lambda/a}{(n_2^2 - n_1^2)^{1/2}} + \frac{3}{4\pi^2}\frac{(\lambda/a)^2}{(n_2^2 - n_1^2)}\right]$$

In the limit $\lambda/a \gg 1$ — that is, the corrugation height being much smaller than the wavelength — the above reduces to

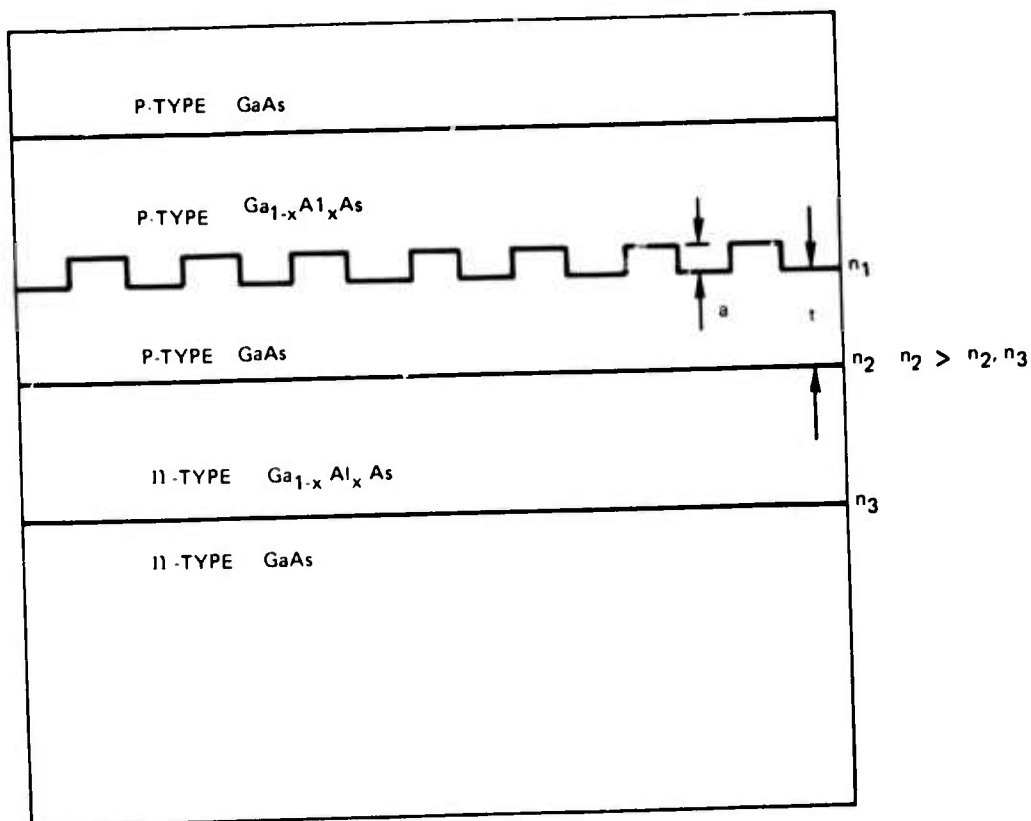$$K_\varrho \approx \frac{(-1)^\varrho \lambda a}{2\varrho n_2 t^3}$$

Figure 28. A double heterojunction laser structure with a corrugated interface.

for the lowest order which is independent of n_1. Thus, a corrugation height of a is equally effective at either an air-GaAs or GaAs $-Ga_{1-x}Al_xAs$ interface. This raises the possibility of using internal corrugations to achieve feedback where one might expect that the reflection coupling would be severely reduced due to the small index difference available. Figures 29 and 30 show numerical solutions for the threshold gain of a corrugated interface hetero-junction laser calculated from the reflection coupling constant $K\ell$[19] with $\ell = 1$. Also plotted in each figure are threshold gain curves for a GaAs laser with cleaved Fabry-Perot reflection end mirrors. Note that for $L < 1$mm and $t < 0.75$ μm, the corrugated interface lasing threshold is much lower than that of the Fabry-Perot cavity. One can also see[19] that the transverse mode number is dependent on both the threshold and the indices n_1 and n_2. Thus, control of the coupling constant K_ℓ will also control the transverse mode.
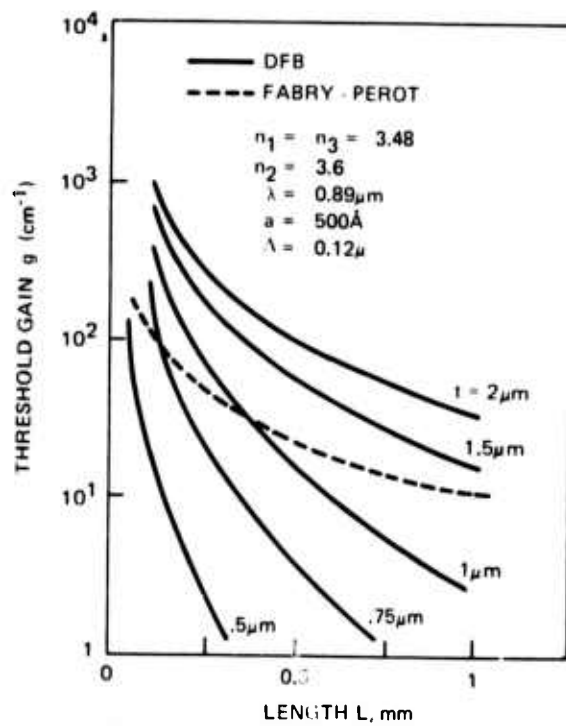
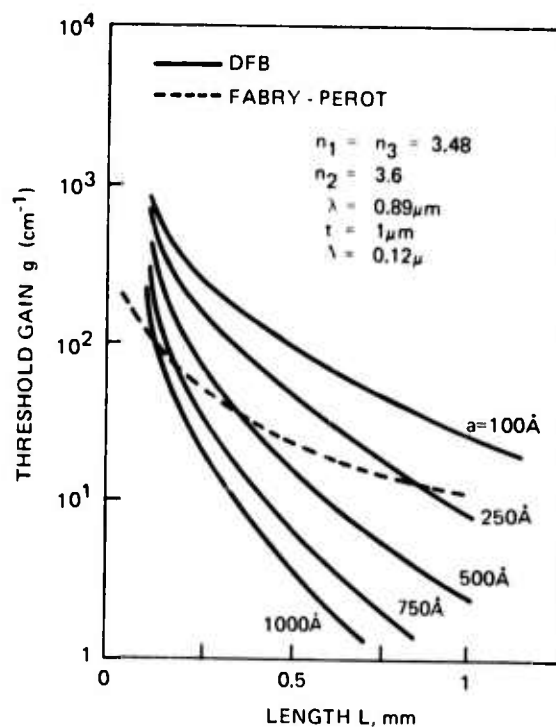Figure 29. Threshold gain vs laser length, with the guiding layer as a parameter.

Figure 30. Threshold gain vs laser length, with the corrugation height as a parameter.

FABRICATION AND ANALYSIS OF INPUT/OUTPUT
WAVEGUIDE COUPLING STRUCTURES
(UNIVERSITY OF WASHINGTON)

FIBER COUPLING TRANSITION ELEMENTS

The general problem of coupling from integrated optical circuits to fiber transmission lines is dominated by practical considerations of the small dimensions and installation difficulties involved in implementing any particular scheme. A useful method for coping with these problems involves employment of transition fibers in the manner illustrated in figure 31. The transition fiber is coupled on one end to the output of an integrated optical waveguide and on the other end to a fiber transmission line. The former coupling is effected under controlled conditions with accurate high-resolution equipment that represents part of the overall integrated optical circuit fabrication process. The latter coupling must be effected in the field with jigs of the kind that will be employed for general fiber splicing. The transition fiber has a length of perhaps 1/3 m.

A practical method for implementing the transition fiber involves use of an externally mounted fiber. This is a fiber mounted on the surface of a larger support fiber in the manner shown in figure 32. The externally mounted fiber is distributively coupled to the waveguide at one end and butt-joined to the fiber transmission line at the other. Distributed coupling is most readily effected when the externally mounted fiber has a rectangular cross section. The short thickness dimension is on the order of 1 micrometer to permit only single-mode operation in this direction. The width lies in the range of 5 - 30 micrometers in accordance with the taper that can be provided in the integrated optical waveguide. The support fiber has a width of 50 - 100 μm. This dimension is established by considerations of the convenience with which the waveguides can be separated on the integrated optical substrate.
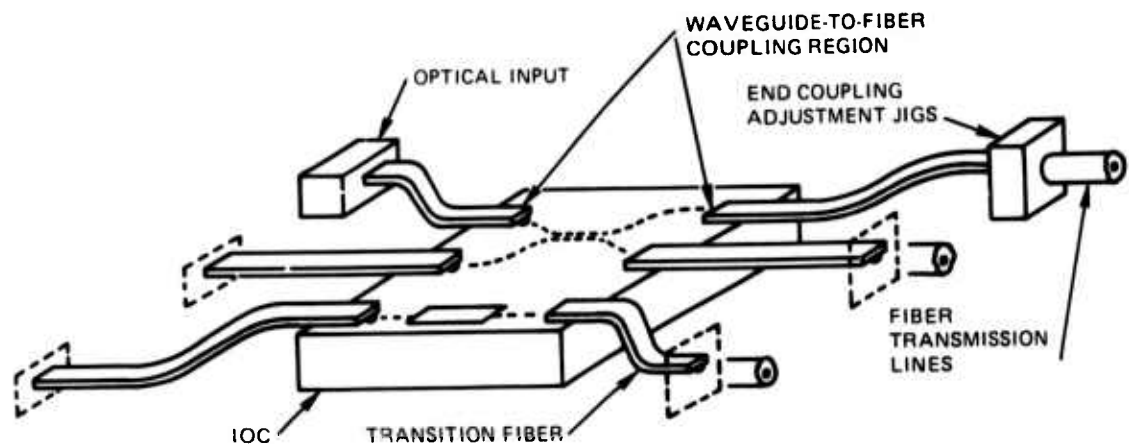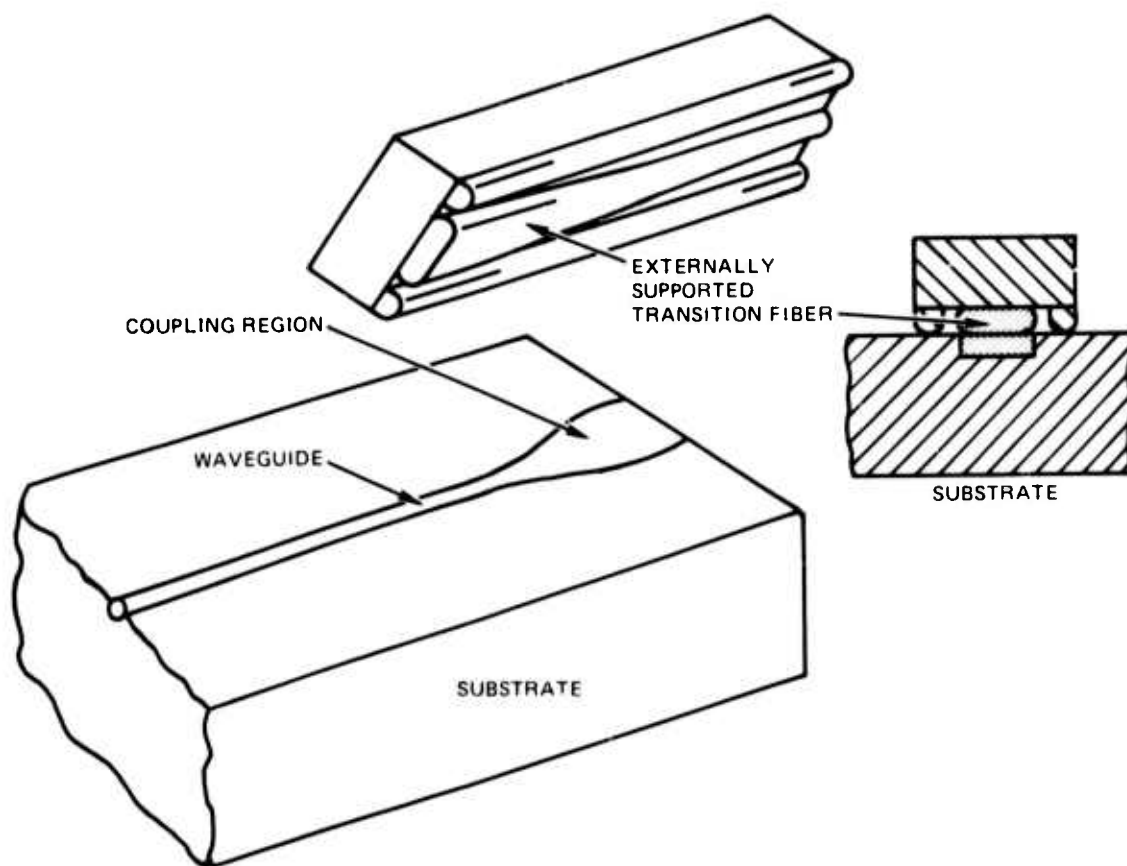

Figure 31. IOC-to-fiber coupling.

44

Figure 32. Waveguide-to-fiber transition.

Distributed coupling can be provided with the aid of tapered films or variable-period periodic structures in the manner illustrated in figure 33. The effectiveness of these structures has been established on an analytic basis, and further research will be directed toward implementing these structures and evaluating potential sources of practical difficulty. The butt-joined end of the taper will require a circular output end for the transition fiber. This may be accomplished by altering the cross section of the externally mounted fiber before or during the fabrication process as indicated in figure 35 or by providing a second coupling region. Figure 34 illustrates how the second coupling step may be accomplished with a second externally mounted fiber positioned either on a separate support fiber or on the same one. Following fabrication of the coupling regions, the externally mounted fibers will be coated for protection against dust and other sources of optical transmission loss.

Two topics relevant to implementation of the coupling scheme outlined above are discussed in this section. The first concerns the solution of coupled-mode equations when the propagation constant in two coupled waveguides varies linearly with opposite slope. The major result is a relatively simple asymptotic form for the power coupled from one guide to another. This expression shows that virtually complete coupling occurs so long as the coupling coefficient exceeds some minimum value and so long as the coupling region is of sufficient length. Exact knowledge of the average mode propagation constants is not required. The second topic is a review of the experimental results achieved so far. Externally mounted fibers have been fabricated and preliminary coupling measurements have been performed.
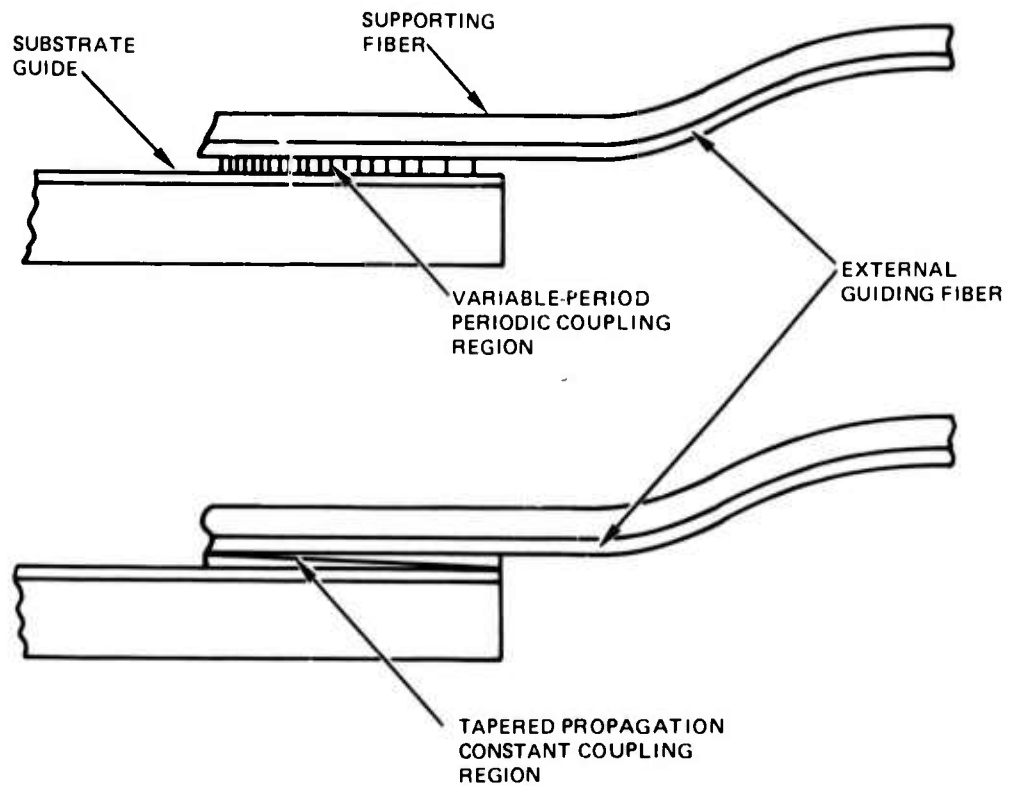
Figure 33. Concepts for coupling between substrate guides and fibers.
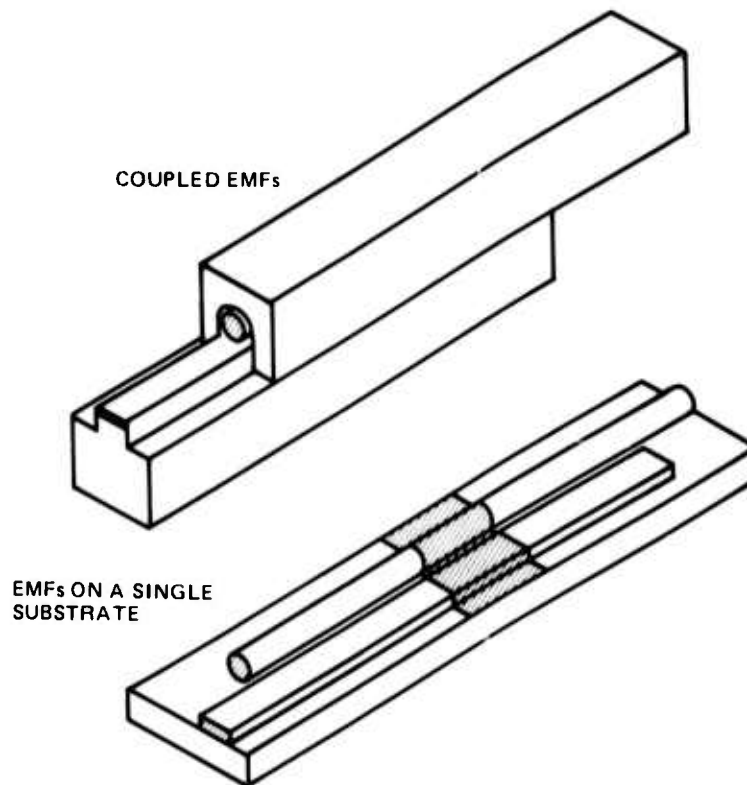

Figure 34. Two methods for obtaining externally mounted fibers (EMFs) with circular output cross sections.

DESIGN OF DISTRIBUTED COUPLING STRUCTURES

Apart from the practical problems of fabricating coupling structures between optical guides, there are conceptual design questions which deserve study. Even if the coupling and propagation parameters can be controlled approximately in the fabrication process, there exists the question of what the parameter values should be in order to achieve efficient couplers with predictable performance. Two aspects of this design question have been studied; the first concerns minimizing the effect of uncertainties and variations in parameter values on coupler performance, and the second concerns optimizing the parameters when their values can be accurately controlled. Achieving an effective coupler in a minimum length is an example of a design objective.

Under assumptions which are widely applicable, the coupling of power between guided modes can be described in terms of the so-called coupled-mode equations, and this formalism has been the subject of the present study. Particular attention has been paid to obtaining coupler designs which are insensitive to the parameters of the fabricated device.

SOLUTIONS OF THE COUPLED-MODE EQUATIONS

The particular model considered is described by the coupled-mode equations in vector form for propagation in the z variable:

$$\frac{d\underline{a}(z)}{dz} = i \begin{bmatrix} k_1(z) & c_{12} \\ & \\ c_{21} & k_2(z) \end{bmatrix} \underline{a}(z), \quad \underline{a}(z) = \begin{bmatrix} a_1(z) \\ \\ a_2(z) \end{bmatrix} , \tag{9}$$

where $a_1(z)$ and $a_2(z)$ are the individual mode amplitudes, and $k_1(z)$, $k_2(z)$, c_{12}, c_{21} are the respective propagation constants and coupling coefficients. A constant complex coupling coefficient is assumed, $c_{12}=c_{21}^*=c$. It is also necessary to assume that $|c| \ll k_1, k_2$. The $k(z)$ are taken to vary linearly at rates set by a parameter $\gamma > 0$ introduced through the relations

$$k_1(z) = k_0(1+\gamma z), \text{ and } k_2(z) = k_0(1-\gamma z) . \tag{10}$$

Exact phase match occurs at $z = 0$, where both propagation constants equal k_0. Approximate phase match and significant power transfer occur over a distance inversely proportional to γ and centered at $z = 0$. For sufficiently large z, say for $0.2 < |\gamma z|$, the phase mismatch prevents power exchange between modes. In physical couplers the point $z = 0$ may not be known, but this introduces effects that are not central to the present analysis.

The differential equations are further reduced by treating the slowly varying mode amplitudes $\underline{A}(z)$ by writing $\underline{a}(z)$ as

$$\underline{a}(z) \equiv \exp(ik_0 z) \cdot \underline{A}(z) . \tag{11}$$

The independent variable z is reduced to dimensionless form by defining

$$x \equiv \sqrt{2\gamma k_o} \cdot z \ . \tag{12}$$

To distinguish the mode amplitudes as they are dependent on z or x, we use the notation $B(x)$ with the equivalences

$$\underline{A}(z) \equiv \underline{B}(\sqrt{2\gamma k_o}\, z) \equiv \underline{B}(x) \ . \tag{13}$$

With these changes of variables the coupled first-order equations become

$$\frac{d\,\underline{B}(x)}{dx} = i \begin{bmatrix} x/2 & c/\sqrt{2\gamma k_o} \\ \\ c^*/\sqrt{2\gamma k_o} & -x/2 \end{bmatrix} \cdot \underline{B}(x) \ . \tag{14}$$

Further differentiation yields the separated second-order equations:

$$\frac{d^2 B_1(x)}{dx^2} + [x^2/4 + \nu - i/2]\, B_1(x) = 0 \tag{15}$$

and

$$\frac{d^2 B_2(x)}{dx^2} + [x^2/4 + \nu + i/2]\, B_2(x) = 0 \ ,$$

where $\nu \equiv |c|^2/2\gamma k_o$ is an important parameter which determines the form of the solutions. The second-order equations are in a standardized form of the equation for the parabolic cylinder functions [27] which is

$$\frac{d^2 w(x)}{dx^2} + [\,x^2/4 - a]\, w(x) = 0 \ . \tag{16}$$

For the present problem the upper sign applies, and the parameter, a, takes on a different value for each of the two modes; denoting these as a'_1 and a'_2, respectively (not the mode amplitudes), we have

$$a'_1 \equiv -\nu + i/2 \qquad a'_2 \equiv -\nu - i/2 \ . \tag{17}$$

The mathematical problem now is to find solutions for $B_1(x)$ and $B_2(x)$ in terms of the parabolic cylinder functions for parameter values a'_1 and a'_2. These solutions must together satisfy the coupled first-order equations.

The power in each mode is given by the squared magnitude of any of the mode amplitudes. For real k_1 and k_2 and for the stated forms of the coupling coefficients the total power will be constant. That is,

$$P_i(z) \equiv |a_i|^2 \equiv |A_i|^2 \equiv |B_i|^2 \qquad i = 1, 2 \tag{18}$$

48

and

$$P_1(z) + P_2(z) = \text{constant} \ . \tag{19}$$

For an initial condition the usual assumption is made that all the power is in one mode. Specifically, let $P_1(z \to -\infty) = 1$ and $P_2(z \to -\infty) = 0$. The corresponding phase of the mode amplitude may be arbitrary.

Of the parabolic cylinder functions standardized by Miller,[27] the ones appropriate to this problem are the two independent solutions he denotes by $E(a,x)$ and $E^*(a,x)$.[27] The properties listed in reference 27 for these functions assume that the parameter a is purely real. For the present problem both values, a_1' and a_2', are complex and some of the listed expressions cannot be used without being generalized to the case of complex a. This generalization can be effected, however, and for the specific values of a_1' and a_2' these solutions may be denoted by

$$E_i(x) \equiv E(a_i,x) \ \text{ and } \ E_i^*(x) \equiv E^*(a_i,x) \quad i = 1, 2 \tag{20}$$

With these functions the solutions for the mode amplitudes have been found to be

$$A_1(z) = B_1(x) = b \cdot E_1(-x)$$

$$= b \cdot [\cos \lambda \cdot E_1(x) + i \sin \lambda \, E_1^*(x)]$$

and
$$\tag{21}$$

$$A_2(z) = B_2(x) = b^* E_2(-x)$$

$$= b^* [\cos \lambda \, E_2(x) - i \sin \lambda \, E_2^*(x)] \ ,$$

where the coefficient $b \equiv [\nu^{1/2} \exp(i\psi)/2]^{1/2}$ and ψ is the phase of the coupling coefficient, $\psi \equiv \text{ph } c$. The term λ is used for convenience in writing some coefficients depending on ν and may be considered to be defined by the relations

$$\cos \lambda \equiv \exp(-\pi\nu) \ \text{ and } \ \sin \lambda \equiv [1 - \exp(-2\pi\nu)]^{1/2} \ . \tag{22}$$

Also recall that $\nu \equiv |c|^2/2\gamma k_o$ and $x \equiv \sqrt{2\gamma k_o} \ z$. The second form of these solutions (involving λ in (21) results from the fact that $E(a,-x)$ may be written as a linear combination of $E(a,x)$ and $E^*(a,x)$. These second forms are preferred for positive x because the available asymptotic expressions for $E(a,x)$ are valid only when x is positive. It is these asymptotic expressions which make it possible to obtain the simple expressions for coupler performance.

CHARACTERISTICS OF THE SOLUTION

Writing the power as the mean squared magnitude of the given solutions of the coupled-mode equations and using the asymptotic expressions for the $E(a,x)$ functions, we obtain the following results for large x (neglecting terms of higher order than $1/x^2$).

$$P_1(x) = |B_1(x)|^2 \sim 1 - \nu/x^2 \to 1 \qquad \nu \ll x^2, x < 0$$

and
$$\tag{23}$$

$$P_2(x) = |B_2(x)|^2 \sim \nu/x^2 \to 0 \ . \qquad 3\nu \ll x^2, x < 0$$
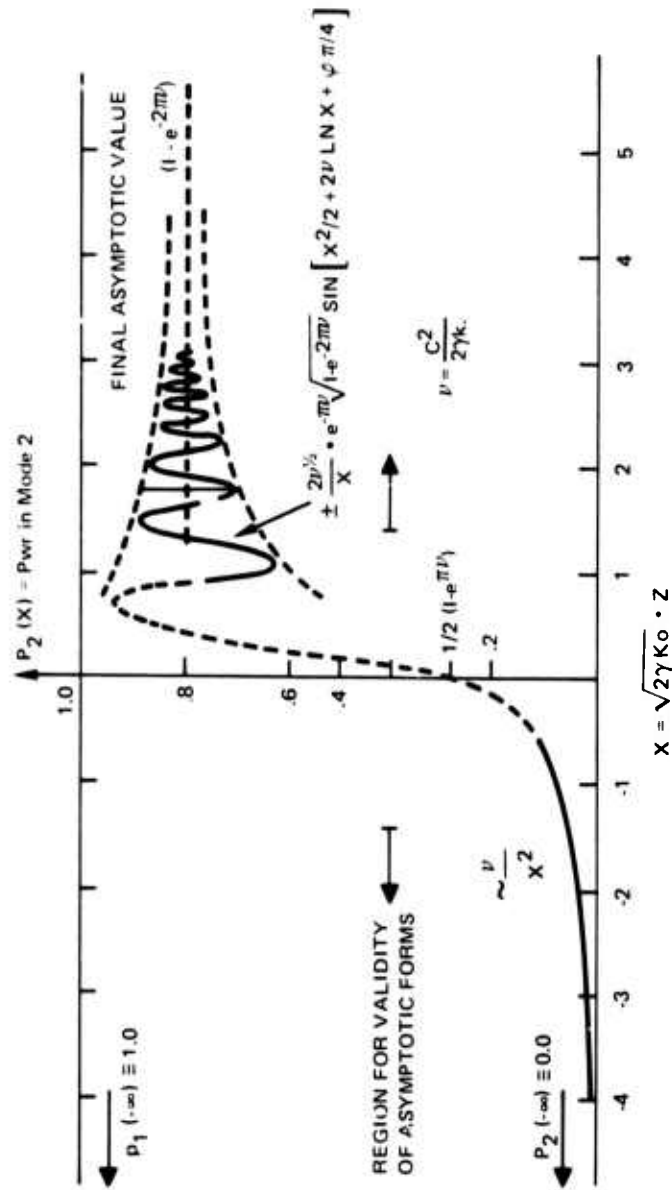
Figure 35. General features of solution for power transferred to second mode. Formulas are asymptotic expressions valid for $\sqrt{1+4\nu^2} \lll \chi^2$. Figure is only approximate and drawn for the case $\nu = 0.25$.

For the case of positive x we find:

$$P_1(x) \sim \cos^2\lambda + (2\nu^{1/2}/x)\sin\lambda\cos\lambda\sin[x^2/2 + 2\nu\ln x + \phi + \pi/4]$$

$$+ (\nu/x^2)(\sin^2\lambda - \cos^2\lambda)$$

and

$$P_2(x) \sim \sin^2\lambda - (2\nu^{1/2}/x)\sin\lambda\cos\lambda\sin[x^2/2 + 2\nu\ln x + \phi + \pi/4]$$

$$- (\nu/x^2)(\sin^2\lambda - \cos^2\lambda) \tag{24}$$

The condition for validity of these forms is that $\sqrt{1+4\nu^2} \ll x^2$, the coefficients in λ have been given above, and ϕ is a phase angle varying only slowly with ν.

In (24) the leading term is a constant which is the power remaining in each mode as $x \to \infty$. That is:

$$P_1(+\infty) = \exp(-2\pi\nu), \quad P_2(+\infty) = 1 - \exp(-2\pi\nu), \tag{25}$$

and $P_2(+\infty)$ is, of course, just the coupler efficiency provided the coupling region is long enough. The record term represents an oscillatory exchange of power between the modes which decreases in magnitude as $1/x$. The frequency of oscillation increases without limit as $x/2$ (representing the increasing phase mismatch); and the magnitude of the oscillation, at any fixed x, is proportional to $2\nu^{1/2}\exp(-\pi\nu)[1 - \exp(-2\pi\nu)]^{1/2}$, which decreases exponentially for large ν. These general features of the power, in mode 2 say, are shown in figure 35, which is drawn for $\nu \approx 0.25$. That this concept could lead to high efficiency for coupling to the second mode was well known from the microwave case, but the simple expression for predicting this efficiency from the parameters is new.

A program for the direct numerical integration of the coupled-mode equations has been written and used on several cases representing this coupler. The results are shown in figures 36–38, and fully confirm the properties found analytically. In particular, the power approaches the constant value predicted in each case.

The expression for the asymptotic efficiency of coupling from the first to the second mode is remarkably simple, and has a simple dependence on the parameters. It is

$$\text{Eff} = 1 - \exp(-2\pi\nu) \tag{26}$$

with

$$\nu \equiv |c|^2/2\gamma k_0 \equiv \frac{1}{2}|c/k_0|^2 \cdot (k_0/\gamma) \tag{27}$$

The efficiency depends on c and γ only through the value of ν. Couplers with differing values of c and γ can have the same efficiency if they have the same $|c|^2/\gamma$ ratio. The second form for ν above shows the convenience of expressing both c and γ in units of k_0. Representative values of ν are 0.1 for an efficiency of 50% and 0.50 for 96%. For even greater values of ν the efficiency becomes arbitrarily close to unity, and it becomes increasingly insensitive to uncertainties in the values of c and γ.

It is convenient to show these results graphically. This is done in figure 39, where the values of c and γ necessary to obtain given efficiencies are plotted. It should be recalled

Figure 37. Results of numerical integration for power coupled to mode 2, vs z. A case of "moderate" value of ν. L_c is a characteristic distance which is four times the length necessary for a phase-matched coupler with the same value of c.
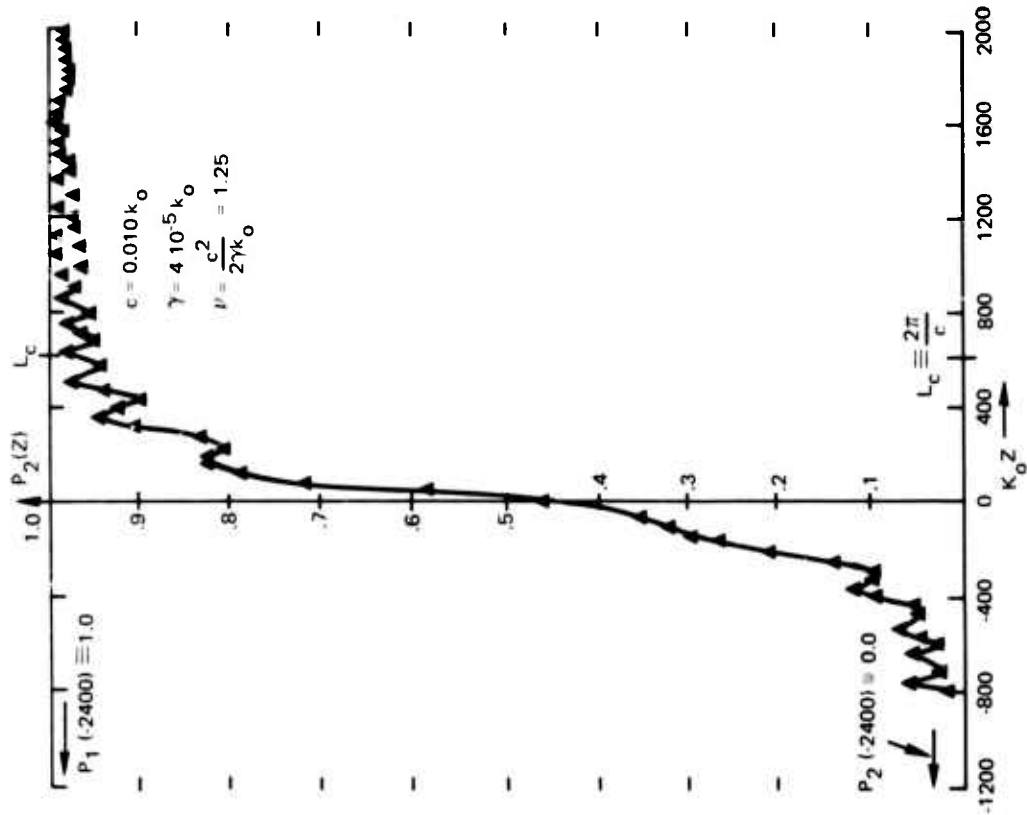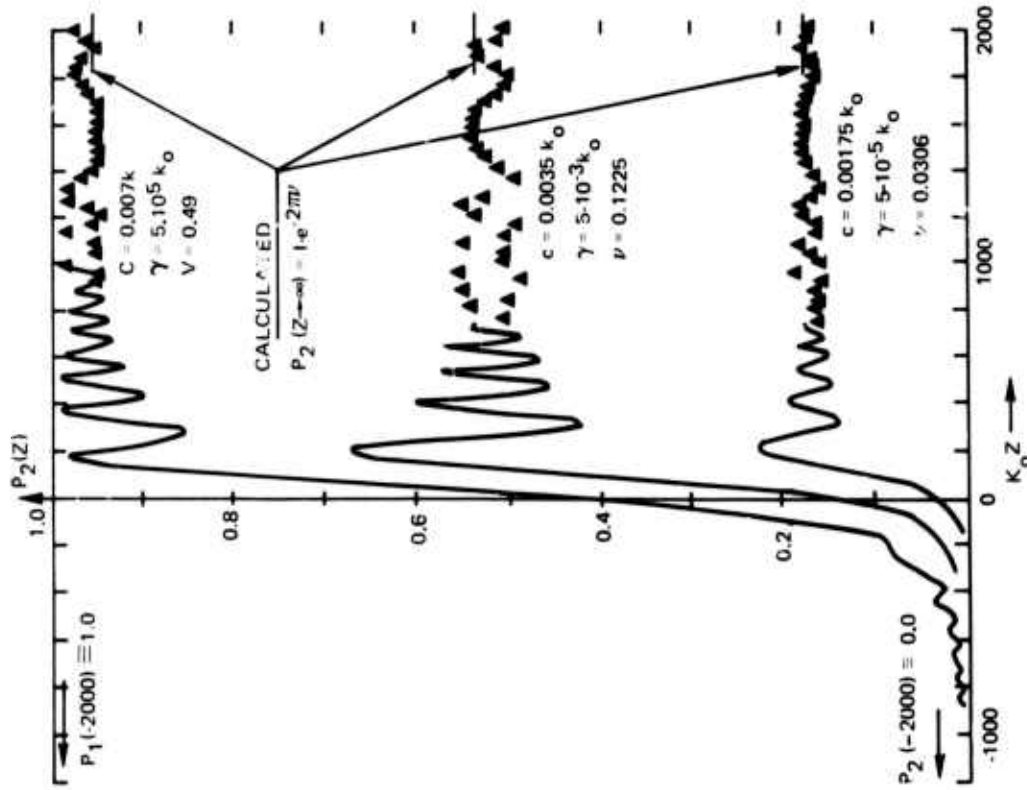

Figure 36. Results of numerical integration for power coupled to mode 2, vs z. Three cases of "small" values of ν. The smooth trend of points on the right is an aliasing effect due to inadequate sampling. (The frequency of the oscillation is about twice that at which values were output.)

that the coupled-mode theory assumes $|c| \ll k_0$, say $|c|/k_0 \gtrsim 10^{-2}$. Consequently, for high efficiency, the range of useful γ will be $10^{-4} \gtrsim \gamma/k_0$, efficiency increasing for decreasing values of γ.

Apart from the value of ν, which affects only the asymptotic efficiency, the value of γ sets the scale factor between the z distance and the x variable; it will determine the necessary length of a coupling region. Smaller values of γ (chosen for increasing the efficiency) will require larger coupling lengths. The coupler efficiency will be independent of the exact length only if it is sufficient for the oscillatory exchange of power to have decreased to some "small" magnitiude. For example, if $\nu = 0.5$ and the corresponding efficiency is 96%, then the power oscillation between modes becomes less than $\pm 4\%$ (that is, 1-0.96) for $x^2 \gtrsim 50$. In terms of the physical distance z, this condition is that $k_0 z \gtrsim 5(k_0/\gamma)^{\frac{1}{2}} = 5 \cdot k_0/|c|$. If the particular value of $\nu = 0.5$ is achieved by the choice $\gamma/k_0 = 10^{-4}$, $|c|/k_0 = 10^{-2}$, then we need $k_0 z > 500$. For smaller values of $|c|$ and γ, the coupler will be correspondingly longer. The value of $k_0 z > 5k_0/|c|$ may be compared to the length of a phase-matched coupler which must be exactly of length $k_0 L = k_0 \pi/2 |c|$ for 100% power transfer. Thus, the "tapered" coupler will be three or more times the length of the phase-matched coupler.

EXPERIMENTATION

Experimental work has centered on the development and testing of externally mounted fibers and on commissioning of the multitarget sputtering facility. Preliminary experiments on simple waveguide coupling structures have also been performed.

EXTERNALLY MOUNTED FIBERS

Externally mounted fibers consist of a rectangular (or other) cross section, high-refractive-index guiding fiber on top of a larger, low-index support fiber (figure 40). The combined fiber is drawn from a larger preform of approximately the same relative cross section. In order for the fiber drawing process to be successful, the two glasses used for the guiding and support fibers must have similar mechanical and thermal properties (such as softening temperature and thermal expansion coefficient). The glasses currently used are Corning 7059 ($n_D = 1.53$) for the guide and Corning 7740 ($n_D = 1.47$) for the support.

Suitably sized sheets are used to produce a preform which is then drawn down in a fiber pulling machine to produce the final fiber. Typical sizes of the final fiber are 10 by 1 μm for the guiding fiber and 100 by 20 μm for the support.

Although both guides maintain their rectangular cross section, some small changes in aspect ratio (width to thickness) have been observed. In addition, it has been found difficult to produce guides of high aspect ratio ($> \sim 30 : 1$).

Some optical evaluation has been carried out on these fibers. It has proved possible to use prism couplers to selectively excite the "thickness modes" of these fiber guides. Modes of fibers as narrow as 7 μm have been excited. Because these guiding fibers have widths much greater than their thickness ($> 5 : 1$), it is convenient to subdivide the modes by considering groups of "thickness modes" which describe the electric (TE) or magnetic (TM) field distribution across the thickness of the guide. For each thickness mode there exist a number of transverse modes which describe the field distribution across the width of the guide. To illustrate this, figure 41 shows a photograph of the output of a 7 by 2 μm waveguide coupled through a prism coupler. The guide was excited by end launching. The four thickness modes appear as bands of mode lines. Each mode line represents a particular transverse mode within that thickness mode.
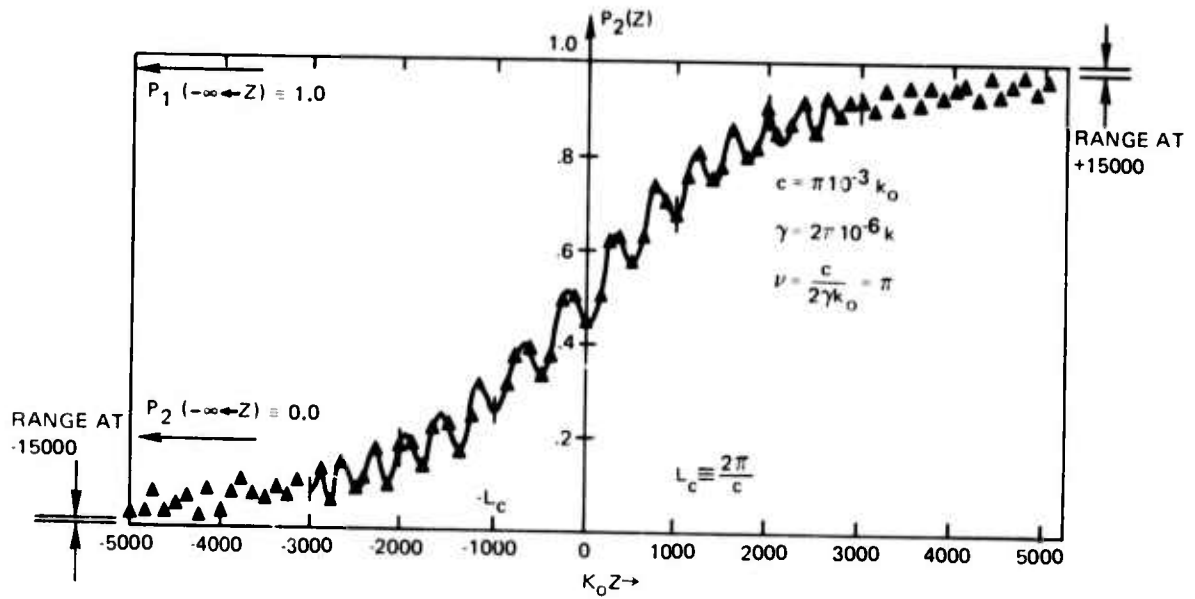
Figure 38. Results of numerical integration for power coupled to mode 2, vs z. A case of "large" value of ν. L_c is as described in figure 37. Note that near z = 0 there are two cycles of oscillation per L_c, as expected for a phase-matched region. For complete power transfer, essentially the whole range of $k_0 z$ shown is necessary; it is 40 times the length of a phase-matched coupler. This is a result of an unnecessarily small value for γ.
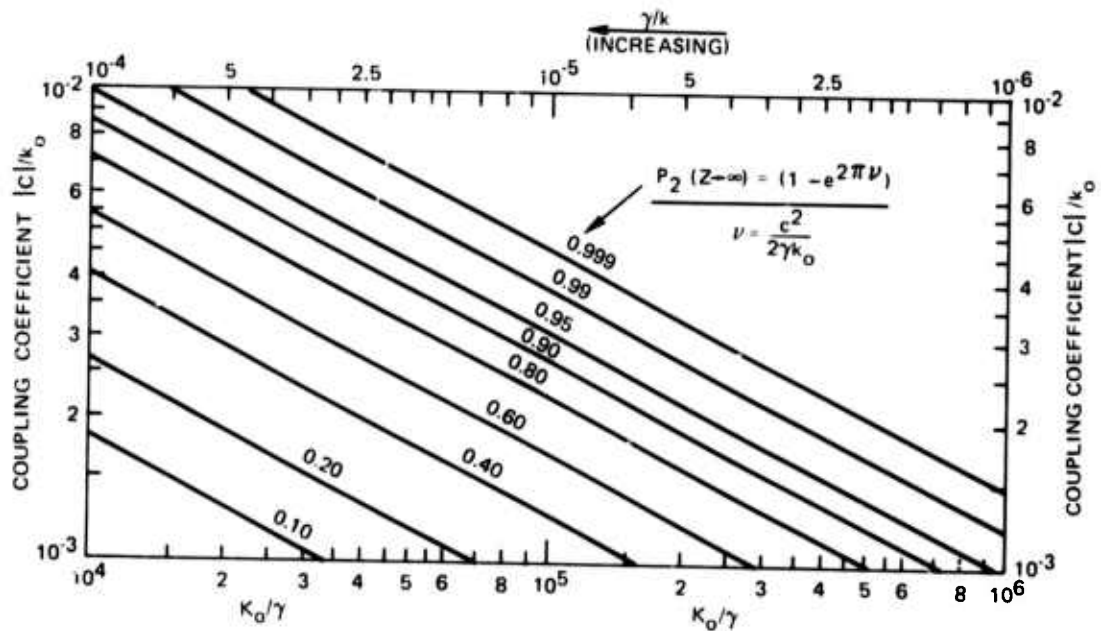

Figure 39. Coupling efficiency (power coupled to mode 2, P_2) vs coupling coefficient, c, and rate of change, γ, of propagation constants.

54
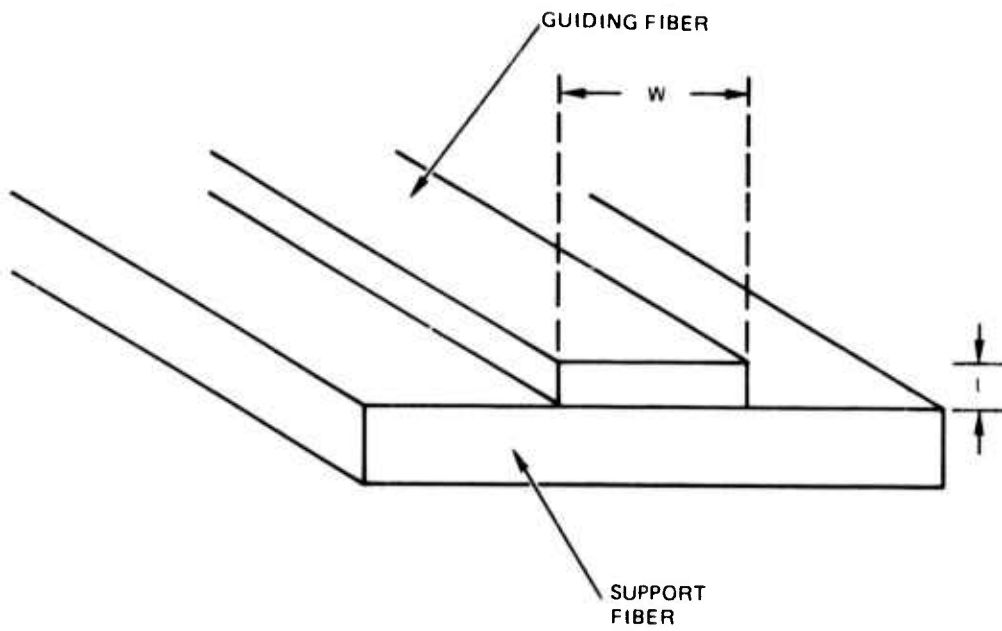
Figure 40. Externally mounted fiber consisting of a guiding fiber of width w and thickness t on a larger support fiber.

TE$_{3x}$ modes

TE$_{2x}$ modes

TE$_{1x}$ modes

TE$_{0x}$ modes

Figure 41. The spectrum of mode lines from a prism coupler on a 7-by-2-μm guide. The lowest line in each band corresponds to the fundamental transverse mode; higher lines correspond to higher-order modes.

Transmission loss measurements have been made for these waveguides by the destructive method of measuring light output after repeated shortening of the fiber. Substrate modes were stripped just prior to the fiber end. Losses of 0.05 dB/cm for multimode (25 by 5 μm) guide and 0.8 dB/cm for guide capable of carrying only one thickness mode have been measured. Fiber drawing has not as yet been conducted under clean-room conditions, which can be expected to result in reduced losses.

COUPLING EXPERIMENTS

An initial investigation of the use of externally mounted fibers as an interconnection medium has been carried out. Preliminary experiments on coupling from planar guide to fiber and from fiber to fiber have been performed.

PLANAR-GUIDE-TO-FIBER COUPLING.
Coupling from high-index guides on high-index substrates (such as diffused semiconductor guides or $LiNb_x Ta_{1-x} O_3$ on $LiTaO_3$) to externally mounted fibers will require careful design and complicated coupling structures, since phase match between the two guides cannot be directly achieved. However, in cases in which the planar guide is of high index on a low-index substrate (lower than the refractive index of the guiding fiber), coupling can be effected by simple tapering of the planer guide and by mounting the fiber directly over the taper as shown in figure 42. Light in the lowest-order mode of the planar guide is converted directly to light in the lowest-order mode of the fiber in this structure, which represents a type of branching waveguide concept. Preliminary experiments indicate that light is indeed coupled from the planar guide to the fiber, but accurate efficiency measurements have not been performed as yet because of dimensional mismatch between the Gaussian beam propagating in the planar guide and the width of the fiber. This concept should be directly transferable to coupling from linear guides to externally mounted fibers of the same width.

FIBER-TO-FIBER COUPLING.
To simulate coupling between an externally mounted fiber and a linear guide, experiments were conducted on coupling between two externally mounted fibers from the same draw. This is a special case, the two fibers being exactly phase matched, but none the less one that permits assessment of the difficulties of carrying out the clamping procedure. In preliminary experiments, two fibers were used (10 by 1 μm), with a matching oil between them to increase the coupling coefficient. Light was coupled into one fiber and coupled out after approximately 4 cm via prism couplers. A second fiber was manipulated into close proximity of and parallel to the first guide. By changing the gap between the two guides (figure 43), transferal of light was observed from the first fiber into the second with typical efficiencies of several tens of percent and ranging to above 60% (100% is theoretically possible). The experiment as described is not sufficiently definitive due to the close tolerance or alignment required (to within a fraction of a micrometer over the coupling length) and not as yet reliably achieved.
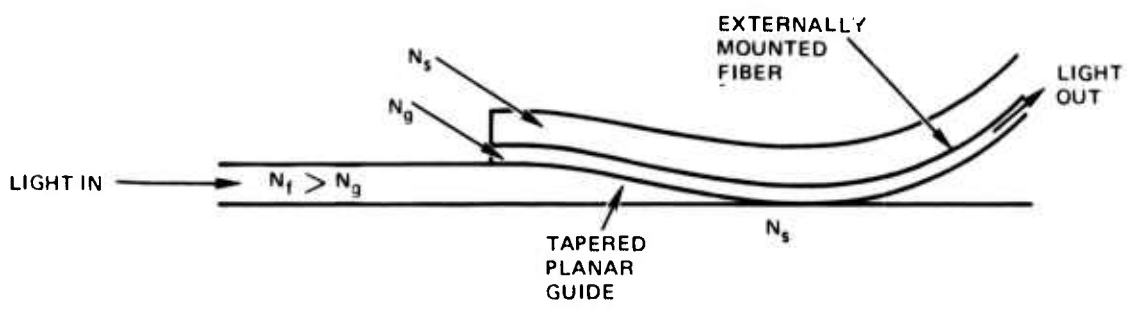
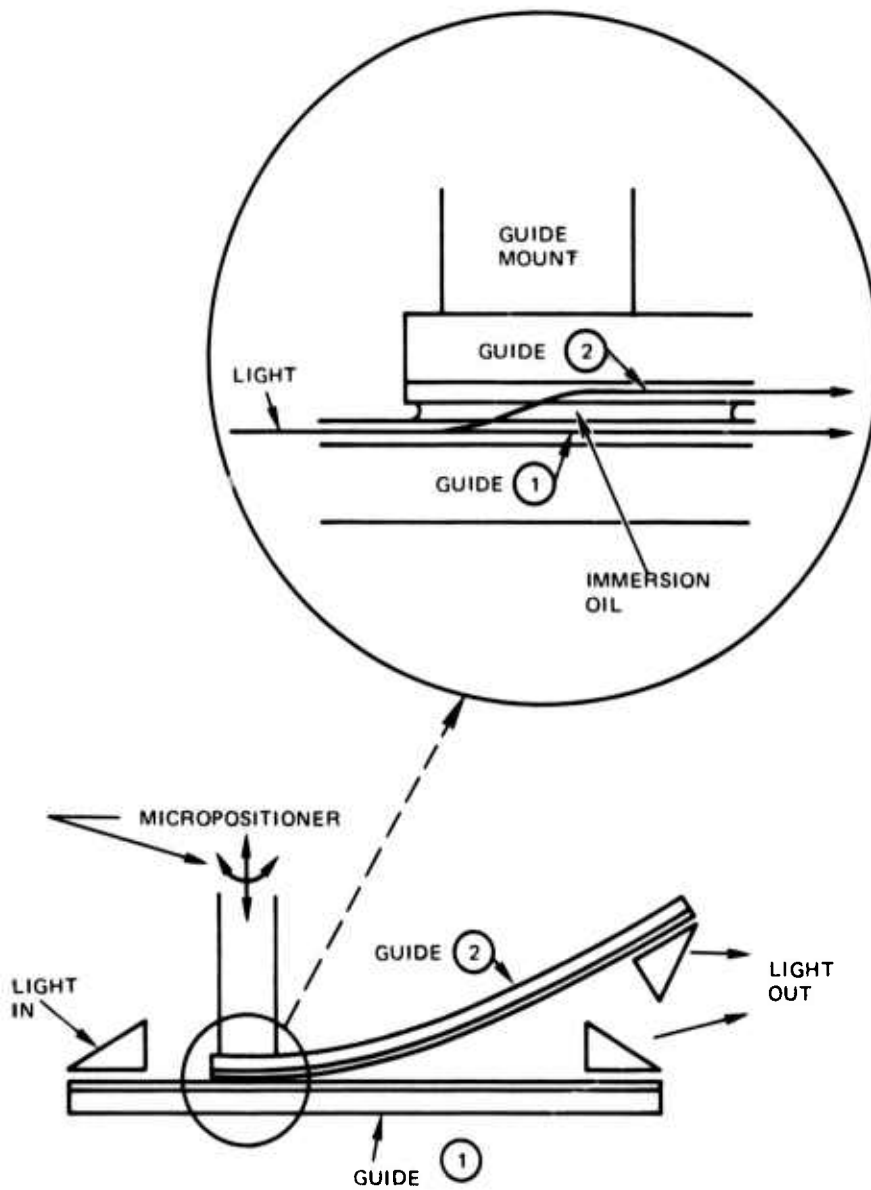Figure 42. Simple planar guide to fiber coupler.

Figure 43. Schematic of fiber-to-fiber coupler.

THEORETICAL ANALYSIS OF COUPLING FROM PLANAR TO LINEAR
WAVEGUIDES VIA HORN STRUCTURES

One barrier to efficient coupling from planar dielectric waveguides to linear waveguides is the difference between the size of the beam in a planar waveguide and the size of linear waveguides. The beam width in planar waveguides is on the order of 50 - 100 wavelengths, while the dimensions of linear waveguides are only a few wavelengths. This size difference produces a geometric mismatch whose deleterious coupling effects can be reduced by using a nonuniform waveguide or a lens system to focus the beam.

There are many ways in which optical coupling between fibers or lasers and integrated optical components may be achieved. In this section the use of a tapered structure similar in shape and function to a microwave horn is considered as a transition between a linear waveguide and a planar guide. This collinear coupling technique is useful under conditions in which a beam is launched in a film from either a fiber or a laser and is then coupled into a narrow channel that might serve as modulator or switch. The taper is also potentially useful for output coupling to fibers. When tapered waveguide section is used as a coupler, its efficiency depends upon the power that remains in the lowest-order mode at the open end or mouth of the taper. This section is a brief summary of detailed calculations to be found in reference 28.

Figure 44 shows the geometrical structure of the horn. The waveguide considered has indices: $n_1 = 1.57$, $n_2 = 1.0$, and $n_4 = 1.53$. The thickness in the y-direction is held constant at 0.5 micrometer and the thickness t_x of the linear waveguide is 5 micrometers. These parameters show the linear waveguide to be single mode.

The first shape of a coupling region to be investigated is a linear taper. If the coupling region is made long enough, we expect to be able to couple to the linear waveguide with any degree of efficiency desired; however, to keep the structure compact, the length should be kept to a minimum. For the linear taper shown in figure 44, the thickness is given by $t_x = 2z\tan(\phi)$, where ϕ is the half angle.

Solutions for the power contained in the lowest three modes in the reciprocal problem of coupling from a linear waveguide to a horn are plotted in figure 45 as a function of horn width. These values are calculated for an input power of 1 watt. The small oscillations about some average value, observed in figure 45, are caused by the coupling of energy between all the modes. This would disappear if the horn supported only two modes.

Beams that we are interested in coupling into linear waveguides contain most of their energy in the lowest-order mode, at least when beam size and horn mouth are approximately equal. This being so, coupling efficiencies can best be improved by improving coupling of the lowest-order mode at the mouth to the lowest-order mode in the waveguide. Comparing efficiencies for coupling to the lowest-order mode at different angles shows that care should be taken when choosing the horn angle; that is oscillations due to coupling to higher-order modes may occur such that a decrease in efficiencies would result for a particular thickness although the horn is longer.

Coupling efficiencies from the lowest-order mode at the mouth of the horn to a single-mode linear waveguide can be improved by varying the slope of the horn wall. Coupling coefficients were shown to be proportional to the slope of the wall, so the overall effect of coupling can be reduced if $\partial t_x/\partial z$ is small when $a_1/t + a_2/t_x^2 + a_3/t_x^3$ is large. The analogous problem of reflections in a transmission line has been investigated, and the results indicate this to be a good method of improving efficiency. By allowing the thickness to vary as $t_x = t_0 + A(1 - e^{-x^2/\ell^2})$, the coupling efficiency can be improved by 10% for the same-length horn. Figure 46 is a plot of power in the first three modes versus thickness of the horn for this thickness variation.
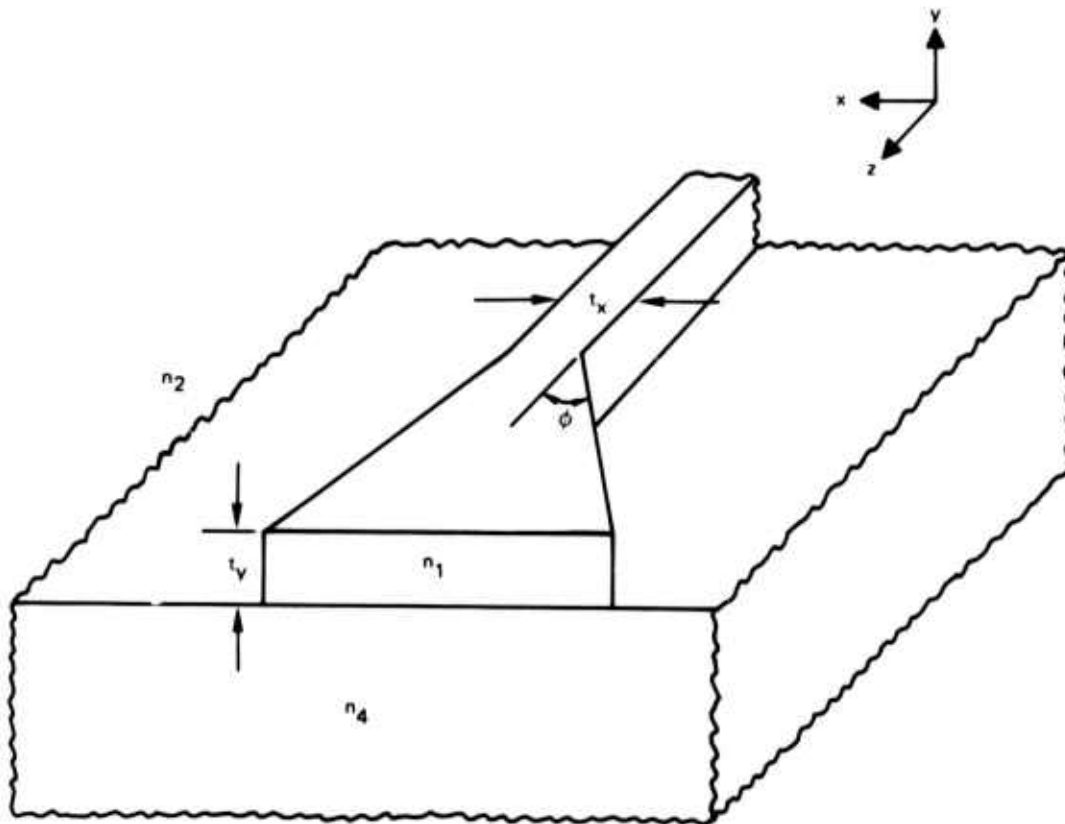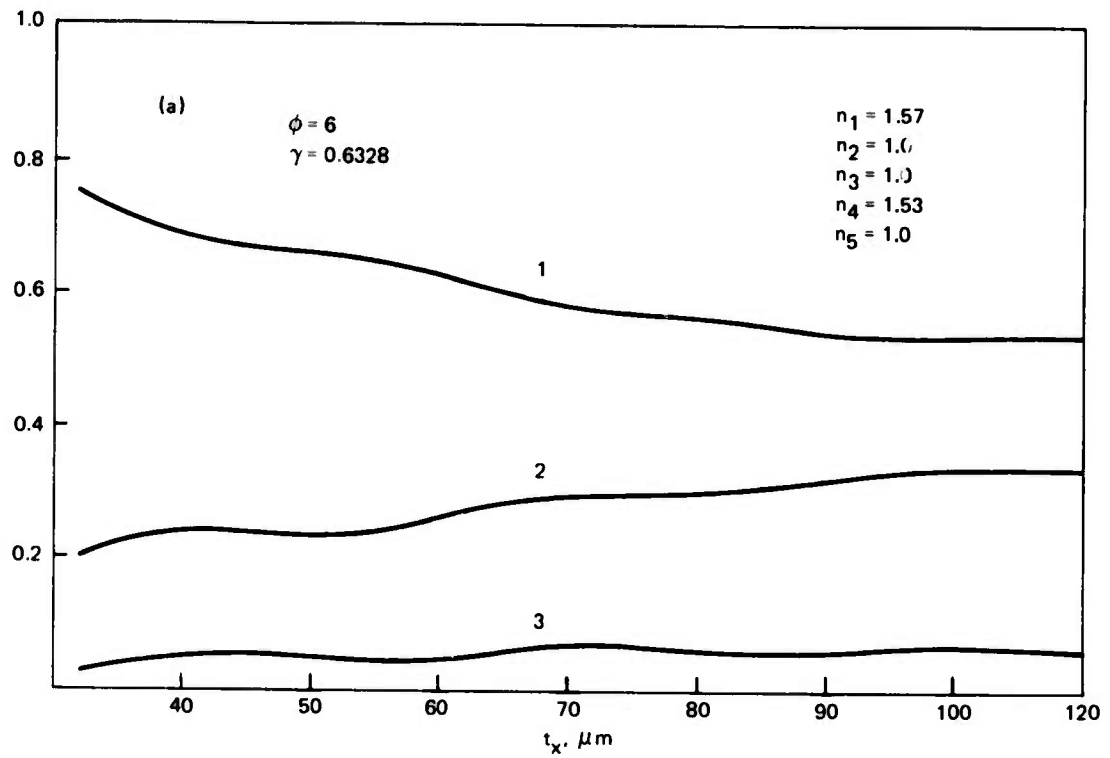
Figure 44. Horn geometry.

Figure 45. Power in first three modes as a
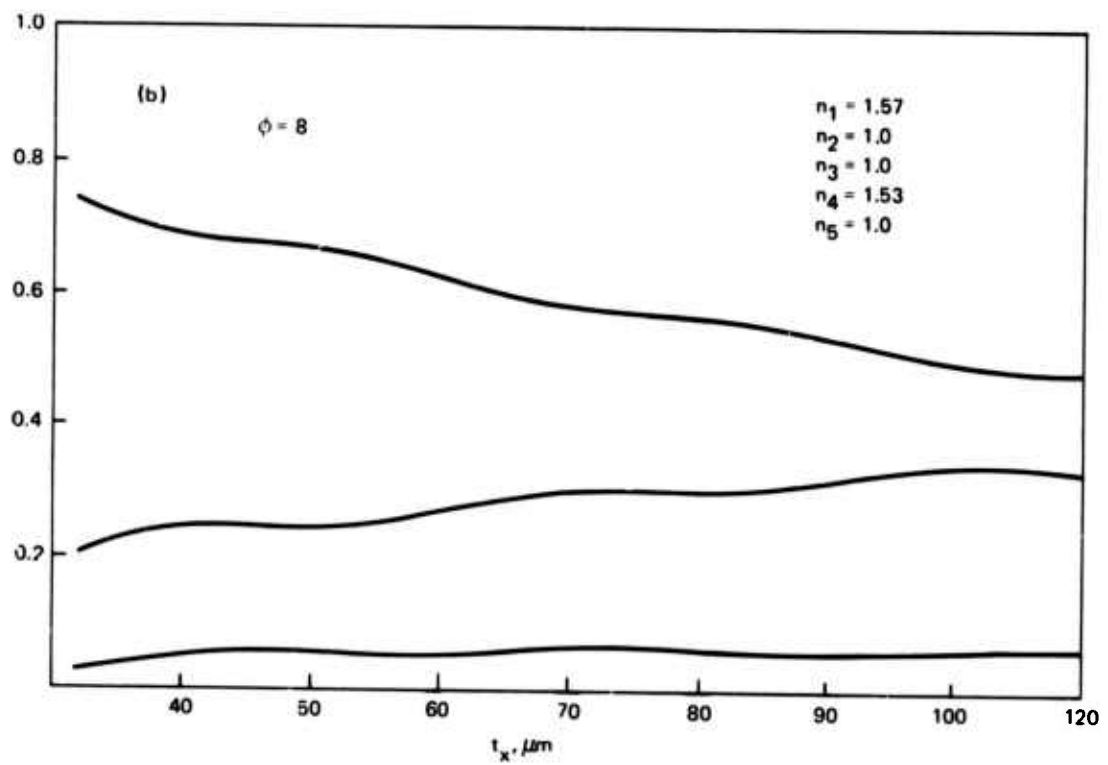function of horn width.

Figure 45. Continued.

60

Coupling efficiency for linear tapers has been shown to be approximately 50% for coupling from a beam whose width is approximately 100 μm. This efficiency is of course a function of flare angle and generally decreases with increasing angle. However, there is coupling to higher-order modes, so there is some oscillation around an average value that might tend to increase the efficiency for a small increase in angle at a given thickness.

The coupling efficiency can be improved by changing the slope of the waveguide wall. By this is meant that the efficiency increases for a given length of coupling region. For the configuration used in figure 46, an increase of approximately 10% is observed.
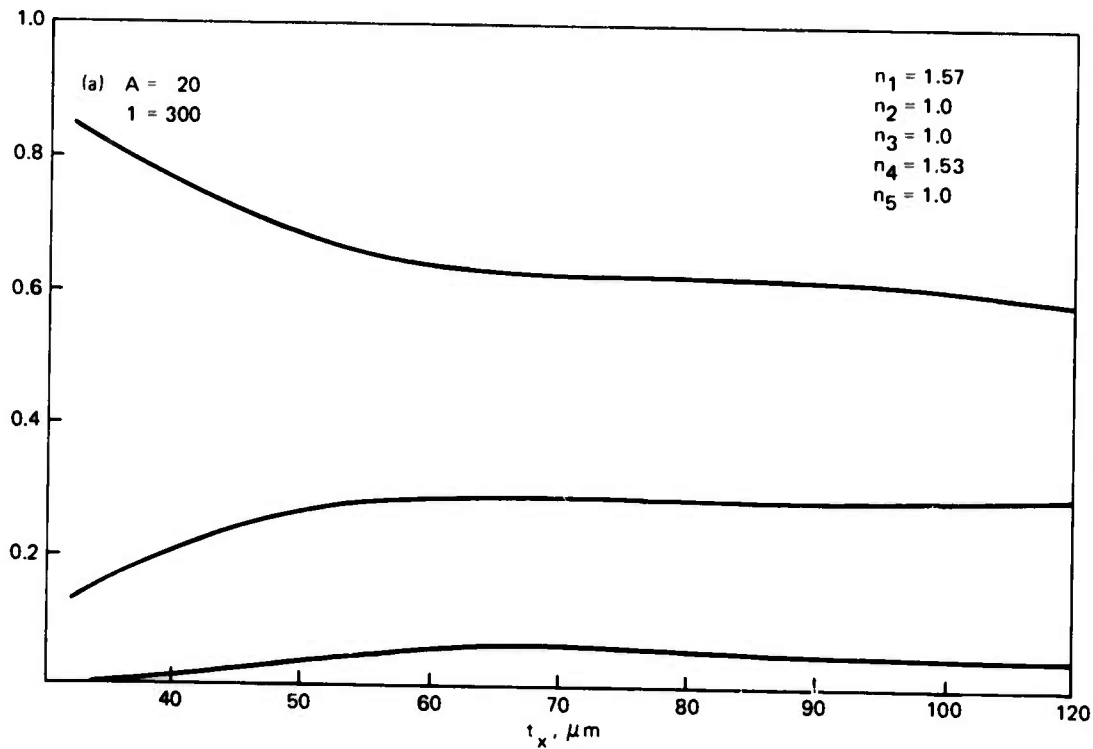

Figure 46. Power in first three modes as a function of horn thickness for specified thickness variation (see text).
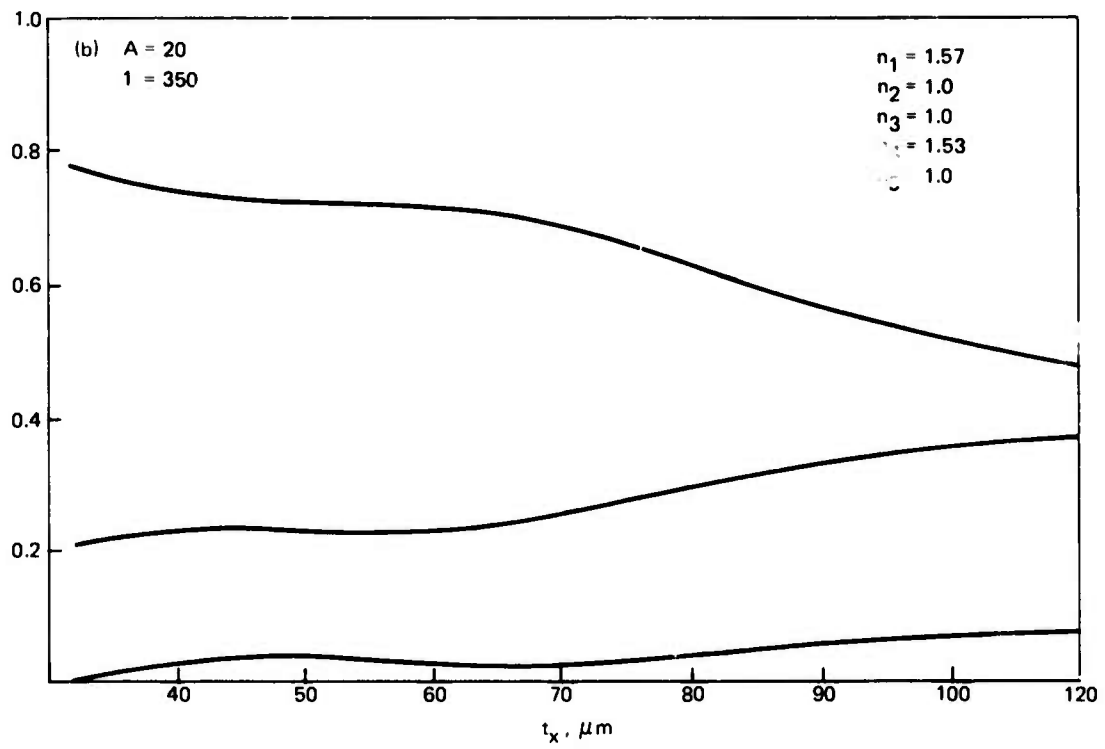
(b) A = 20
1 = 350

$n_1 = 1.57$
$n_2 = 1.0$
$n_3 = 1.0$
$n_4 = 1.53$
$n_5 = 1.0$

t_x, μm

Figure 46. Continued.

(c) A = 20
1 = 400

$n_1 = 1.57$
$n_2 = 1.0$
$n_3 = 1.0$
$n_4 = 1.53$
$n_5 = 1.0$

t_x, μm

Figure 46. Continued.

62
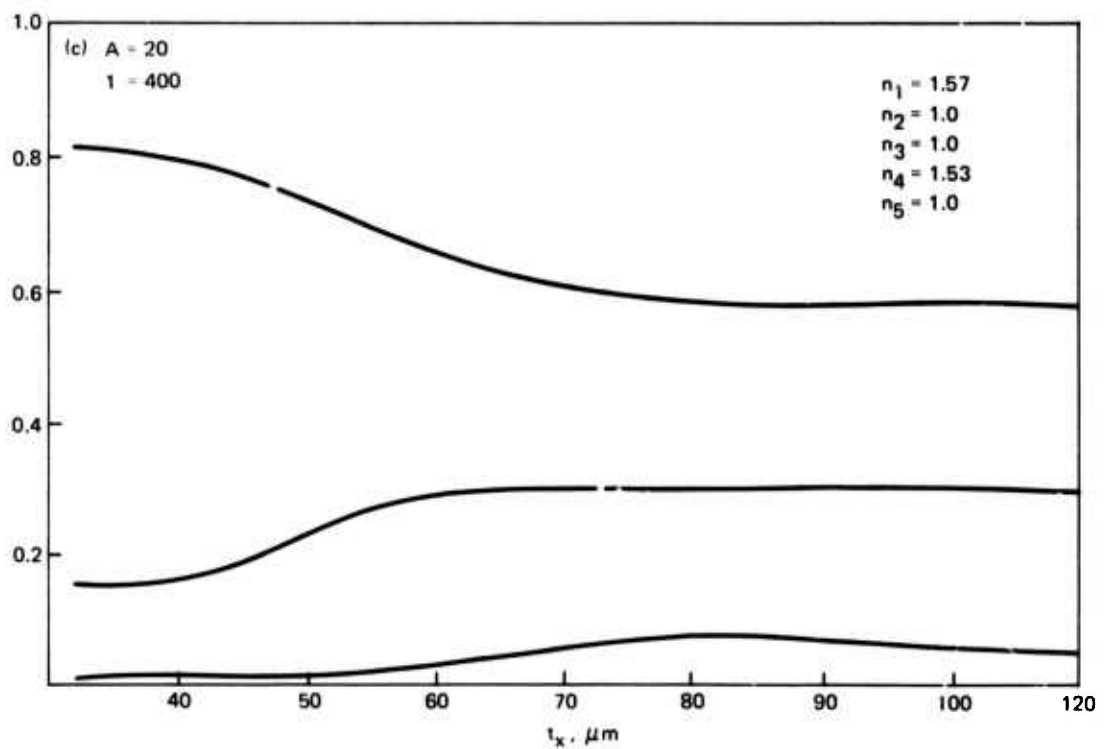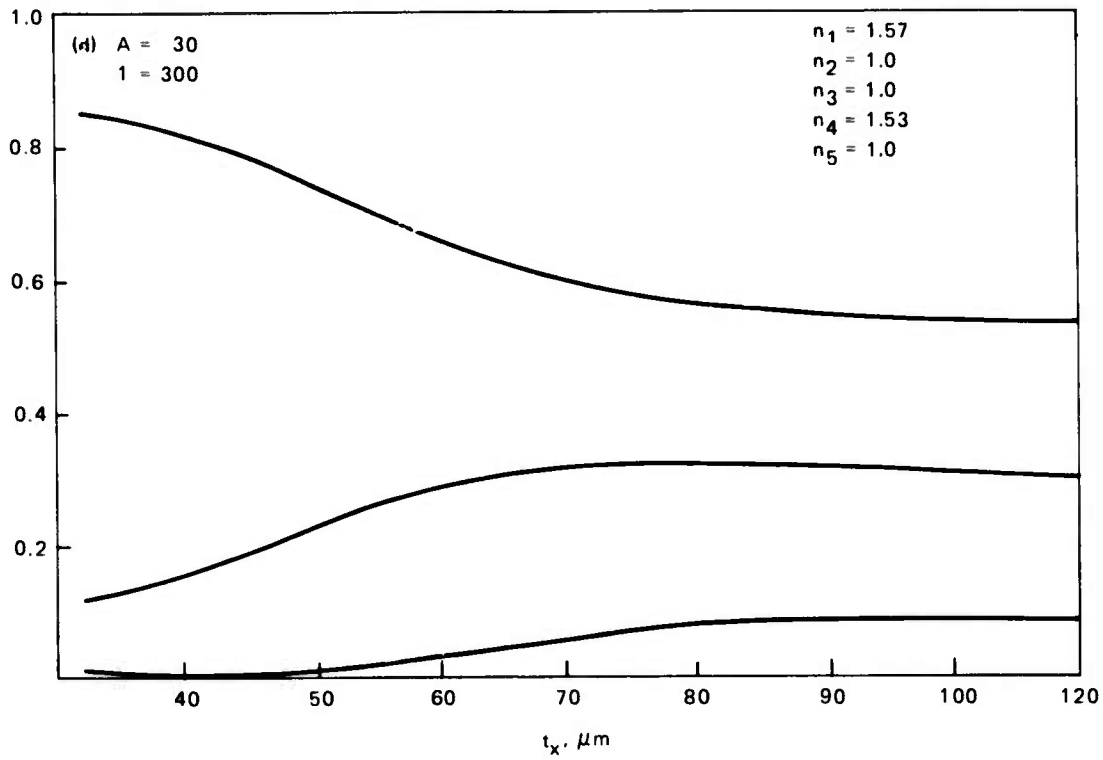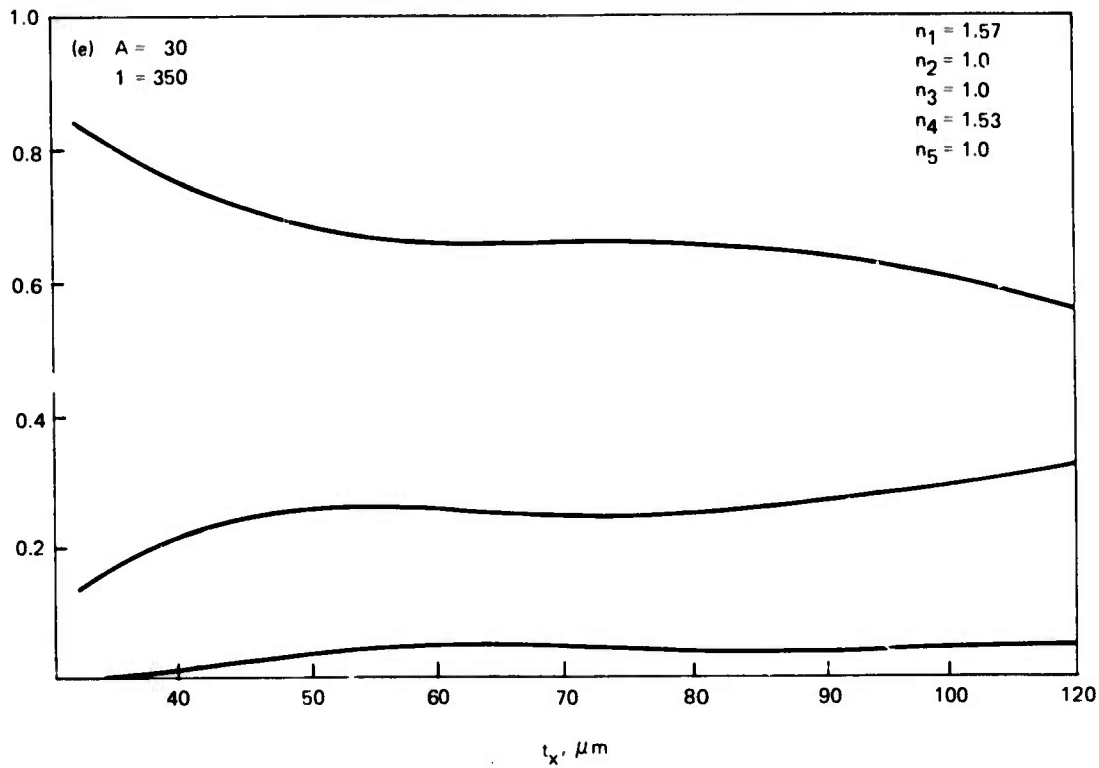
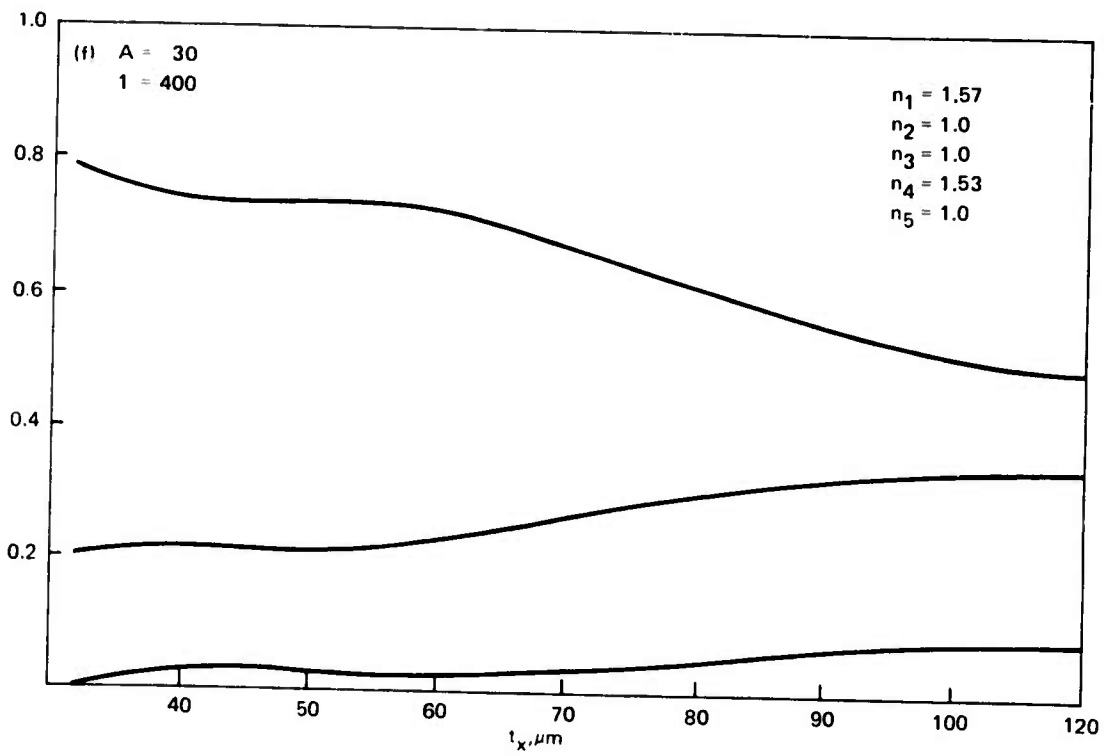Figure 46. Continued.

Figure 46. Continued.

Figure 46. Continued.

TRANSIENTS IN PERIODIC STRUCTURES:
COUPLED WAVES APPROACH
(UNIVERSITY OF CALIFORNIA, LOS ANGELES)

Most of the work in the field of electromagnetic wave propagation in periodic structures was directed toward continuous monochromatic waves [29-34]. However, it is of importance to study the transient response of these structures to finite pulses. In this section the reflection and transmission of a rectangular pulse and a Gaussian pulse impinging on a periodic structure of finite length ℓ are studied. In the analytic analysis, the general case of transversely bounded structures is considered wherein the coupled waves could be different modes and therefore have different longitudinal wave vectors [34]. For simplicity, and with no loss of generality, the numerical examples will correspond to the special case of transversely unbounded structures. The coupled-wave approach [35-37] is used and its limitations are briefly discussed relative to the more general Floquet approach [29-33]. There is no limitation on the type of periodicity as long as the coupling coefficient χ is small enough to satisfy the coupled-wave approach conditions.

TRANSFER FUNCTIONS

Let us consider a wave $F(z) U_p(x) e^{i\beta_p Z}$ propagating in a transversely bounded periodic structure. The index p represents the guided mode, β_p is its longitudinal wave vector, and $U_p(x)$ is the transverse dependence. This wave can be effectively coupled to a backward q mode wave $B(z) U_q(x) e^{-i\beta_p Z}$ if the phase-matching condition,

$$\beta_p + \beta_q = 2\pi/\Lambda \ . \tag{28}$$

is satisfied, where Λ is the period of the structure (figure 47). Let $\frac{\omega_{pq}}{2\pi}$ be the frequency at which phase matching occurs. The coupled-wave equations are well known to be [35-37].

$$\frac{dF}{dz} - i\delta_p F = i\chi_{pq} B$$

$$\text{and} \quad \frac{dB}{dz} + i\delta_q B = - i\chi_{pq} F \quad . \tag{29}$$

where χ_{pq} is the coupling coefficient which depends on the transverse functions $U_p(x)$ and $U_q(x)$ [34], δ_p and δ_q are the wave vector mismatch, and they are related to the frequency match by

$$\delta_p = \psi_p \Delta\omega = \frac{\partial\beta_p}{\partial\omega}\bigg|_{\omega_{pq}} \Delta\omega$$

$$\text{and} \quad \delta_q = \psi_q \Delta\omega = \frac{\partial\beta_q}{\partial\omega}\bigg|_{\omega_{pq}} \Delta\omega \tag{30}$$
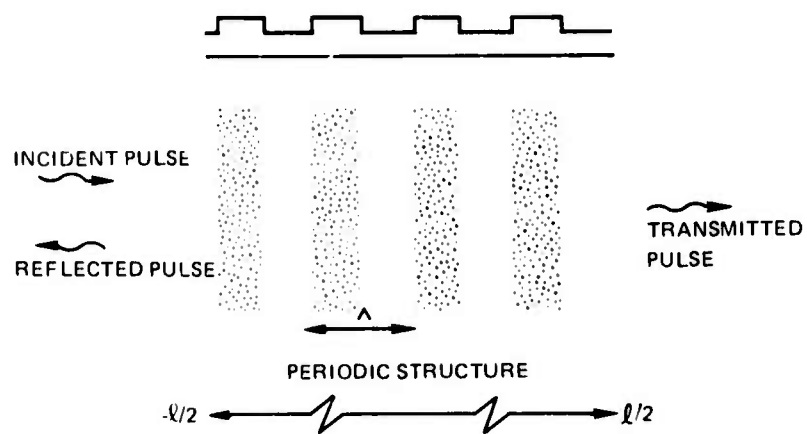
Figure 47. Configuration.

where $\Delta\omega = \omega - \omega_{pq}$,

ω = angular frequency ,

and ψ_p and ψ_q are the slopes of the dispersion diagram of the guided wave. If ℓ is the length of the coupling region, then the longitudinal boundary conditions are (see figure 47)

$$F(-\ell/2) = 1 , \qquad\qquad F(\ell/2) = T , \tag{31}$$

$$B(-\ell/2) = R , \quad \text{and} \quad B(\ell/2) = 0 , \tag{32}$$

where T and R are the transmission and reflection coefficients. The solution for the coupled-wave equation (29) with the above boundary condition gives

$$R = \frac{ix_{pq}}{D \coth D\ell - i \dfrac{\delta_p + \delta_q}{2}} \tag{33}$$

and

$$T = \frac{D e^{-i(\delta_q - \delta_p)\ell}}{D \cosh D\ell - i \dfrac{\delta_p + \delta_q}{2} \sinh D\ell} \tag{34}$$

where

$$D = \left[x_{pq}^2 - \left(\frac{\delta_p + \delta_q}{2} \right)^2 \right]^{\frac{1}{2}}$$

If the two coupled modes are identical, then $\delta_p = \delta_q = \delta$,

$$R = \frac{ix}{D \coth D\ell - i\delta} , \tag{35}$$

$$T = \frac{D}{D \cosh D\ell - i\delta \sin D\ell} . \tag{36}$$

and $\quad D = (x^2 - \delta^2)^{\frac{1}{2}}$.

From equations (33 and (34) we can derive the characteristic of the periodic structure:

1. Maximum reflection: $\quad R_M = i \tanh(x_{pq}\ell)$ $\qquad\qquad$ (37)

2. Minimum transmission: $\quad T_m = 1/\cosh(x_{pq}\ell)$ $\qquad\qquad$ (38)

3. $R = 0$ and $T = 1$ for: $\quad \delta_p + \delta_q = 2[\chi^2 + (n\pi/\ell)^2]^{1/2} \quad n = 1,2,...;$ (39)
   the corresponding phase of R is equal to $(2n - 1)\,\pi/2$

4. $|R|^2 + |T|^2 = 1$

In figure 48 are plotted the magnitudes of the reflection and transmission coefficients as a function of $\delta\ell$ for a given value of $\chi\ell$. Figure 49 shows the equimagnitude and equiphase curves of the reflection coefficient plotted as a function of $\chi\ell$ and $\delta\ell$. Figure 48 corresponds to a horizontal line ($\chi\ell = 2$) across figure 49.

TRANSIENT RESPONSE

The reflection and transmission of a pulse with a relatively narrow spectrum near ω_{pq} can now be derived from the reflection and transmission coefficients of each spectra component. For an incident pulse g(t) of spectrum $G(\omega)$,

$$G(\omega) = \int_{-\infty}^{+\infty} g(t)e^{\,i\omega t}\,dt \quad ,$$ (40)

the reflected pulse is

$$r(t) = \frac{1}{2\pi} \int_{-\infty}^{+\infty} G(\omega)\,R(\omega)e^{-i\omega t}\,d\omega$$ (41)

and the transmitted pulse is

$$p(t) = \frac{1}{2\pi} \int_{-\infty}^{+\infty} G(\omega)\,T(\omega)e^{-i\omega t}\,d\omega \quad .$$ (42)

Numerical inversion has been used by a number of authors [38, 39 and others] to obtain time response to radiation, propagation and scattering problems by convolution or transforms. The method used here is the Cooley-Tukey fast Fourier transform (FFT) [40], with $2^{11} = 2048$ samples in the FFT to calculate equations (41) and (42).

The reflection and transmission of several rectangular pulses were studied, with carrier frequency $\omega_0 = \omega_{pq}, \omega_1,$ and ω_2, where ω_1 and ω_2 correspond to the first two zeros of the reflection coefficient. The normalized pulse lengths τ were chosen as 0.25 time unit and 2.0 time units, where each time unit corresponds to the transit time of the pulse across the slab of length ℓ.

Figure 50 displays the reflected and transmitted pulses which result from an incident rectangular pulse of $\tau = 0.25$ with a carrier frequency exactly at phase match ($\omega = \omega_0$).
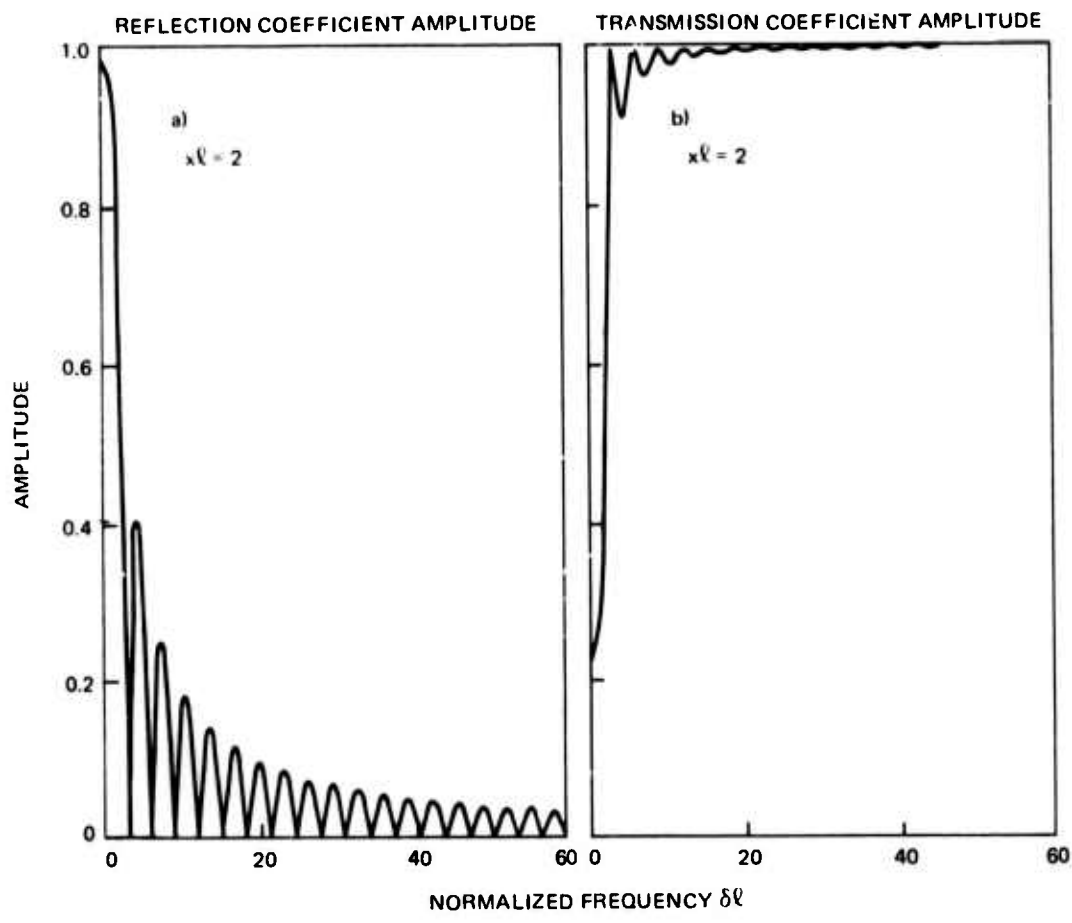
Figure 48. Magnitude of the reflection and transmission coefficients as a function of the normalized frequency mismatch: $\delta\ell = \Delta\omega\ell/c$ for a fixed coupling: $\chi\ell = 2$.
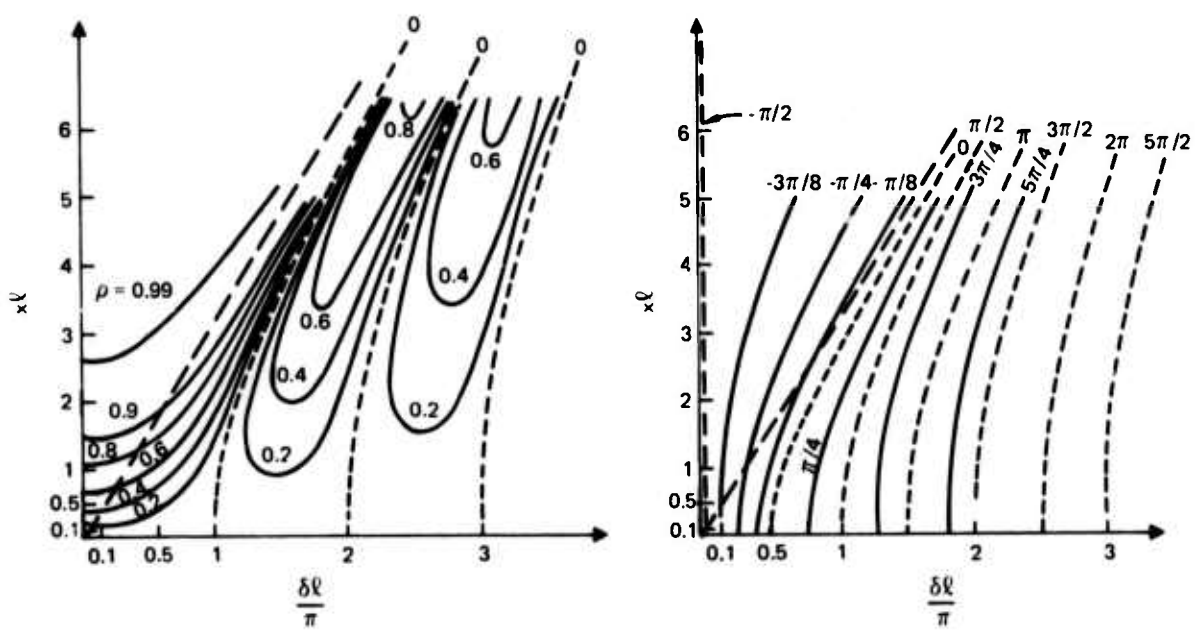

Figure 49. Equimagnitude and equiphase curves of the reflection coefficient as a function of $\delta\ell$ and $\chi\ell$. The reflection curve in figure 48 corresponds to a horizontal line ($\chi\ell = 2$) across the graph.
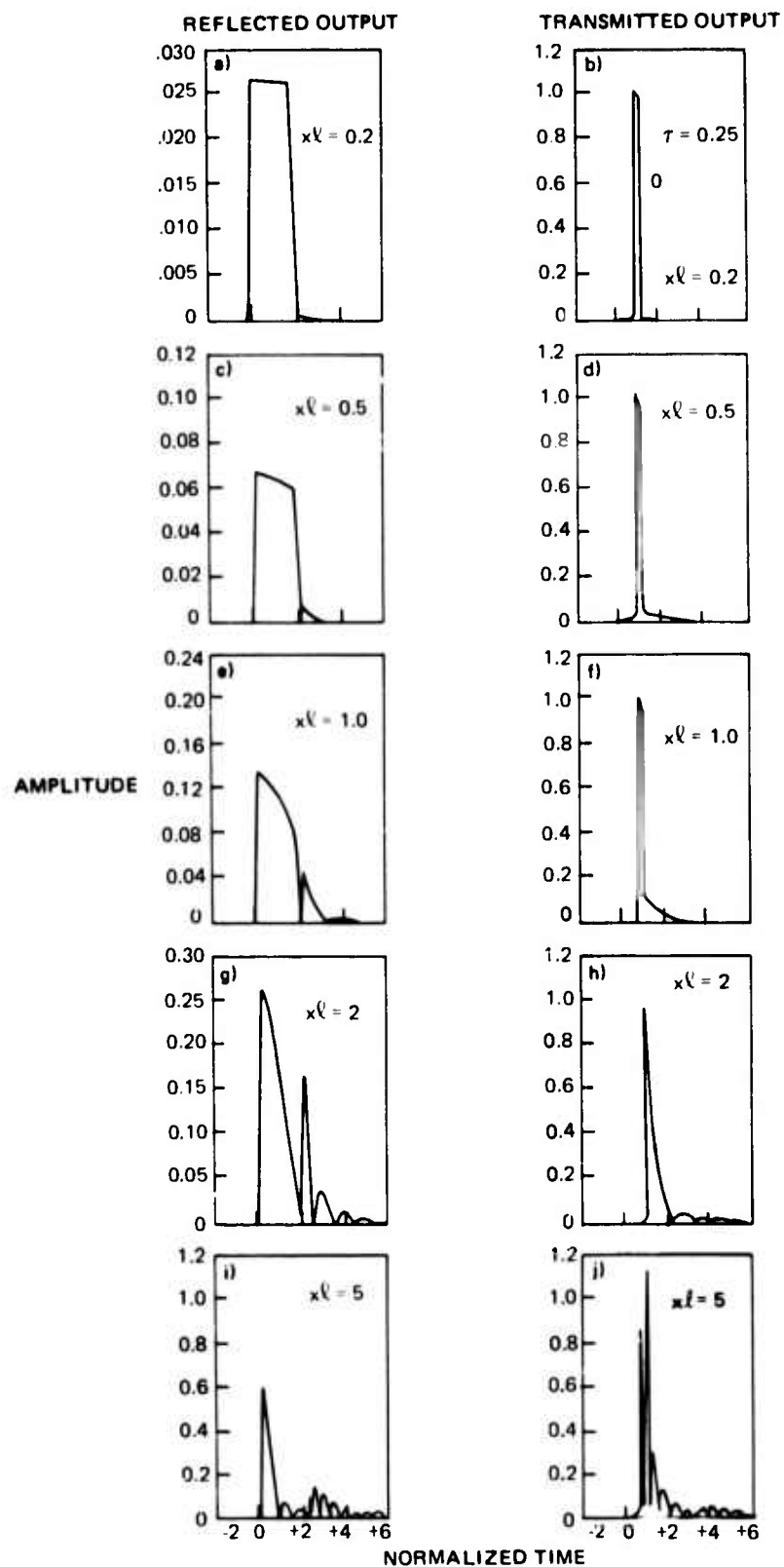
REFLECTED OUTPUT   TRANSMITTED OUTPUT

Figure 50. Reflected and transmitted pulses for different values of the coupling coefficient. The incident rectangular pulse has a length of 0.25 time unit and a carrier frequency ω_0 at the Bragg condition.
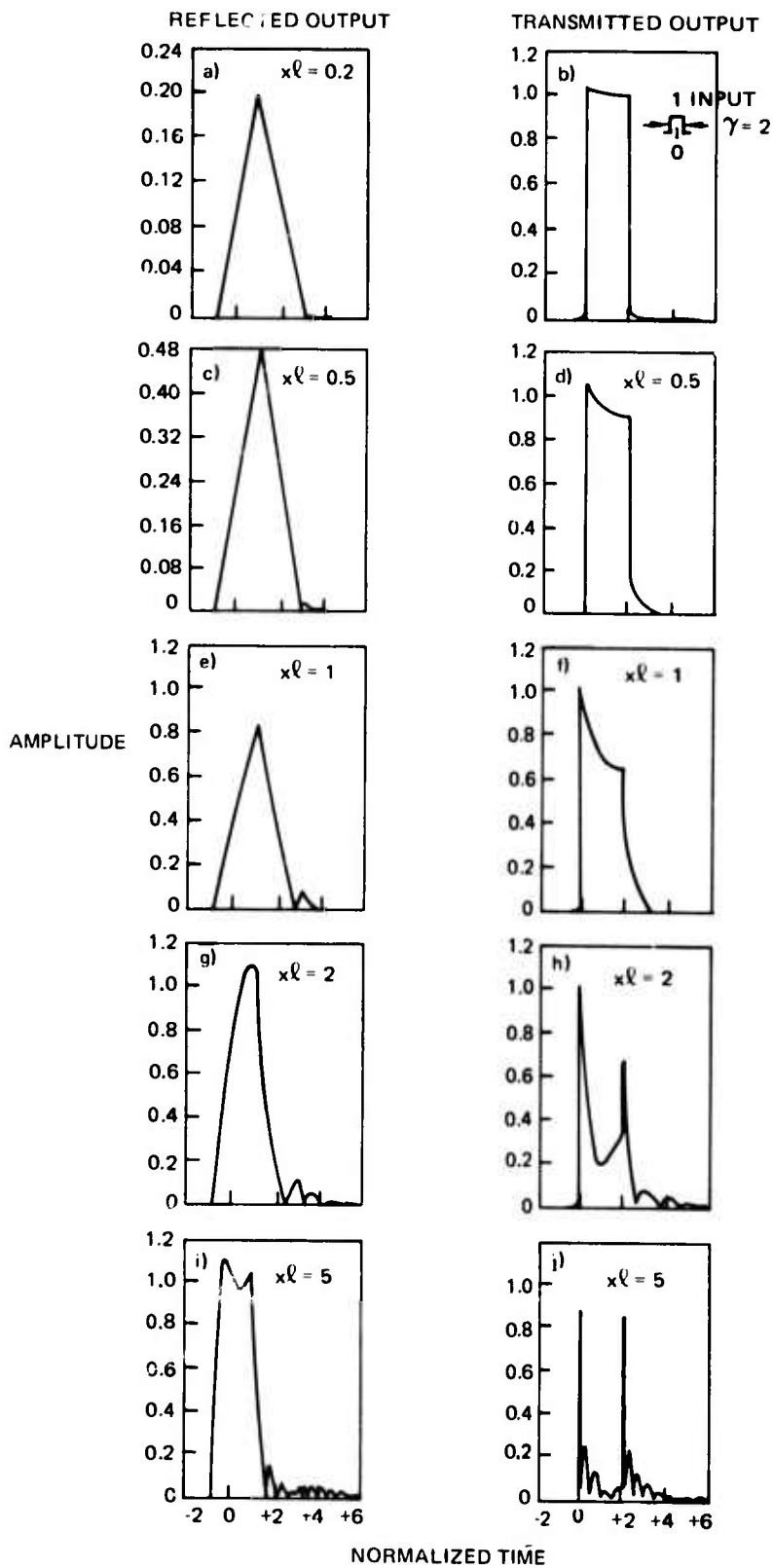
Figure 51. Reflected and transmitted pulses for different values of the coupling coefficient. The incident rectangular pulse has a length of 2.0 time units and a carrier frequency ω_0 at the Bragg condition.

The different cases correspond to different values of coupling χ. Note that for small coupling (figure 50a, b) the pulse is spread over two time units. This is to be expected, because the energy is reflected from successive stratifications and the echo from the last layer would take a round trip time of two units. Since the reflections are relatively weak ($\chi\ell \ll 1$), the transmitted pulse is similar to the delayed incident pulse. As the coupling is increased (stronger reflections from each layer), multiple interference plays an appreciable role which leads to transients over a longer time period (41). Simultaneously, the reflected and transmitted pulses will have a clear maximum at the leading edge. At high coupling (figure 50, j) the reflected pulse reaches its peak at 0.25 time unit and decreases rapidly afterward because most of the pulse energy has been reflected back by the first reflection. However, a relatively complicated interference tail of multiple pulses is present. The transmitted pulse in this case contains two main narrow peaks which correspond to differentiation of the incident pulse.

In figure 51 the same sequence is repeated for the case of a rectangular pulse of length $\tau = 2$. Some characteristics should be noted. At low coupling the reflected pulse (figure 51a) is similar to the autocorrelation of the incident pulse. This is due to the similarity of the input pulse and the reflection coefficient in the frequency domain and does not hold for other pulse widths or pulses in general. At high coupling, the transmitted pulse is again similar (except for wave interference echoes) to the derivative of the incoming pulse. As in the previous case, the transmitted pulse is similar to the input pulse for weak coupling ($\chi\ell \leqslant 1$).

Figure 52 displays the reflected and transmitted pulses for a Gaussian incident pulse of width $\tau = 2$ (where the width is taken at the $1/e$ values). Since the high-frequency components of the Gaussian pulse are smaller than those of the rectangular pulse, the characteristic sharpening of the edges of the transmitted pulse found in previous cases is not found here. In fact, for the cases examined in figure 52, all output pulses tend to mimic the input pulse. However, if the Gaussian pulse is narrowed to $\tau = 0.25$ (not shown here), the results are similar to a rectangular pulse of the same width.

Finally, a series of curves was generated for the case in which the carrier frequency is shifted to the first (figure 53) or second (figure 54) zero of the reflection coefficient. Both narrow ($\tau = 0.25$) and wide ($\tau = 2.0$) rectangular pulses were considered. In these cases the reflected output is greatly distorted by a number of auxiliary pulses including some that are larger than the leading pulse. As before, the transmitted pulse has the general shape of the incident one.

LIMITATIONS AND APPLICATIONS

The above results were based on the coupled-wave approach, which only accounts for the main forward and backward waves and neglects the presence of higher harmonics. This is valid as long as the coupling is weak enough so that the wave amplitude does not change much over a wavelength or over a structure period, and the input bandwidth is not too large. Otherwise, the Floquet approach [29-33], which accounts for all space harmonics, has to be used. This approach, even though it is simple to formulate, is relatively involved numerically and is left for future work.

Periodic structures, in different forms, have played an important role in many fields: microwave tubes, filters, antennas, and solid-state theory. Recently, their application in the emerging field of optical communication and integrated optics [33] has attracted appreciable attention. As it is likely that optical communication will be in digital form, the results of this paper are relevant. For instance, a periodic structure can be used as a "derivator" for edge
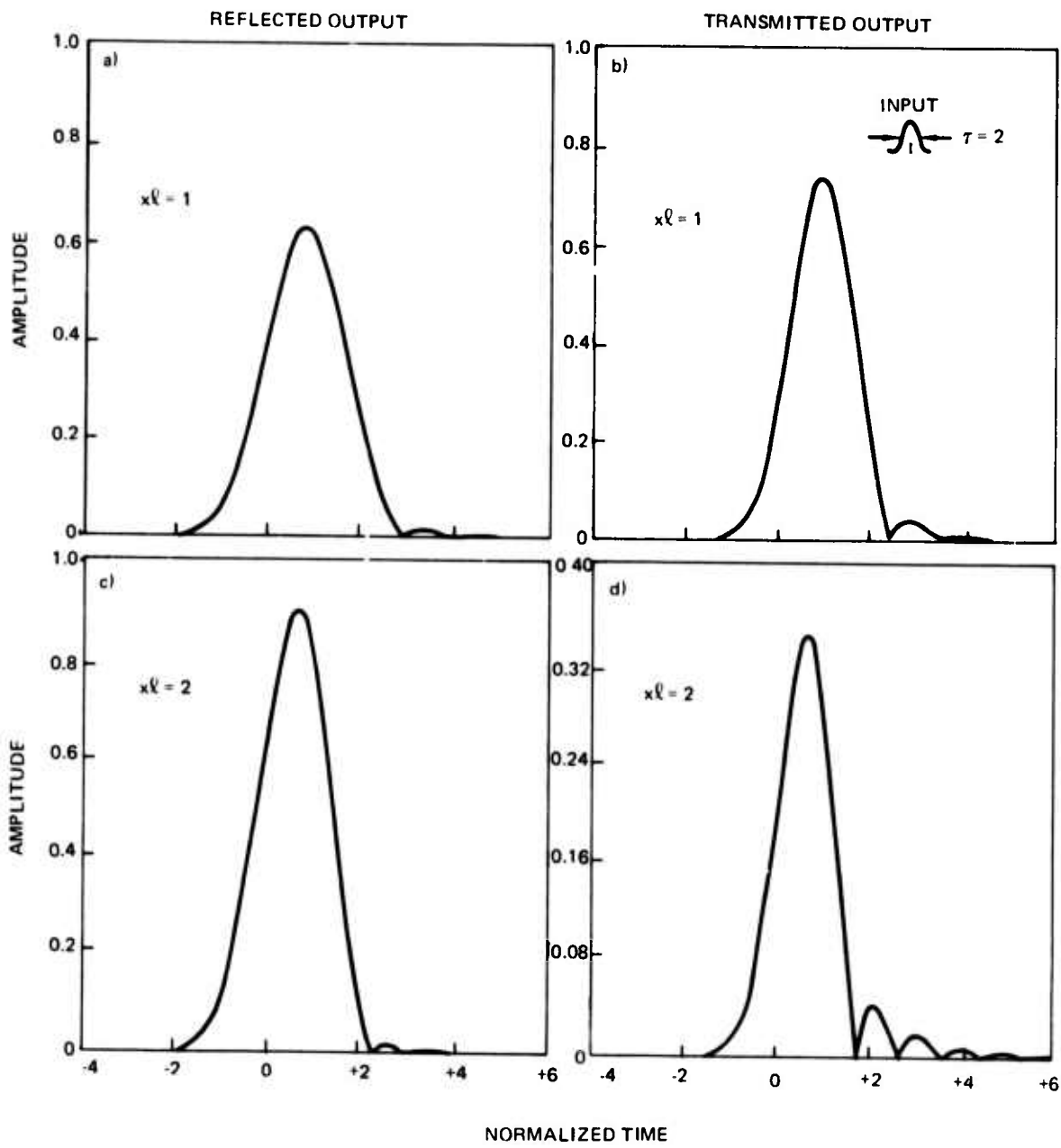
Figure 52. Reflected and transmitted pulses for the case of an incident Gaussian pulse of width 2.0 time units and carrier frequency ω_0.

Figure 53. Reflected and transmitted pulses for the case of an incident rectangular pulse of widths 0.25 time unit and 2.0 time units and carrier frequency ω_1 at the first zero of the reflection coefficient.
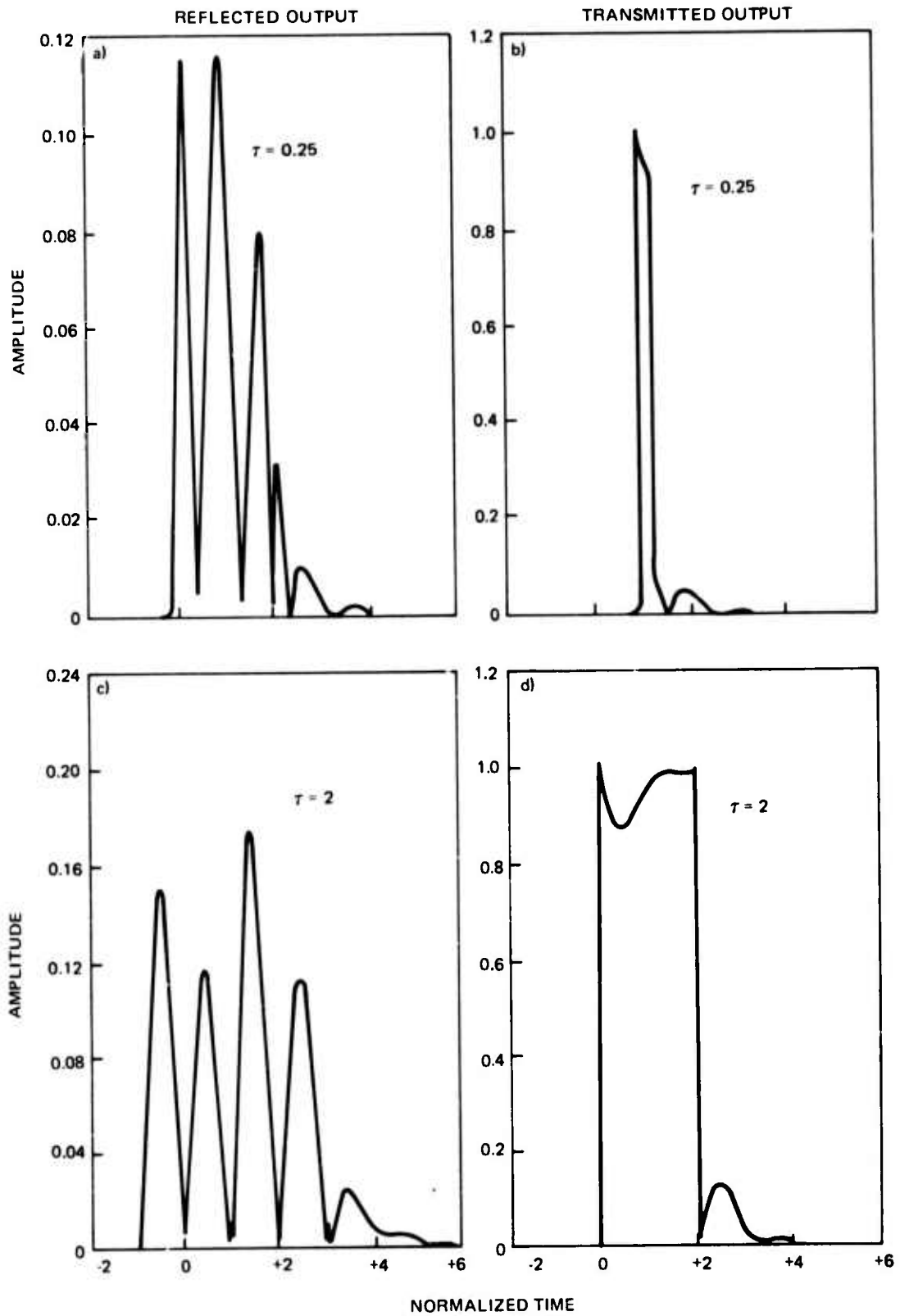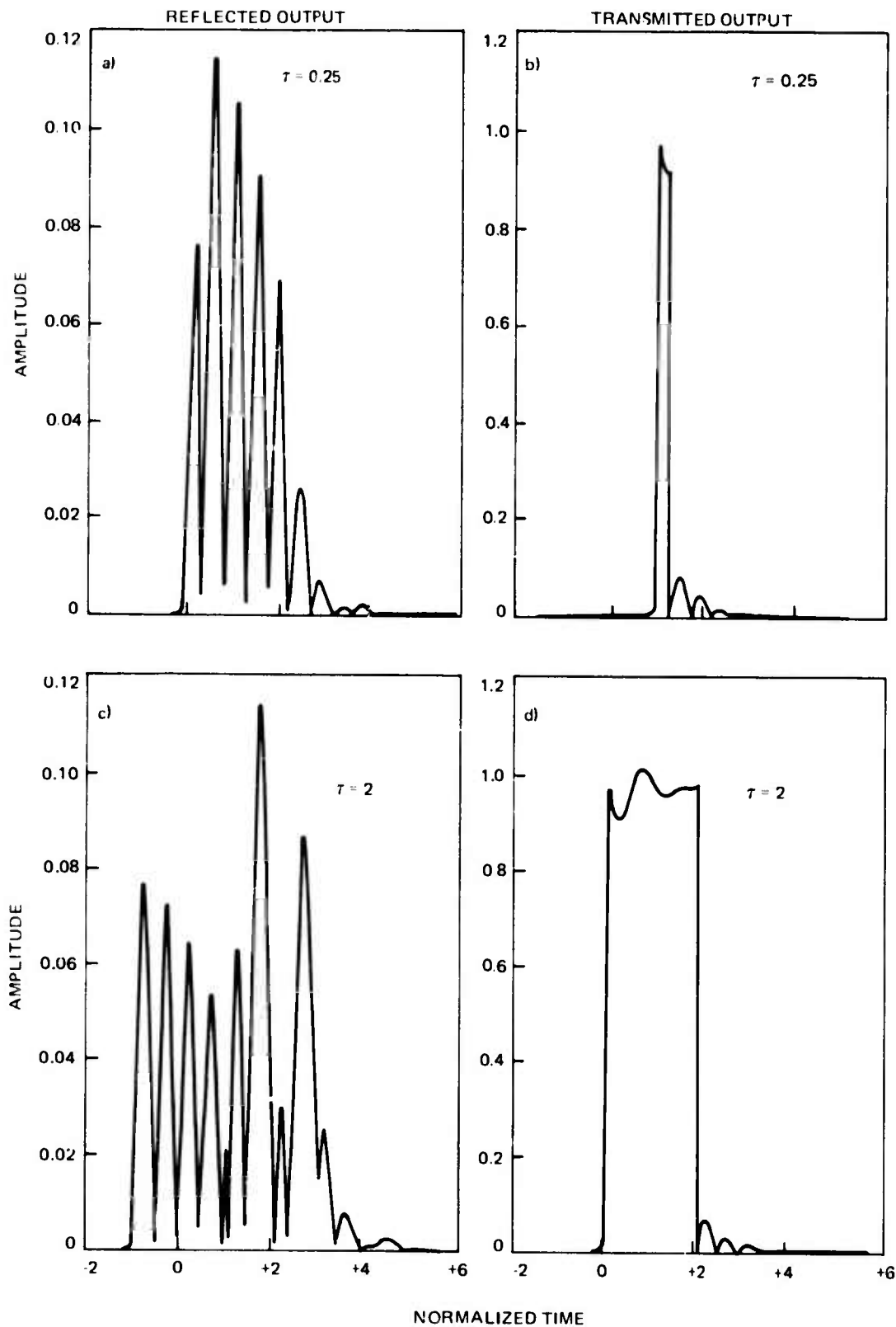
74

Figure 54. Reflected and transmitted pulses for the case of an incident rectangular pulse of widths 0.25 time unit and 2.0 time units and carrier frequency ω_2 at the second zero of the reflection coefficient.

detection (figure 51j) or multiple-pulse generator (figure 50j). The above results can also be applied to such fields as microwave filters, optical filters, and sounders of subsurface layers.

REFERENCES

[1] Miller, S. E., Marcatili, C. A. J., and Li, T., "Research Towards Optical-Fiber Transmission Systems," Proc IEEE 61, 12, p 1703, 1973

[2] Taylor, H.F., Martin, W.E., Hall, D.B., and Smiley, V.N., "Fabrication of Single-Crystal Semiconductor Optical Waveguides by Solid State Diffusion," Physical Review B, v 5, n 4, 15 February 1972

[3] Martin, W.E., and Hall, D.B., "Optical Waveguides by Diffusion into II-VI Compounts," Appl Phys Lett, v 21, n 7, 1 October 1972

[4] Martin, W.E., "Refractive Index Profile Measurements of Diffused Optical Waveguides," Applied Optics, v 13, n 9, p2112-2116, September 1974

[5] Burke, J.J., "Propagation Constants of Resonant Waves on Homogeneous, Isotropic Slab Waveguides," Applied Optics, v9, n 11, p 2444-2452, November 1970

[6] Marcuse, D., "TE Modes of Graded-Index Slab Waveguides," IEEE J of Quantum Electronics, v QE-9, n 10, October 1973

[7] Conwell, E.M., "Modes in Optical Waveguides Formed by Diffusion," Appl Phys Lett, v 23, n 6, p 328-329, 15 September 1973

[8] Boltaks, B.I., Diffusion in Semiconductors, Academic Press, 1963

[9] Nelson, D.F., and McKenna, J., "Electromagnetic Modes of Anisotropic Dielectric Waveguides at p-n Junctions," Journal of Applied Physics, v 38, n 10, p4057-4074, September 1967

[10] Schiff, L.I., Quantum Mechanics, McGraw-Hill, New York, p270-279, 1958

[11] Martin, W.E., "Waveguide electro-optic modulation in II-VI compounds," J Appl Phys, v 44, n 8, p 3703-3707, August 1973

[12] Kaminow, I.P., and Turner, E.H., "Electro-Optic Light Modulators," Proc of IEEE, v 54, n 10, p1374-1390, October 1966

[13] Namba, S., "Electro-optical effect of Zincblend," J Opt Soc Am, v 51, n 1, p 76-79, January 1961

[14] Caton, W.M. (to be published)

[15] Pavlopoulos, T.G., and Crabtree, K., "Fabrication of Channel Optical Waveguides in Glass by CW Laser Heating, J Appl Phys 45, p 4964, 1974

[16] Somekh, S., et.al., "Channel Optical Waveguides and Directional Couplers in GaAs", Appl Optics 13, 327, 1974

[17] Kogelnik, H., and Shank, C.V., "Stimulated Emission in a Periodic Structure," Appl Phys Lett, 18, p152, 1971

[18] Bjorkholm, J.E., and Shank, C.V., "Distributed Feedback Laser in Thin-film Optical Waveguides," IEEE J Quantum Electronics, 8, p833 1972

[19] Bjorkholm, J.E., Sosnowski, T.P., and Shank, C.V., "Distributed Feedback Laser in Optical Waveguides Deposited on Anisotropic Substrates," Appl Phys Lett 22, p132, 1973

[20] Yen, H.W., and others, Opt Comm (to be published)

[21] Nakamura, M., and others, "Optically Pumped GaAs Surface Laser with Corrugation Feedback," Appl Phys Lett, 22, p515, 1973

[22] Kogelnik, H., and Shank, C.V., "Coupled Wave Theory of Distributed Feedback Lasers," J Appl Phys 43, p2327, 1972

[23] Shank, C.V., Schmidt, R.V., and Miller, B.I., "Double Heterostructure GaAs Distributed-Feedback Laser," Appl Phys Lett, 25, p200, 1974

[24] Scifres, D. R., Burham, R.D., and Streifer, W., "Distributed-Feedback Single Heterojunction GaAs Diode Laser," Appl Phys Lett, 25, p203, 1974

[25]Nakamura, M., et.al., "Laser Oscillation in Epitaxial GaAs Waveguide with Corrugation Feedback," Appl Phys Lett 23, p224, 1973

[26]Nakamura, M., and Yariv, A., "Analysis of the Threshold of Double Heterostructure GaAs-GaAlAs Lasers with a Corrugated Interface," Opt Comm 11, p18, 1974

[27]Miller, J. C. P., Tables of Parabolic Cylinder Functions, Nat Phys Lab, HM Stat Off, London, 1955; "Parabolic Cylinder Functions," chap 19 of Handbook of Mathematical Functions, M. Abramovitz and I. Stegun, editors, NBS Appl Math Ser 55, Washington, DC, p686-720, 1964

[28]Winn, R. K. "A Theoretical Analysis of Coupling from Planar to Linear Waveguides," Thesis, University of Washington (1974), NELC Contract N00953-73-M-1437, Final Report

[29]Brillouin, N., Wave Propagation in Periodic Structures, Dover, N.Y., 1953

[30]Tamir, T., Wang, H. C., and Oliner, A. A., "Wave Propagation in Sinusoidally Stratified Dielectric Media," IEEE Trans, MTT-12, 323-335, 1964

[31]Casey, K. F., Mathis, J. R., and Yeh, C., "Wave Propagation in Sinusoidally Stratified Plasma," J Math Phys, 10, p891-987, 1969

[32]Tamir, T., and Wange, H. C., "Scattering of electromagnetic waves by a sinusoidally stratified half-space," Canadian J Phys, 44, p2073-2093, 1966

[33]Elachi, C., and Yeh, C., "Periodic Structures in Integrated Optics," J Appl Phys, 44, p3146-3152, 1973

[34]Elachi, C., and Yeh, C., "Mode conversion in periodically disturbed thin film waveguides," J Appl Phys, 45, 1974

[35]Louisell, W. H., "Coupled mode and parametric electronics," J. Wiley and Sons, N.Y. 1960

[36]Marcuse, D., "Light Transmission Optics," Van Nostrand, N.Y., 1973

[37]Kogelnik, H., and Shank, C. V., "Coupled Wave Theory of Distributed Feedback Lasers," J Appl Phys, 43, p2327-2335, 1972

[38]Ray, P. S., and Stephens, J. J., "Far-field Transient Backscattering by Ice Spheres," Radio Science, 9, p 43-55, 1974

[39]Hill, D. A., and Wait, J. R., "The Transient Electromagnetic Response of a Spherical Shell of Arbitrary Thickness," Radio Science, 7, p911-935, 1972

[40]Cooley, J. W., Lewis, P. A., and Welch, P. D., "The Fast Fourier Transform Algorithm," IBM Watson Research Center, Yorktown Heights, N.Y., 1969

[41]Elachi, C., Jaggard, D., and Yeh, C., "Transients in Periodic Structures: Coupled Waves Approach" (to be published)